UNIVERSITY OF CALIFORNIA, SAN DIEGO

Label-free lab-on-a-chip flow cytometer for biomedical applications

A dissertation submitted in partial satisfaction of

the requirements for the degree Doctor of Philosophy

in

Materials Science and Engineering

by

Tsung-Feng Wu

Committee in charge:

Professor Yu-Hwa Lo, Chair
Professor Shaochen Chen
Professor Drew Hall
Professor Michael Heller
Professor Xiaohua Huang

2013

The dissertation of Tsung-Feng Wu is approved, and it is acceptable in quality and form for publication on microfilm and electronically:

_____

_____

_____

_____

_____

Chair

University of California, San Diego

2013

Dedication

This dissertation is dedicated to my family.

Table of Contents

List of Figures

List of Tables

Acknowledgements

First, I would like to express my deepest gratitude to my advisor, Prof. Yu-Hwa Lo, for his tremendous guidance, care, and patience. Prof. Lo's direction inspired me greatly throughout the research and thesis writing process. Without his continuing support, I could not have finished my Ph.D research. Prof. Lo was the best advisor and mentor any Ph.D candidate could ask for, and it was a privilege and honor to study and perform research in such an excellent facility and work environment where Prof. Lo's knowledge and personality have lasting impact on my life.

I am also grateful for the other members on the dissertation committee, namely Prof. Shaochen Chen, Prof. Michael Heller, Prof. Xiaohuang Huang, Prof Eric Lauga and Prof. Drew Hall. Their suggestions contributed not only to the direction of this work, but also helped me develop critical thinking skills as a scientist and an engineer.

Since my research projects were all interdisciplinary, it was impossible to accomplish them without significant assistance from other departments. I appreciate all the collaborators for their effort and valuable input. I am particularly thankful for Dr. Sung Hwan Cho, Dr. Chun-Hao (Randy) Chen, Dr. Jessica Godin, Dr. Frank Tsai, Dr. James Cheng, Dr. Arthur Zhang, Dr. Jose Morachis, Dr. Ian Lian, Dr. Ian Quigley, Ti-Hsuan Ku, Hosuk Lee, Luca Pion-Tonachini and NANO3 staffs. I would like to thank all of Lo group members, Dr. Wen Qiao, Ashkan Arianpour, Samia Rahman, Yu-Hsin Liu, Roger Chiu, Tiantian Zhang, Ramkumar Subramanian, Nasim Vahidi, Tony Yen, David Hall, Yuchun Zhou and Yuanyuan Han. My research would not have been possible and fun without their kind support.

Finally, I want to thank my mother and sister. They have always been supportive of my decision to pursue Ph.D and encouraging when I feel frustrated. I owe all of my achievements to my family for their love and sacrifice.

Chapter 3 or portion thereof has been published in *AIP advances* (2011), Tsung-Feng Wu, Zhe Mei, Luca Pion-Tonachini, Chao, Zhao, Wen Qiao, Ashkan Arianpour and Yu-Hwa Lo. The dissertation author was the first author of the paper.

Chapter 4 or portion thereof has been published in Lab on a Chip (2012), Tsung-Feng Wu, Zhe mei, and Yu-Hwa Lo. The dissertation author was the first author of the paper.

Chapter 5 or portion thereof has been published in Sensors and Actuators B: Chemical (2013), Tsung-Feng Wu, Zhe Mei, and Yu-Hwa Lo. The dissertation author was the first author of the paper.

Chapter 6 or portion thereof will be submitted by Tsung-Feng Wu, Tony Minghung Yen, Yu-Jui Chiu, Yuanyuan Han, Yu Sheng Lin and Yu-Hwa Lo (2014). The dissertation author was the first author of the paper.

Vita

June, 2003	Bachelor of Science in Chemical Engineering National Cheng Kung University, Tainan, Taiwan
June, 2005	Master of Science in Materials Science and Engineering National Tsing Hua University, Hsinchu, Taiwan
March, 2010	Graduate Student Researcher Materials Science and Engineering Program University of California, San Diego
December, 2013	Doctor of Philosophy in Materials Science and Engineering Materials Science and Engineering Program University of California, San Diego

Journal Publications

1. Chih-Huang Lai, **Tsung-Feng Wu**, Ming-Der Lan, "Synthesis and Property of Core-Shell Ag@Fe_3O_4 Nanoparticles", ***IEEE Trans. Magn.*** 41, 3397-3399 (2005).

2. **Tsung-Feng Wu**, Zhe Mei, Luca Pion-Tonachini, Chao, Zhao, Wen Qiao, Ashkan Arianpour and Yu-Hwa Lo, "An Optical-Coding Method to Measure Particle Distribution in Microfluidic Devices", ***AIP advances***. 1, 022155 (2011)

3. Zhe Mei, **Tsung-Feng Wu**, Luca Pion-Tonachini, Wen Qiao, Chao Zhao, Ashkan Arianpour and Yu-Hwa Lo. "Applying an optical space-time coding method to enhance light scattering signals in microfluidic devices", ***Biomicrofluidics***, 5, 034116 (2011)

4. **Tsung-Feng Wu**, Zhe Mei and Yu-Hwa Lo, "Optofluidic device for label-free cell classification from whole blood", ***Lab on a Chip***, 12, 3791 (2012) *[featured as Key Scientific Articles in Global Medical Discovery]*

5. Yu Jui Chiu, Sung Hwan Cho, Zhe Mei, Victor Lien, **Tsung-Feng Wu**, and Yu-Hwa Lo, "Universally applicable three-dimensional hydrodynamics focusing embedded microfluidic flow design achieved by simple two-layer-fabricated technique," ***Lab on a chip***, 13, 1803 (2013)

6. **Tsung-Feng Wu**, Zhe Mei, Yu-Hwa Lo "Label-free Optofluidic Cell Classifier Utilizing Support Vector Machines", ***Sensors and Actuators B***, 186, 327 (2013)

7. **Tsung-Feng Wu**, Tony Minghung Yen,Yu Jui Chiu, Yuanyuan Han, Yu Sheng Lin and Yu-Hwa Lo, "Label-free reconstruct the signature of cellular nucleus by using scattering-imagin-based cytometer," to be submitted (2014)

8. **Tsung-Feng Wu,** Sung Hwan Cho, Ian Quigley and Yu-Hwa Lo, "Circulating tumor cells captured by lab-on-a-chip systems" in preparation

Conference Proceedings

1. **Tsung-Feng Wu**, Chien-Hsin Ho, Chih-Huang Lai, Ming-Der Lan "Synthesis and Property of Core-Shell Ag@Fe_3O_4 Nanoparticles", poster, **IEEE International Magnetics Conference**, Nagoya (Japan), April 4-8, 2005

2. **Tsung-Feng Wu**, Chien-Hsin Ho, Chih-Huang Lai "Shape-Induced Anisotropy of Fe_3O_4 Nanocubes", oral presentation, **52nd Conference on Magnetism & Magnetic Materials**, Tampa (USA), November 10-14, 2007

3. **T.-F. Wu**, Z.Mei, L. Pion-Tonachini, C. Zhao, W. Qiao, A. Arianpour and Y.-H. Lo "An Optical-Coding Method for Scattering Signal Detection in Microfluidic Cytometers", poster, **Micro Total Analysis System**, Seattle (USA), October 2-6, 2011

4. **T.-F. Wu**, Zhe Mei, Luca Pion-Tonachini and Yu-Hwa Lo "Microfluidic Flow Cytometer Utilizing Optical Space-Time Coding Technique", oral presentation, **IEEE photonics 2011 conference**, Arlington (USA), October 9-13, 2011

5. Zhe Mei, Sung Hwan Cho, Arthur Zhang, Jie Dai, **Tsung-Feng Wu** and Yu-Hwa Lo "Counting leukocytes from whole blood using a lab-on-a-chip Coulter counter", oral presentation, **IEEE Engineering in Medicine and Biology Society (EMBC)**, San Diego (USA), August 28-September 1, 2012

6. **Tsung-Feng Wu**, Zhe Mei, Yu-Hwa Lo "Label-free Optofluidic Cell Classifier Utilizing Support Vector Machines", **IEEE Healthcare Innovation Conference**, poster, Houston (USA), Nov 7-9 2012

7. **Tsung-Feng Wu**, Zhe Mei, Yu-Jui Chiu, Sung Hwan Cho, Yu-Hwa Lo "Rapid White Blood Cell Detection for Peritonitis Diagnosis ", oral presentation, **SPIE West**, San Francisco (USA), Feb 2013

Book Chapters

1. **Tsung-Feng Wu**, Sung Hwan Cho, Yu-Jui Chiu, Yu-Hwa Lo "*Lab-on-a-chip device and system for point-of-care applications*", edited by Aaron H.-P. Ho, Donghyun Kim and Michael G. Somekh, Springer, 2014, to be published

2. **Tsung-Feng Wu**, Qiao Wen, Yu-Jui Chiu, Yu-Hwa Lo "*Optofluidic lab-on-a-chip devices for photomedicine applications*," edited by Michael R Hamblin, Woodhead Publishing Ltd, 2014, submitted

3. **Tsung-Feng Wu**, Yu-Hwa Lo "*Optofluidic device for label-free cell classification from whole blood*," edited by Avi Rasooly, Humana Press, 2014, submitted

Patent

1. Yu-Hwa Lo, **Tsung-Feng Wu**, Zhe Mei "*OPTICAL SPACE-TIME CODING TECHNIQUE IN MICROFLUIDIC DEVICES*", US Patent pending, 20130016335

ABSTRACT OF THE DISSERTATION

Label-free lab-on-a-chip flow cytometer for biomedical applications

by

Tsung-Feng Wu

Doctor of Philosophy in Materials Science and Engineering

University of California, San Diego, 2013

Professor Yu-Hwa Lo, Chair

This dissertation demonstrates the development of a portable and low cost lab-on-a-chip flow cytometer, in which various methods are applied to achieve label-free detections for rapid, accurate and high performance point-of-care applications. This work is based on the measurement of scattering light from cells or beads in the microfluidic channel to either collect scattering signals or image scattering light.

An optical-coding technique is proposed to enhance the cell classification and minimize the cost with the compact form. The encoded scattering signals are collected by off-the-shelf PIN photoreceivers. The spatial distribution of cells or beads in the microfluidic channel can be readily extracted with the specific waveform. Although the

theory of the inertial effect can explain the spatial distribution of objects with different sizes, the stiffness of cells is found to play a role on the distribution. The stiffness of cells can be used as an effective biomarker for cell classification. Moreover, with the aid of machine learning algorithms, the optical-coding technique can be expanded to proceed a multi-dimensional analysis, which further enhances the performance of the microfluidic flow cytometer.

Recently, the study of sub-cellular structure has drawn more attention because the size and shape of cellular nucleus carry important information about biological activities such as apoptosis, cell cycle, cancerous metastasis, etc. However, current technologies have only used labeling technique to image cell nuclei for further observation. Another part of this work is to build up a label-free technique to unambiguously retrieve the information of cell nucleus, more importantly, by using widely available CMOS imagers. The scattering-imaging-based cytometer is demonstrated to record the scattering images from cancer or human white blood cells. The signature of cells can be graphically established to represent the size, shape and orientation of cell nucleus.

Such a low-cost, compact, portable lab-on-a-chip cytometer platform can be easily afforded by individual clinics and research labs, satisfying point-of-care diagnosis and telemedicine applications. The development executed in this dissertation is aiming to improve the global health and lead a better life for human beings.

Chapter 1

Introduction – Optofluidic lab-on-a-chip device and flow cytometer

In the past decades, the great advance of lab-on-a-chip device has been shown to address the increasing needs for biomedical study and clinical tests. The pursuits of developing less expensive, compact and portable lab-on-a-chip devices could bring significant improvement on the life quality of people who live in the developing country or suburban area. For example, people in Africa or Asia are suffering from such as

HIV/AIDS or malaria, etc., and deficit of rapid diagonstics results in the high death rate of lives. Therefore, the demands of point-of-care healthcare have tremedously driven the development of lab-on-a-chip devices.

In this chapter, the concept of optofluidic devices will be introduced first, followed by the principal of various techniques such as labeled and label-free detection. The brief literature survey on the advancements of optofluidic devices for biological applications will be also included.

1. 1. Optofluidic lab-on-a-chip device

Optofluidic, a term first named in 2003,[1] represents a technique that can synergistically operate fluidics and optics for analyzing biological and chemical samples.[2-4] A wide range of principles of optics such as Raman scattering, fluorescence, refractive index, adsorption, etc.,[5-10] have been applied to detect and analyze various biological samples in the fluid. The signals or images obtained are then used to resolve the size, shape, granularity, and physical, chemical, and biological properties of samples. Taking the advantage of development of microfabrication techniques, since last decade the miniaturization of fluidics has led to the creation of the field of microfluidics, and a further advancement on the integration of optical components and features allows microfluidic device to detect, excite and manipulate particles or cells in microfluidics. Since then, optofluidics, being identified as a specific branch of the general field of microfluidics, is extensively recognized by the increasing number of publications that specifically define themselves as “optofluidics.”

To detect partciles in optofluidic devices, the guidance of light within the device is important. The optical waveguides are the general approaches to confine and guide the incident light by total internal reflection. For most optofluidic devices, the polymer material, polydimethylsiloxane (PDMS), is generally adopted for the fabrication of devices because PDMS is easy to be shaped with desired feature by so-called soft lithography process, which will be discussed in Chapter 2. Also, with the aid of capillary filling method, the integrated optical waveguides that have a higher refractive index PDMS (n≈1.42) as the "core" channel and a lower refractive index PDMS (n≈1.407) as the cladding channel have been demonstrated by Lien et al.[11, 12] to guide the light through the total reflection. The liquid-to-liquid core-cladding waveguide[13,14] and liquid-core/air-cladding waveguide[15, 16] have been proposed to deliver light through the microchannel; however, the difficulty of flow control between both fluid layers results in thhe inefficient light guidance. Recently a low refractive index solid material, Teflon AF (Dupont Inc.), is used as the cladding layer to provide better light confinement within microfluidic channel. Because Teflon AF is chemically stable and optically transparent from UV to IR, a coating layer of Teflon AF as the cladding layer would not influence cell viability and signal detection. Cho et al. [17] have implemented Teflon AF layer coating on the wall of PDMS microchannels. Teflon AF-coated waveguides provide excellent light confinement within the liquid core where the biological samples flow though, thus offering a convenient, low loss design for optical excitation along the flow channel. One salient feature of the optofluidic waveguide design is to allow multiple points of detection because the guided excitation light follows the travel of

particles. In the conventional setup, laser beam is focused to only one excitation spot and multi-point detection not only reduces the light intensity by power splitting but also increases the complexity, size, and cost of optics tremendously.

We next discuss lab-on-a-chip devices, especially microfluidic flow cytometers because of its importance for optofluidic devices. The purposes of lab-on-a-chip (LOC) devices are to reduce the required amount of sample for analysis, increase the sensitivity of detection and provide a better bio-safety environment. The feature dimensions of LOC devices are typically around few hundred microns and the entire devices have to be portable.

As mentioned, people have been applying optical detection on the analysis of biological samples. Among these applications, the flow cytometer is one of the most powerful tools for the characterization of cells because the flow cytometer is able to introduce a continuous sample flow within the channel that promises the high throughput examination to achieve rapid analysis. In the flow cytometer system, an external light source is implemented to interrogate the flowing sample within the channel. The physical and biological properties of samples could be realized, depending on their optical responses such as forward scattering (FSC), side scattering (SSC) and fluorescence (FL). The optical signals are stored and then processed with a computation system to retrieve the quantitative data. Figure 1.1 shows a scheme of the traditional benchtop flow cytometry, consisted of a fluidic system with sheath flow confinement, an optical system to illuminate and collect signals, a sorting component, if necessary, to

isolate desired samples from the original sample mixture and an electronics system for data analysis.[18]

In order to address the rapid and point-of-care clinical tests, the miniaturization of flow cytometer is required. Following the principal of benchtop flow cytometers, the LOC flow cytometer is designed to have hydrodynamic flow confinement systems, which center the sample flow and allow an optical system to interrogate for signal collection. This type of flow focusing is only 2-dimensional confinement because the vertical direction, normal direction to the flow plane, is not focused, which might allow the variation of velocity and distribution of particles and thus cause the inferior performance of LOC flow cytometers to a conventional benchtop flow cytometer. Another, the device materials of LOC devices is usually PDMS, which has a porous surface and thus generate the scattering center. In this dissertation, we will demonstrate an optical-coding optofluidic LOC device that allows high throughput cell measurement and reduce noise by algorithm optizmiation.

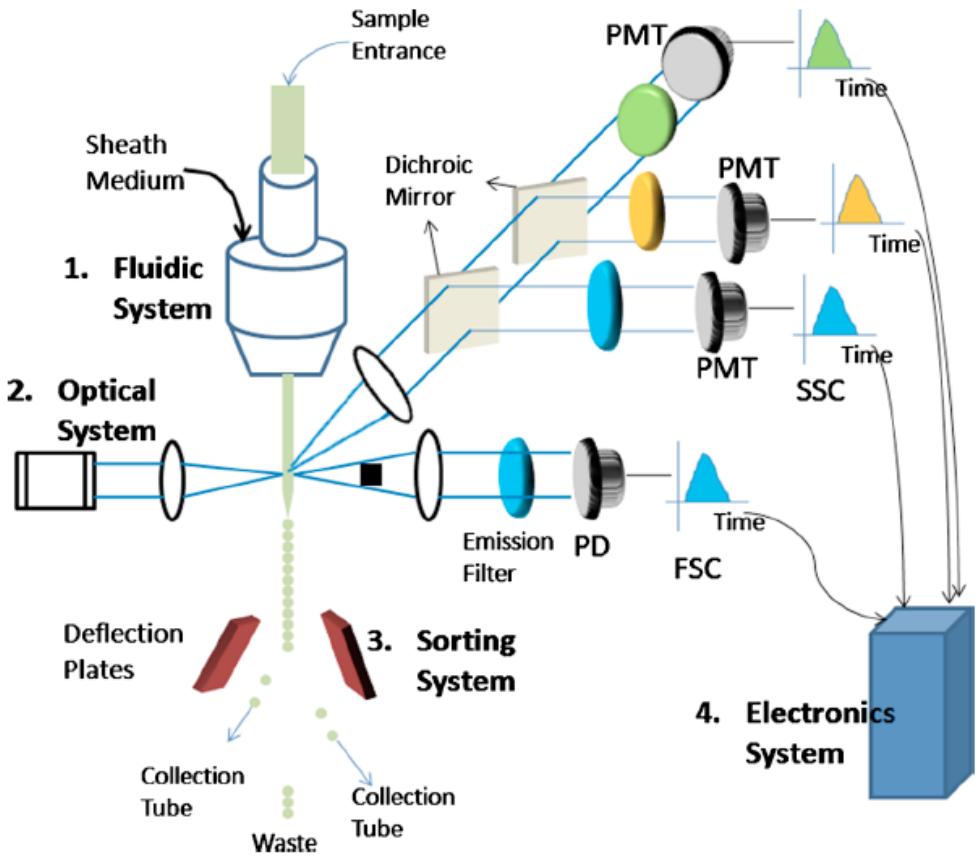

Figure 1.1 Schematic of a FACS system that can sense two scattered signals (forward scattering and side scattering) and two distinct fluorescent signals excited by an external laser source. The system contains (1) a fluidic system, (2) an optical system, (3) a sorting system and (4) an electronic control system for data collection and processing.[18]

1. 2. Labeled and label-free optpfluidic devices for biomedical applications

As in any in-vitro bio-sensing techniques, optofluidic devices for biomedical detection can be classified into two categories, labeled and label-free detection. The label-free technique produces signals from samples without attaching fluorescent dyes,

quantum dots, or beads to the samples.[19-21] On the other hand, labeled detection binds fluorescent dyes, proteins, or beads [22-24] to samples so the signals are generated from the labels rather than the samples themselves. The label-free technique offers lower cost and faster results and is generally more desirable as long as feasible. However, the labeled detection still dominates the field today because it provides more specific and accurate detection for most applications. We will briefly discuss these two approaches here.

Labeled detection

A wide range of labeled detection techniques are omnipresent in the fields of biology and biomedicine. Although these methods require extra sample preparation steps compared to the unlabeled methods, they usually have higher detection sensitivity, accuracy, and specificity. We introduce a few commonly used labeled detection techniques in this section.

On-chip fluorescence detection

Fluorescence detection is the most popular method to identify and enumerate cells and investigate their physical and biochemical properties. In conventional fluorescence detection settings, however, bulky peripheral setup is necessary. For example, a fluorescence microscope requires bulky lasers and optical components such as beam splitters, dichroic mirrors, optical filters and photo-detectors. This becomes an obstacle when deploying lab-on-a-chip fluorescence detection systems for point-of-care needs, particularly in less developed countries and areas.

In order to reduce the cost, size, and complexity of the fluorescence detection systems, researchers have tried to integrate some key optical components to create monolithic optofluidic systems. For example, waveguides and lenses[14, 25, 26] have been integrated to collect and guide fluorescence signals to the detector array that is also integrated on the same chip. The integrated waveguides can also bring excitation light to the interrogation zone of microfluidic channels. In addition, on-chip lenses to collimate the excitation beam and to collect signals from fluorescently labeled cells have been used, thus removing the need for off-chip lenses. Since the lenses, waveguides and the channels are pre-aligned lithographically on a chip, the approach of on-chip illumination and detection assures precise alignment even in environments of constant motions and vibrations. The microfabrication of on-chip lenses enables the design of customized lens profiles such as aspherical lenses at much lower cost than conventional fabrication methods for aspherical lenses such as diamond turn. More recently, researchers have demonstrated optofluidic devices with tunable optical components. The curvature of lens is controlled by the flow ratio between the core stream and the cladding stream. Tang *et. al.*[27] demonstrated on-chip tunable lenses, where the curvature of the tunable liquid lens can be controlled by adjusting the rates of the sample flow (e.g. the core stream) and the sheath flow (e.g. cladding stream).[27] Xiongs *et. al.* created an on-chip optofluidic prism capable of separating multiple fluorescence emission wavelengths.[28] In combination with on-chip detector arrays, the optofluidic prism can significantly reduce the optical path from fluorescently labeled targets to detector arrays. The

interface between the two liquids is optically smooth and the potential light loss is also minimized in those configurations.

Other researchers pushed the concept even further, developing on-chip integrated fluorescence filters by adding fluorescence dyes into PDMS layer.[29, 30] By mixing certain dyes or even food colors, they demonstrated various optical band-pass and long-pass filters. Adjusting the concentration and composition of dye-additives and controlling the thickness of the layer can precisely engineer the optical cut-off wavelengths and transmission spectra. For point-of-care applications, microfluidics devices that can measure the absolute number of CD4+ and percentage of CD4 counts in patient blood have been demonstrated by various research groups.[31]

Fluorescently labeled detection on chip – flow and image cytometers

There are several ways to fluorescently label or stain cells: antibodies or proteins tagged with a fluorochrome(s), protein or DNA conjugated quantum dots or nanoparticles, to name a few. Conventional flow-based or image-based systems are bulky, expensive, and complicated to operate, thus producing the incentives of developing microfluidic versions of flow cytometers for point-of-care clinical applications.

Microfluidic image cytometer (MIC)

Microfluidic image cytometry (MIC) that combines the advantages of microfluidics and microscopy-based cytometry is capable of quantitative, single-cell

proteomic analysis of multiple signaling molecules using small number of cells.[32] Together with advanced bioinformatics analysis, the MIC platform enables *in-vitro* molecular diagnostics for pathology analysis, and personalized medicine in the future. Schonbrun *et al*. have explored a new way of performing imaging flow cytometry to overcome low screening throughput by exploiting parallel microfluidic channels and using diffractive lenses, which enables higher throughput or high quality image of single cells.[33, 34] They recently imaged red blood cells and acute leukemia cells at high screening throughput up to 20,000 cells per second. The MIFC has a high imaging resolution of sub-cellular features to give information about microbial infection of cells. Though only bright-field imaging was demonstrated, fluorescence imaging may be integrated in the near future.

Label-free detection

Based on the properties of samples one wants to detect, label-free detection mainly includes light scattering, Raman scattering and surface plasmon resonance. Each detection technique can be utilized individually or in combination to collect differentiable signals. In the present dissertation, we will merely implement scattering measurement as our label-free detection, which will be discussed in the following chapters.

Light scattering

The measurement of light scattering is relatively straightforward for optofluidic sensors. When particles suspended in the fluid are interrogated with an external light source, the refractive index difference between particles and fluid medium or the refractive index difference of organelles within the cells can generate scattering signals. The intensity of scattering light is determined by the refractive index difference as well as the size, shape and orientation of cells.[35-37] Therefore, light scattering signals can be used to identify cells or particles. The scattering signals are usually collected at two different angles. The scattering close to the incident light beam is known as the forward scattering (FSC) signal, and the scattering at 90-degreee from the incident light is referred to side scattering (SSC) signal.

The forward scattering signal can be used to retrieve the particle size since it is measured at small angles (0.5~5°) from the incident light source and its intensity is related to the volume of the particle in the flow medium. In some scenarios, the shape of cells in the fluid medium is not spherical so the orientation of cells might cause different forward scattering signals. The intensity of side scattering reveals information about the intracellular structures and is particularly sensitive to the granularity and internal structures (e.g. mitochondrial) of the cells. Since the forward scattering and side scattering signals contain different information (i.e. size and granularity) of cells, they have been exploited for unlabeled cell classification in flow cytometers although with limited resolution. An on-chip integrated microfluidic flow cytometer with integrated waveguides for the collection of forward scattering, side scattering, large angle scattering and fluorescence signals has been demostarted.[38]

Raman Scattering

Raman spectroscopy is a technique that senses the spectrum to investigate vibrational and rotational modes of molecules. Raman scattering occurs when the incident light interacts with the electron cloud and molecular bonds and passes (receives) energies to (from) phonons. The energy shifts between the excitation light and scattered light due to Raman scattering carry information of rotational or vibrational state of molecules, which can be used for molecule detection or identification. However, as a third-order nonlinear optical effect, the efficiency of Raman scattering is very low so the intensities of Raman scattering is too weak for most applications. To address this problem, surface enhanced Raman spectroscopy (SERS) has been developed. The generally accepted theory for SERS is that the enhancement of Raman scattering is due to the concentrated electromagnetic field via metallic nanoparticles and molecular amplification (Raman probes). Combining both effects, the signals of Raman scattering can be drastically enhanced by a factor of 10^{14},[39, 40] although most reported data show a much lower yet still significant enhancement in Raman scattering efficiency. Piorek *et al*. presented a microfluidic device for sensitive and real-time detection using SERS.[8] This device can quantitatively monitor the extent of colloid aggregation based on the change of the SERS intensity and simultaneously observe the aggregation process of nanoparticles.

Surface plasmon resonance (SPR)

Surface plasmon represents modes of electron oscillations at the interface between the molecules and the metal surface and the resonant frequencies of oscillation are determined by the dielectric properties of metal and molecules. When the electromagnetic field from an external light source matches the electron oscillations in polarization and frequencies, strong coupling occurs between the surface plasmon and the incident light, revealing a light absorption peak at the resonant frequencies (wavelengths).[41, 42] Both the strength and the spectrum of the light absorption produce information about the concentration and characteristics of molecules (e.g. proteins) ligated to the functionalized metal surface. Currently, light is introduced to the interface between metal and analytes containing medium via a prism. To use the effect of surface plasmonics, the device generally uses the Kretschmann configuration,[43] where a metal thin film is directly deposited on a prism and the evanescent optical wave interacts with the metal film via the prism coupling to excite surface plasmons. When the wave vector or incident angle of light matches the wave vector of surface plasma, resonant coupling occurs to give rise to a strong absorption of the incident light. By monitoring the shift of incident angle for the resonant coupling and the strength of light absorption, one can obtain information about the concentration, reaction kinetics, and affinity of biological molecules as well as cell phenotype.[44]

Shan *et al*. also harnessed the surface plasmon effect in microfluidic devices to measure the surface charge density and particle heights.[45, 46] A modified layer of Au is deposited onto the glass. The concentration and size of particles on the surface influence the surface charge density and produce signals for sample identification. Wang *et al*.

have also demonstrated the surface plasmon resonance microscopy (SPRM) for label-free imaging, allowing detection and size measurement of single viral particles.[47]

1. 3. Overview

This dissertation discusses a few important achievements on developing label-free lab-on-a-chip platform flow cytometers by harnessing the novel optical-coding technique to encode the scattering light from cells. Besides, the scattering images of cells are also recorded by using microfabricated μlens that is first demonstrated to rapid scan scattering center within cells. The label-free lab-on-a-chip platforms described in this dissertation are all compact and portable to hold a promise for telecom healthcare applications.

Chapter 2 will discuss the conventional fabrication process of polydimethylsiloxane (PDMS) including the main process of manufacturing the optical-coding devices.

Chapter 3 will introduce the optical-coding technique for reconstruct the distribution of particles within microfluidic channel. The distribution of particles within the microchannel depends on the size of particles when the flow rate is increased to trigger the inertial effect. In the chapter 3, the principal of inertial effect will be discussed. Laser light was introduced from the bottom of LOC devices and encoded with the four trapezoidal slits, which were formed by depositing a layer of metal film on the glass substrate. The encoded incident laser beam would illuminate the particles or cells within the microchannel. A pair of PIN silicon photoreceivers was placed on top of

the LOC device to collect forward scattering and large angle scattering signals from particles, respectively. Followed by the custom algorithms, digital signal processing gave rise to extraction of spatial information of cells within microfluidic channel. By processing the encoded signals, the signal-to-noise ratio (SNR) can be significantly enhanced for further analysis. Chapter 3 or portion thereof has been published in *AIP advances* (2011), Tsung-Feng Wu, Zhe Mei, Luca Pion-Tonachini, Wen Qiao, Ashkan Arianpour and Yu-Hwa Lo, and *Biomicrofluidics* (2011), Zhe Mei, Tsung-Feng Wu, Luca Pion-Tonachini, Wen Qiao, Ashkan Arianpour and Yu-Hwa Lo.

Chapter 4 will introduce the application of the optical-coding technique on enumaeration of white blood cells from human whole blood. For the real biological samples like cells, the distribution of cells within the microchannel not only depends on the size of cells, but also relates to the stiffness of cells. It turns out that the stiffness of cells becomes ann effective biomarker for cell classification. Starting with blood sample preparation, the lysed white blood cells were introduced into the microfluidic channel at the high flow rate. We will demonstrate that the optical-coding LOC device can effectively enumerate neutrophils, a sub-population in white blood cell family, from whole blood. Chapter 4 or portion thereof has been published in *Lab on a Chip* (2012), Tsung-Feng Wu, Zhe Mei and Yu-Hwa Lo.

Chapter 5 will show an important feature of the optical-coding LOC device in cell classification. As discussed in the chapter 4, the stiffness of cells can play a role on the spatial distribution of cells and be used as a biomarker to further identify the cell phenotyping. In the traditional flow cytometer, if the label-free detection conducted,

only forward scattering and side scattering will be presented for cell classification. However, with the novel optical-coding technique, every single cell can carry the forward scattering as well as the two dimensional position over the channel cross-section. We introduced a machine-leanring method, called support vector machine, which can perform the multi-dimensional analysis to further enhance the sensitivity and specificity of cell classification. Chapter 5 or portion thereof has been published in *Sensors and Actuators B-Chemical* (2013), Tsung-Feng Wu, Zhe Mei, and Yu-Hwa Lo.

Chapter 6 will introduce an innovative method of the observation of cell scattering images. By fabricating a cylindrical μlens on the layer of metal film, which has 10 μm opening to focus the sheet of incident light, the nuclei of cells can be scanned to produce a series of scattering images. The bright spots that are believed to reflect the scattering center within cells (i.e. nuclei) are recorded with the conventional CMOS imager. The study of cell cycle was tested to demonstrate this technology. Moreover, the polymorphonuclear white blood cells and mononuclear white blood cells can be distinguished by using this scattering-image-based method. The cellphone-compatible technique allows a rapid route for biomedical applications such as 2-part white blood cell classification or malaria diagonstics.

Chapter 7 will summarize the present study and briefly overlook future works.

References:

1. V. R. Horowitz, D. D. Awschalom and S. Pennathur, Lab Chip 8 (11), 1856-1863 (2008).

2. X. D. Fan and I. M. White, Nat Photonics 5 (10), 591-597 (2011).

3. H. Schmidt and A. R. Hawkins, Nat Photonics 5 (10), 598-604 (2011).

4. D. Psaltis, S. R. Quake and C. H. Yang, Nature 442 (7101), 381-386 (2006).

5. S. H. Cho, C. H. Chen, F. S. Tsai, J. M. Godin and Y. H. Lo, Lab Chip 10 (12), 1567-1573 (2010).

6. J. Godin, C. H. Chen, S. H. Cho, W. Qiao, F. Tsai and Y. H. Lo, J Biophotonics 1 (5), 355-376 (2008).

7. L. Pang, H. M. Chen, L. M. Freeman and Y. Fainman, Lab Chip 12 (19), 3543-3551 (2012).

8. B. D. Piorek, S. J. Lee, J. G. Santiago, M. Moskovits, S. Banerjee and C. D. Meinhart, P Natl Acad Sci USA 104 (48), 18898-18901 (2007).

9. J. G. Wu, G. A. Zheng and L. M. Lee, Lab Chip 12 (19), 3566-3575 (2012).

10. C. Monat, P. Domachuk and B. J. Eggleton, Nat Photonics 1 (2), 106-114 (2007).

11. V. Lien, K. Zhao, Y. Berdichevsky and Y. H. Lo, Ieee J Sel Top Quant 11 (4), 827-834 (2005).

12. V. Lien, K. Zhao and Y. H. Lo, Appl Phys Lett 87 (19) (2005).

13. D. V. Vezenov, B. T. Mayers, D. B. Wolfe and G. M. Whitesides, Appl Phys Lett 86 (4) (2005).

14. D. B. Wolfe, R. S. Conroy, P. Garstecki, B. T. Mayers, M. A. Fischbach, K. E. Paul, M. Prentiss and G. M. Whitesides, P Natl Acad Sci USA 101 (34), 12434-12438 (2004).

15. J. M. Lim, S. H. Kim, J. H. Choi and S. M. Yang, Lab Chip 8 (9), 1580-1585 (2008).

16. J. M. Lim, S. H. Kim and S. M. Yang, Microfluid Nanofluid 10 (1), 211-217 (2011).

17. S. H. Cho, J. Godin and Y. H. Lo, Ieee Photonic Tech L 21 (15), 1057-1059 (2009).

18. A. R. Hawkins and H. Schmidt, Handbook of optofluidics. (Taylor & Francis, 2010).

19. A. Q. Liu, H. J. Huang, L. K. Chin, Y. F. Yu and X. C. Li, Anal Bioanal Chem 391 (7), 2443-2452 (2008).

20. H. Y. Zhu, I. M. White, J. D. Suter, M. Zourob and X. D. Fan, Analyst 133 (3), 356-360 (2008).

21. X. D. Fan, I. M. White, S. I. Shopova, H. Y. Zhu, J. D. Suter and Y. Z. Sun, Anal Chim Acta 620 (1-2), 8-26 (2008).

22. M. L. Chabinyc, D. T. Chiu, J. C. McDonald, A. D. Stroock, J. F. Christian, A. M. Karger and G. M. Whitesides, Anal Chem 73 (18), 4491-4498 (2001).

23. J. C. Roulet, R. Volkel, H. P. Herzig, E. Verpoorte, N. F. de Rooij and R. Dandliker, Anal Chem 74 (14), 3400-3407 (2002).

24. L. Novak, P. Neuzil, J. Pipper, Y. Zhang and S. H. Lee, Lab Chip 7 (1), 27-29 (2007).

25. J. Seo and L. P. Lee, Sensor Actuat B-Chem 99 (2-3), 615-622 (2004).

26. J. Godin, V. Lien and Y. H. Lo, Appl Phys Lett 89 (6) (2006).

27. S. K. Y. Tang, C. A. Stan and G. M. Whitesides, Lab Chip 8 (3), 395-401 (2008).

28. S. Xiong, A. Q. Liu, L. K. Chin and Y. Yang, Lab Chip 11 (11), 1864-1869 (2011).

29. S. H. Cho, W. Qiao, F. S. Tsai, K. Yamashita and Y. H. Lo, Appl Phys Lett 97 (9) (2010).

30. C. L. Bliss, J. N. McMullin and C. J. Backhouse, Lab Chip 8 (1), 143-151 (2008).

31. D. S. Boyle, K. R. Hawkins, M. S. Steele, M. Singhal and X. H. Cheng, Trends Biotechnol 30 (1), 45-54 (2012).

32. J. Sun, M. D. Masterman-Smith, N. A. Graham, J. Jiao, J. Mottahedeh, D. R. Laks, M. Ohashi, J. DeJesus, K. Kamei, K. B. Lee, H. Wang, Z. T. F. Yu, Y. T. Lu, S. A. Hou, K. Y. Li, M. Liu, N. G. Zhang, S. T. Wang, B. Angenieux, E. Panosyan, E. R. Samuels, J. Park, D. Williams, V. Konkankit, D. Nathanson, R. M. van Dam, M. E. Phelps, H. Wu, L. M. Liau, P. S. Mischel, J. A. Lazareff, H. I. Kornblum, W. H. Yong, T. G. Graeber and H. R. Tseng, Cancer Res 70 (15), 6128-6138 (2010).

33. E. Schonbrun, A. R. Abate, P. E. Steinvurzel, D. A. Weitz and K. B. Crozier, Lab Chip 10 (7), 852-856 (2010).

34. E. Schonbrun, S. S. Gorthi and D. Schaak, Lab Chip 12 (2), 268-273 (2012).

35. J. Godin and Y. H. Lo, Biomed Opt Express 1 (5), 1472-1479 (2010).

36. A. Karlsson, J. P. He, J. Swartling and S. Andersson-Engels, Ieee T Bio-Med Eng 52 (1), 13-18 (2005).

37. N. Pamme, R. Koyama and A. Manz, Lab Chip 3 (3), 187-192 (2003).

38. V. L. J. Godin, Y. Lo, (19th Annual Meeting of the IEEE Lasers and Electro-Optics Society (Montreal, Quebec, 2006), 2006), pp. 605–606.

39. K. Kneipp, H. Kneipp, V. B. Kartha, R. Manoharan, G. Deinum, I. Itzkan, R. R. Dasari and M. S. Feld, Phys Rev E 57 (6), R6281-R6284 (1998).

40. K. Kneipp, Y. Wang, H. Kneipp, L. T. Perelman, I. Itzkan, R. Dasari and M. S. Feld, Phys Rev Lett 78 (9), 1667-1670 (1997).

41. B. Liedberg, C. Nylander and I. Lundstrom, Biosens Bioelectron 10 (8), R1-R9 (1995).

42. B. Liedberg, I. Lundstrom and E. Stenberg, Sensor Actuat B-Chem 11 (1-3), 63-72 (1993).

43. E. Kretschmann and E. Kroger, J Opt Soc Am 65 (2), 150-154 (1975).

44. Y. C. Tung, N. T. Huang, B. R. Oh, B. Patra, C. C. Pan, T. Qiu, P. K. Chu, W. J. Zhang and K. Kurabayashi, Lab Chip 12 (19), 3552-3565 (2012).

45. X. N. Shan, K. J. Foley and N. J. Tao, Appl Phys Lett 92 (13) (2008).

46. X. N. Shan, X. P. Huang, K. J. Foley, P. M. Zhang, K. P. Chen, S. P. Wang and N. J. Tao, Anal Chem 82 (1), 234-240 (2010).

47. S. P. Wang, X. N. Shan, U. Patel, X. P. Huang, J. Lu, J. H. Li and N. J. Tao, P Natl Acad Sci USA 107 (37), 16028-16032 (2010).

Chapter 2

Fabrication of the optical-coding lab-on-a-chip device

In the chapter 2, the process of fabricating the optical-coding lab-on-a-chip flow cytometers will be covered. We used soft-lithography method to rapid fabricate the prototype of microfluidic devices. Two main steps of fabricating the optical-coding

microfluidic device are required: (1) Deposition of a layer of metal film with four trapezoidal slits on the glass slide, (2) Fabrication of SU-8 mold on the silicon wafer.

2. 1. Deposition of the metal film

Mask silts design is first layouted with Autocad software and printed out with high resolution. The layout of device is drawn by AutoCAD and printed out on the transparent mask (CAD/Art Services, Inc., Oregon, USA). Four transparent trapezoidal slits are designed to be arranged alternatively, wherein the individual trapezoidal slit has its base lengths of 50 μm and 100 μm and separates by 50 μm from each other silt to form a sensing area of pattern length of 450 μm.

A negative photoresist, NR9-1500, is spun on a 1 × 2 inches glass substrate at the speed of 4000 rpm for 30 seconds. After the soft bake at 150°C for 1 minute, the glass slide is exposed under I-line for 90 seconds. As-exposed glass slide is placed on the hotplate at 100°C for 1 minute, followed by immersing the slide in the developer solution for 6 seconds. Rinse with deionized water.

The sputtering (Denton Discover 18) is applied to form a spatial mask. A thin layer of Ti/Au (100nm/200nm) metal film is deposited on the glass with patterned photoresist, followed by the lift-off process to form the transparent four slits.

2. 1. Fabrication of SU-8 mold for PDMS replica

To date, the soft-lithography process[1] is widely adopted in most research labtoaries not only because of the low process cost but also due to its fast prototyping.

Soft lithography is meant reduce the use of photoaligner and enhance the fabrication efficiency for microdevice manufacturing, as shown in Figure 2.1. In this thesis, a microfluidic channel is designed as a 5 cm long straight channel and has a channel width of 100 μm with one inlet for sample introduction and one outlet for the exit. The layout of device is drawn by AutoCAD and printed out on the transparent mask (CAD/Art Services, Inc., Oregon, USA).

A negative photoresist, SU8-2050, is spun on a 4-inch mechanical silicon wafer at the speed of 3500 rpm for 40 seconds. The soft bake is required for as-spun wafer, which is placed on the hotplate at 65°C for 3 minutes and then heated to 95°C for 6 minutes. After cooling down to 65°C from 95°C, the wafer is exposed with the dosage of 150mJ/cm^2 with (I-Line) MA-6 photoaligner. The designed pattern is photolithographically transferred from the transparent mask onto the photoresist. The wafer is placed on the hotplate at 65°C for 1 minute and then heated to 95°C for another 6 minutes for post exposure bake, followed by cooling down to 65°C. The SU-8 developer is used to remove unexposed photoresist, followed by rinsing with isopropyl alcohol (IPA) and deionized water. One has to notice that if a white film produced when rinsing with IPA rinse, the unexposed photoresist is underdeveloped. Re-immersing the wafer with additional SU-8 developer is needed to remove the white film and complete the development process, followed by repeating the rinse step. The as-developed wafer is placed in the oven and heated to 150°C for 30 minutes. This hard bake process can increase the adhesion between SU-8 and silicon wafer as well as the mechanical property of SU-8 mold. The thickness of final SU-8 mold is measured to be 45 μm.

Once SU-8 mold is fabricated, Polydimethylsiloxane (Sylgard 184, Dow Corning), is mixed with the curing agent at the weight ratio of 15:1. The pre-polymer mixture is poured onto the SU-8 mold on silicon wafer and baked in the oven at 60°C for 4 hours. The PDMS replica can be easily cut off with the blazer for further use.

To assemble the microfluidic device, PDMS replica and the patterned glass slide are both treated with ozone plasma for 3 mintues. After treatment, with careful alignment under the stereomicroscope, the PDMS replica can be bonded onto the patterned glass slide to form the microfluidic device.

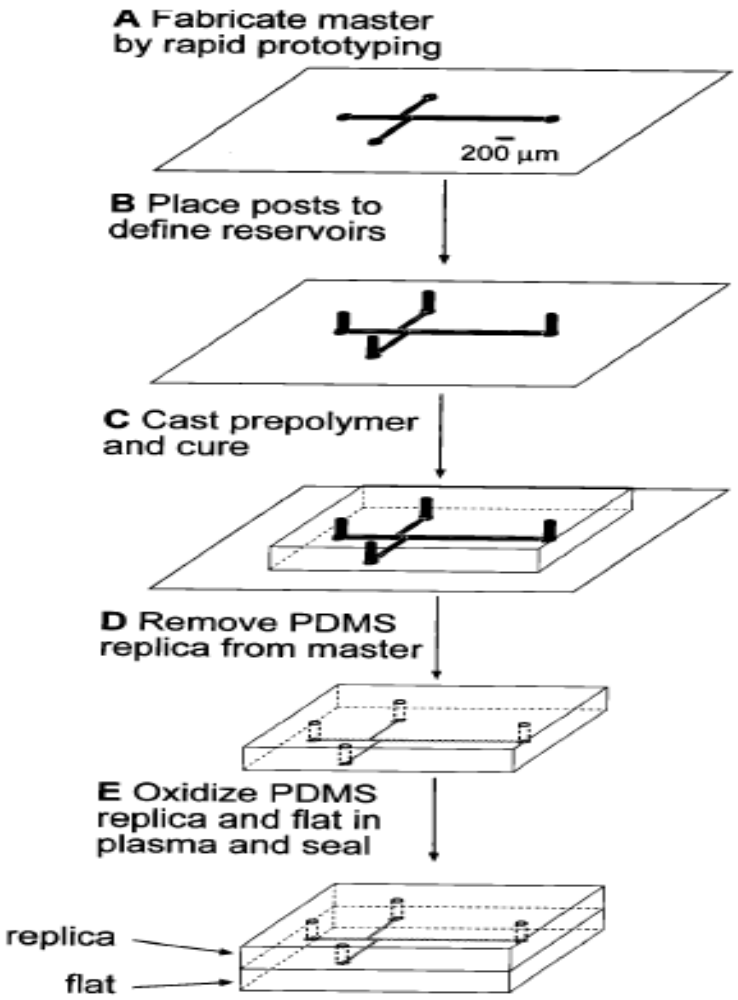

.

Figure 2.1 Schmetaic of fabrication of the microfluidic device by using soft lithography process .[2]

.

References:

1. D. Qin, Y. N. Xia and G. M. Whitesides, Nat Protoc **5** (3), 491-502 (2010).

2. J. C. McDonald, D. C. Duffy, J. R. Anderson, D. T. Chiu, H. K. Wu, O. J. A. Schueller and G. M. Whitesides, Electrophoresis **21** (1), 27-40 (2000).

Chapter 3

Optical-coding lab-on-a-chip device to enhance sensitivity and measure particle distribution in the microfluidic channel

In this chapter, we demonstrated an "optical space-time coding method" that can be applied to microfluidic devices to detect the forward and large angle light scattering signals for unlabelled bead and cell detection. Because of the enhanced sensitivity by this method, silicon pin photoreceivers can be used to detect both forward scattering (FS)

and large angle (45–60°) scattering (LAS) signals, the latter of which has been traditionally detected by a photomultiplier tube. This method yields significant improvements in coefficients of variation (CV), producing CVs of 3.95% to 10.05% for FS and 7.97% to 26.12% for LAS with 5, 10 and 15 μm beads. These are among the best values ever demonstrated with microfluidic devices.

Furthermore, the optical coding method can reconstruct the position of each particle in a microfluidic channel. The technique utilizes a specially designed pattern as a spatial mask to encode the forward scattering signal of each particle. From the waveform of the forward scattering signal, one can obtain the information about the particle position and velocity. The technique enables us to experimentally investigate the complex relations between particle positions within the microfluidic channel and flow conditions and particle sizes. The method also produces insight for important phenomenon in microfluidic and lab-on-a-chip devices such as inertial focusing, Dean flow, flow confinement, etc.

3. 1. Introduction

The enumeration and differentiation of particles based on optical detection in microfluidic devices has attracted significant attention because the optofluidic technology promises cheaper, portable, and easy-to-use devices for research, clinical, environmental, and industrial applications.[1-3] In general, particles that suspended in a microfluidic channel are guided in a stream to a sensing area where optical scattering, fluorescence, and Raman signals as well as electrical signals such as impedance are used

to interrogate the intrinsic properties of the sample. Depending on the signals of interest, the separation methods of particles based on hydrodynamic, dielectrophoretic, optical, acoustic, or magnetic mechanisms may be faciliated to guide the particles to the desired downstream exits, a function called cell sorting to isolate subpopulations of cells from the biological sample.[4, 5] For the purposes of either sample analysis or cell sorting, the most critical step is to detect intrinsic properties of each particle, especially for single-cell analysis in contrast with detection of the average properties of an ensemble. In this chapter, FS and LAS or side-scattering (SS) signals are the most widely used signals for bead and cell analysis since these signals indicate the size, shape, and granularity of each single particle without adding complexity, cost, and potentially bias to the subjects, caused by labeling steps. However, in the reality, the intensity of side scattering signals are serveral orders weaker and usually detected by photomultiplier tubes (PMTs) which require high voltage (>1000 V) operation and are costly and fragile, not suitable for point-of-care clinics. Besides, for most measurement with using microfluidic or lab-on-a-chip devices, the positions of samples within the microchannels can significantly affect the quality of signals such as the value of CVs. Should the device be used to separate or isolate certain subpopulations of cells or particles, the precise control of sample positions inside the channel becomes especially important.

To control and manipulate the positions of samples inside microchannels, a wide range of approaches for positioning particles have been explored. The current methods for positioning samples can be categorized into sheath and sheathless focusing approaches.[6] Sheath focusing employs sheath fluids to narrow sample flows. Although

highly effective, the design tends to have a relatively low throughput which could become a concern for cell sorting or cell counting.[7] Also for most microfluidic devices, sheath flow confines the particles in the in-plane direction but requires special designs and more complex processes to achieve particle confinement in the out-of-plane direction. To significantly increase the throughput for applications that require a large volume of samples such as milliliters of whole blood or body fluid, sheathless approaches have been actively investigated. To control particle behaviors in a sheathless design, an external force can be applied to move particles to the reestablished equilibrium positions through dielecrophoretic (DEP) effects,[8] acoustic effects,[9] or inertial effects induced by the balance between lift and drag forces.[10] Among these mechanisms, devices using inertial focusing are perhaps the simplest to fabricate because inertial focusing does not require additional electrodes and external signals to guide the suspended particles in the microfluidic channels. However, for all the sheath and sheathless methods that control the particle distribution in the flow, there is no experimental technique, to accurately and non-invasively measure the particle distribution over the channel area under different flow conditions and particle sizes. Researchers usually simulated the particles distribution by using the computational fluid dynamics (CFD) tools such as FLUENT and COMSOL, but these tools have limited capabilities to simulate how real bioparticles are distributed inside the microchannel because of the highly complicated physics and mathematics involved when particles are added to the flow medium in the simulation.

In this chapter, we demonstrate an optical coding method to measure the position of each particle in a microfluidic channel. Both forward (5–10°) and large angle (45-60°) scattering signals are respectively collected by using a pair of commodity Si PIN photoreceivers (PDA36A, Thorlabs) instead of sophisticated PMTs. The technique utilizes a specially designed pattern as a spatial mask to encode the forward scattering signal of each particle. From the waveform of the forward scattering signal, one can obtain the information about the particle position and velocity. Due to the fact that FS and LAS of each individual particle have to occur simultaneously, the signal-to-noise ratio of LAS can be digitally improved by custom-written MATLAB algorithms. The technique enables us to experimentally investigate the complex relations between particle positions within the microfluidic channel and flow conditions and particle sizes. The method also produces insight for important phenomenon in microfluidic and lab-on-a-chip devices such as inertial focusing, Dean flow, flow confinement, etc.

3. 2. Device design and space-time-coding technique

In this section, we present the design of an optical-coding technique to obtain the position and velocity information of particles within microchannels. Also, the principal of space-time-coding technique that we rely on to create the distribution of particles within microfluidic channel is described. The forward scattering signal of each individual particle is encoded by a spatial filter designed in such a way that both the position and velocity of each particle can be obtained from the waveform of the forward scattering signal. To prove the concept, as mentioned in Chapter 2, soft lithography was

used to fabricate the microchannels in polydimethylsiloxane (PDMS, Sylgard 184, Dow Corning) bonded to a glass substrate. As shown in Fig. 3.1, the microfluidic channel is 5 cm long and has a cross-section of 100 μm × 45 μm (width × height). Over the area where the forward scattering signals and large angle scattering signals were detected, we formed a pattern of four transparent trapezoidal slits that were created lithographically using 100 nm of Ti and 200 nm of Au on the glass substrate as a spatial mask. Thus the scattering signals of a particle displayed a specific waveform according to the lateral position the particle travels through, as illustrated in Fig. 3.2. Each trapezoidal slit has its base lengths of 100 μm and 50 μm. Fours slits were separated by 50 μm between each other and located 4.5 cm from the inlet. In our experiments that will be discussed in the next section, the sheath flow can be optionally turned on to compare to the results of the inertial effect. Fig 3.3 shows the sensing area image of assembly device taken by a CCD camera.

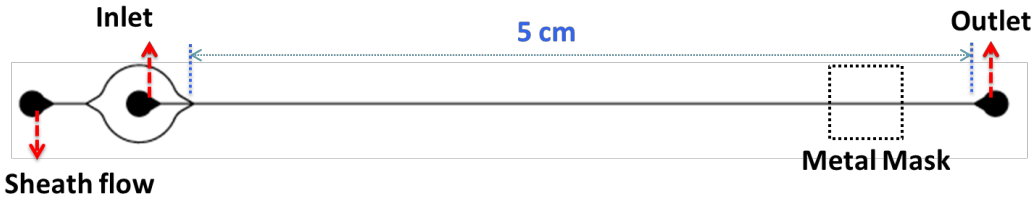

Figure 3.1 Design layout of the optical-coding microfluidic device. The microfluidic device has a 5-cm long straight microchannel and a cross-section of 100 × 45 μm (width × height). As designed, the device body has one inlet for the introduction of samples with one opening for optional sheath flow. On the downstream, the metal mask area is indicated with dash line, which will be illustrated clearly in Figure 3.2. After the interrogation, the fluid will come out from the outlet.

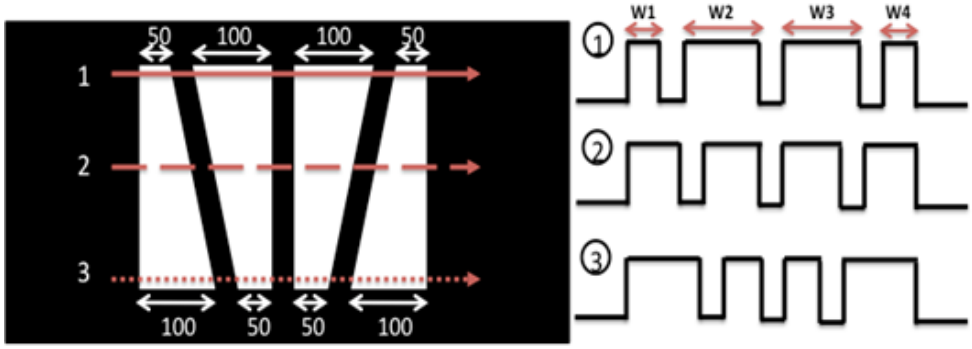

Figure 3.2 An illustration of spatial pattern for optical coding. Three representative forward-scattering signals are shown for particles travelling through different positions of the microfluidic channel. Each trapezoidal slit has its base lengths of 100 μm and 50 μm. The width of each peak, *W1* through *W4*, in the signal is used to acquire the position of particles along the *x*-direction. The method to find the position along the *y*-direction will be discussed later.[11]

Figure 3.3 The image of the sensing area under CCD camera, indicating the uniform illumination is applied over the four slits to allow the incident light to be encoded.

The space-time-coding technique thourghout this thesis represents the conversion of spatial information of particles within the microchannel into the the temporal spectrum collected by photoreceivers, as shown in Fig. 3.4. Because of the unequal width for each slit, the particles will produce forward scattering signals with 4 peaks of different widths in time domain. The position of each particle along the *x*-axis is determined by the width ratio of the first peak (*W1*) to the second peak (*W2*) as well as the width ratio of the fourth peak (*W4*) to the third peak (*W3*). In our algorithms, the ratio of pulse width *W2* to *W1* is between 2 and 0.5, which means the values 2 and 0.5 correspond to two opposite ends of the mask or the edges of the microfluidic channel; on the other hand, when the *W2*/*W1* ratio is equal to 1, the trajectory of particles is the central of the channel along the channel width.The velocity of each particle is obtained by dividing the pattern length, 450μm, with the overall duration of the signal.

To reduce the complexity of device fabrication and operation without losing the purpose of proving the key concepts of optical space-time coding, the sheath flow for flow confinement was optionally turned off. As a result, coincident events, meaning more than two particles simultaneously pass the interrogation area, occurred to our device more frequently than typical microfluidic devices with sheath flow. Those signals produced by coincident events were identified since they lacked the 4 distinctive peaks which are characteristics of signals from single events. Those coincident events were then excluded from the analysis.

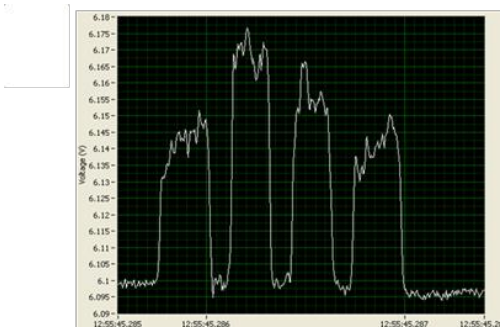

Figure 3.4 The snapspot of real-time encoded forward scattering signals from cells in time domain collected by a silicon PIN photoreceiver.

3. 3. Setup of optics and the preparation of particle samples

A 488 nm wavelength diode laser (40mW, Spectra-physics) was used as the optical source for the forward scattering measurement. The beam spot of the laser has a Gaussian intensity profile across the whole sensing area of 450 μm. Two silicon photoreceivers (PDA36A, Thorlabs) were placed over the microfluidic device to collect 5~10 degree forward scattering and side scattering signals from particles through the sensing area, respectively. Two different experiments were conducted. With the sheath flow, a mixture of polystyrene beads including 3.3 and 7.7 μm was introduced into the microfluidic channel. The flow rate ratio of sheath flow to sample flow was varied to test the experiment conditions. On the other hand, without the sheath flow, a mixture of polystyrene beads with diameters of 5, 10 and 15 μm (PPS-6K, Sphero) was injected into the microchannel with the flow rate controlled by a syringe pump (NE-1000, New Era Pump Systems).

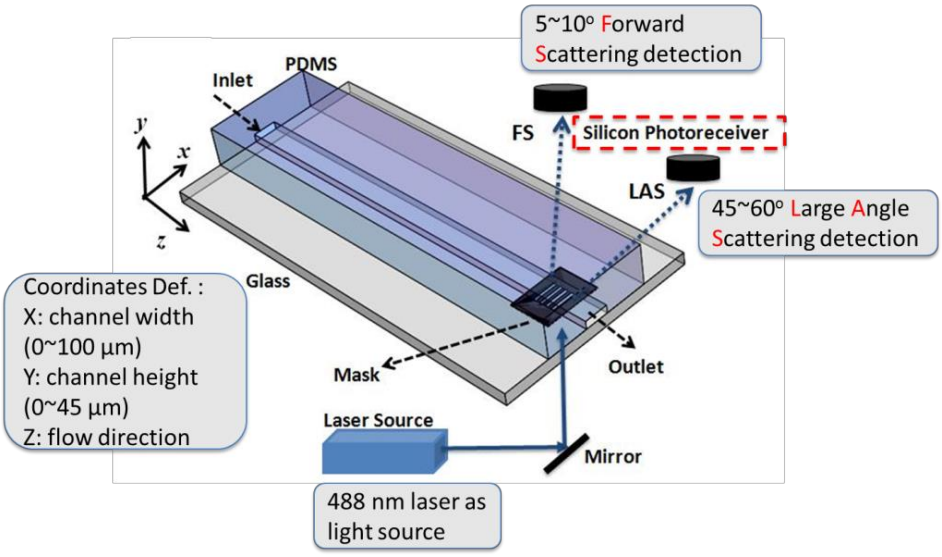

Figure 3.5 Schematics of test setup of the optical space-time coded microfluidic device. The samples enter the microfluidic channel from the inlet by a syringe pump. The laser beam illuminates the microfluidic channel through the spatial mask with a pattern in Fig 3.2.

3. 4. The optical-coding technique on the classification of particles

Figures 3.6 (a) and (b) are typical space-time coded FS and LAS signals produced by bead samples. The displayed signals have gone through a high pass digital filter (cutoff frequency: 2500 Hz) to remove low frequency noise and any baseline drift. A standard peak-finding algorithm based on a predefined threshold was employed in MATLAB to register all detectable events. In the experiment setting, the gain of amplifier is 50 dB for LAS detection and 30 dB for FS detection since the LAS signals are much weaker than FS signals. To show both signals on the same chart, the LAS signals were also plotted at 10× of the measured amplitudes. Due to the Gaussian intensity profile of the laser beam, the two central peaks of the space-time coded signals have higher magnitudes than the two side peaks. The quality of the signals, particularly the more noisy LAS signals, can be enhanced using several digital signal processing algorithms enabled by their special waveforms. Given the designed spacing and geometry of the spatial mask, the simultaneous occurrence of FS and LAS signals can be harnessed. Such algorithms include matched filter, cross correlation between the stronger FS signal and the weaker LAS signal, etc. We have shown that, for practical purposes, even the simplest algorithm of taking the average of the magnitudes of 4 distinct peaks in the waveform can significantly improve the CV values of both FS and LAS signals. For the following section, we have adopted this simple algorithm for data analysis since this algorithm requires a minimum amount of computation and favors real time processing required by cell sorting.

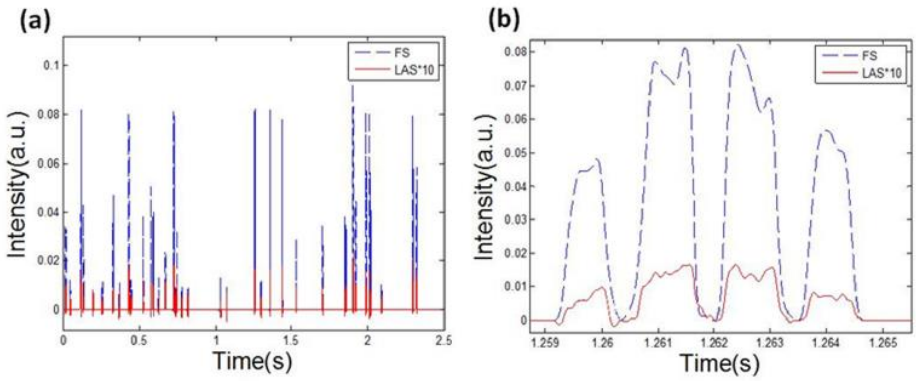

Figure 3.6 (a) Forward (blue) and large angle side scattering (red) signals for a mixture of 5, 10, and 15 lm beads. (b) The close-up view of one event. The dash line depicts the forward scattering signal and the solid line depicts the large angle scattering. (a) and (b) are signals after a low pass filter with a cutoff frequency of 2500 Hz.

To first demonstrate the optical-coding technique, we used the bead mixture including 3.3 and 7.7 μm polystyrene beads with introducing the sheath flow for flow confinement. The flow rate of sample flow is fixed at 6 μL/min with tuning the flow rate of sheath flow from 25 to 70 μL/min. Due to the trapezoidal slit, the widths of encoded FS signals could be used to find the bead position along the direction of channel width (*x*-axis) and its velocity. In Fig 3.7., the narrow variation of bead velocity (0.152±0.007 m/s, CV: 4.81%) indicates the flow confinement by sheath flows. It is also observed in the position distribution along *x*-axis direction, as shown in Fig 3.8. The distribution along *x*-axis direction of beads is averaged to be 47.457±4.431μm, i.e. CV:9.33%, indicating most beads are perfectly focused to the central of channel width. Figure 3.9 shows the scatter plot of the digitally processed FS and LAS signals for bead mixture under the sheath flow rate of 50μL/min. We also changed the sheath flow rate to examine the effect of bead confinement on the FS and LAS signals as summarized in Table 3.1. Due to the width of the microfluidic channel and the chosen flow rate, the beads were confined to a width of 19, 11 and 7.9 μm for the sheath flow of 25, 50 and 70μL/min, respectively. A narrower width beads are confined to, a better quality of FS and LAS signals, measured by CVs is expected. In our case, the FS CVs for 7.7 μm beads are 8.63%, 5.79% and 5.53% for sheath flow rate of 25, 50 and 70 μL/min, respectively. The FS CVs for 3.3μm beads are 11.88%, 10.81% and 10.13% respectively. We also observe similar improvements in LAS signals. The results manifest that a larger ratio between the sheath flow and the sample flow effectively improves the signal quality and reduces CVs.

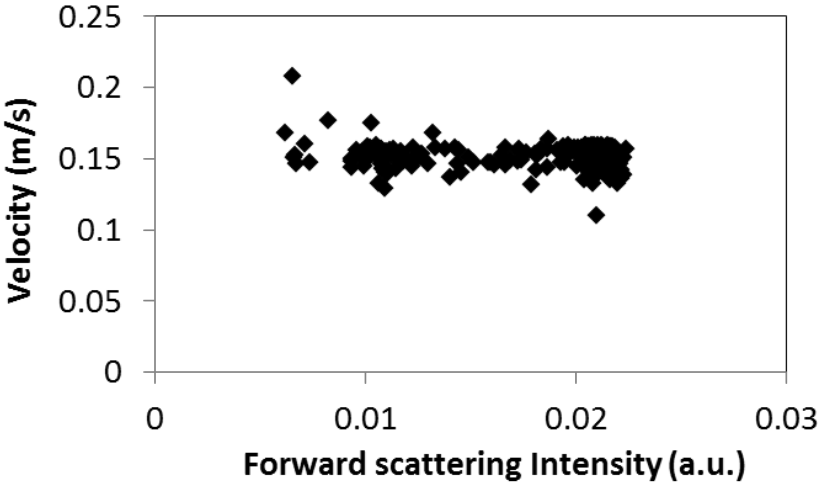

Figure. 3.7 The scatter plot of bead velocity over the entire sensing area to forward scattering intensity for the bead mixture, including 3.3 and 7.7 μm in diameter, at the sample flow rate of 6 μL/min with the sheath flow of 50 μL/min.

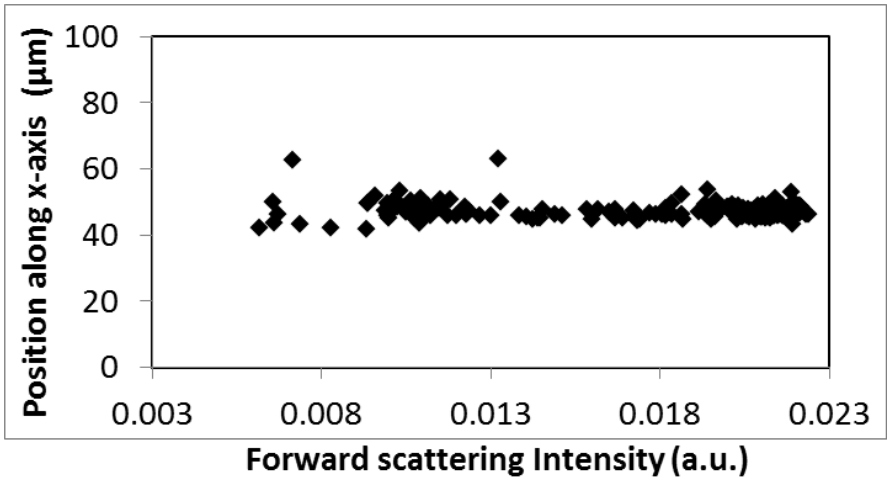

Figure. 3.8 The scatter plot of bead position along *x*-axis to forward scattering intensity for the bead mixture, including 3.3 and 7.7 μm in diameter, at the sample flow rate of 6μL/min with the sheath flow of 50 μL/min.

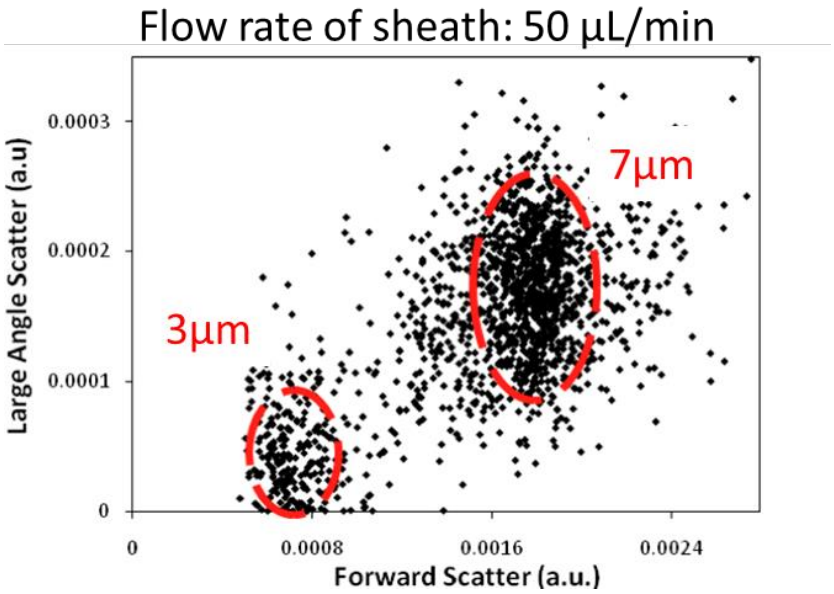

Figure. 3.9 The scatter plot of a mixture of 3.3µm and 7.7 µm polystyrene beads with a sheath flow rate of 50 µL/min and a sample flow rate of 6 µL/min. Red circles are the gates for visualizing two populations for 3.3µm (left) and 7.7µm (right) beads.

Table 3.1 The CVs for FS and LAS signals of 3.3µm and 7.7µm beads

	7.7 µm			3.3 µm		
Sheath Flow Rate (µL/min)	25	50	70	25	50	70
CV for Forward Scatter	8.63%	5.79%	5.53%	11.88%	10.81%	10.13%
CV for Large Angle Scatter	18.29%	16.96%	21.06%	56.82%	54.98%	49.70%

We also applied this method to detect cell samples. Lymphocytes were introduced at a flow rate of 10μL/min with a sheath flow of 40μL/min. The preliminary FS and LAS signals from lymphocytes are shown in Fig 3.10. Lymphocytes are typically around 8μm in diameter. After signal processing, we found the cells were confined to regions around the center of the channel with a spread of 20.4 μm , as shown in Fig. 3.10 (a). Fig 3.10 (b) shows the scatter plot of FS and LAS signals with CVs of 24.51% and 30.45% for FS and LAS respectively. The large CVs are the results of inherent non-uniformity of cells.

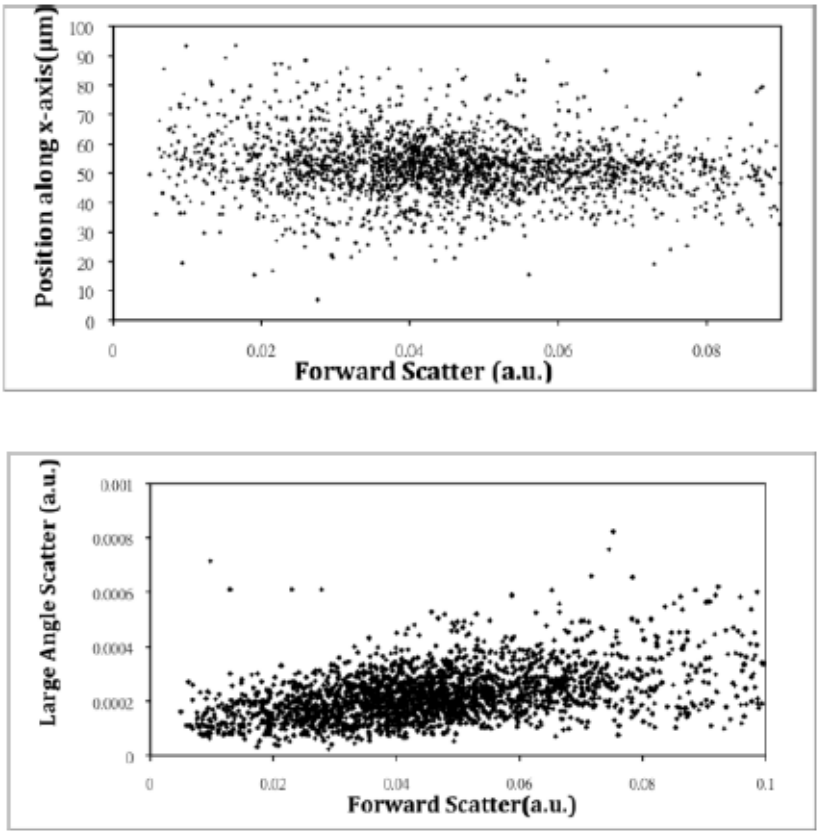

Figure 3. 10 (a) The scatter plot of position versus FS signals, (b) The scatter plot of FS and LAS signals for lymphocytes. The flow rates of lymphocyte samples and sheath flow are 10 and 40 μL/min, respectively.

Even though the sheath flow can provide a good flow confinement, the thoughput of sample analysis will be sacrificed significantly. In the following, we examine the samples at very high flow rate without the aid of sheath flow. Fig. 3.11 (a) shows the distribution plot of LAS intensity versus FS intensity from a sample consisting of a mixture of 5, 10 and 15 μm polystyrene beads. The scatter plot from a commercial flow cytometer (C6 flow cytometer, Acurri) is shown in Fig. 3.11 (b) for comparison. It is clear that larger beads produce higher FS and LAS (or side scattering for the commercial system) intensities and three types of beads form three separate clusters that are easy to distinguish. For data from the commercial flow cytometer, there are also signals very close to the origin likely due to debris or impurities in the sample and system noise. Such data are not shown in our result because the signal processing has removed those points. To further demonstrate the performance improvements using the proposed method, we ran the experiment using the same setup without the spatial mask and the result is shown in Fig. 3.11 (c). In sharp contrast to Fig. 3.11 (a), without the spatial mask one cannot obtain 3 distinct groups in the distribution plot corresponding to 5, 10, and 15 μm beads. By employing the quadrant gate, CVs of each bead population from our device (with the spatial mask) and the commercial flow cytometer are summarized in Table 3.2. The FS CVs measured from our device are 10.05%, 9.53%, and 3.95% for 5, 10, and 15 μm beads, respectively. These values are about 3 times of the CVs from the commercial system. We suspect that the laser speckle noise and the interference effects caused by the spatial mask may contribute to the signal fluctuation of the FS signal shown in Fig. 3.6 (b). Nonetheless, these are among

the best values achieved with microfluidic devices.[12] On the other hand, the CVs of large angle signals from our device are compared favorably with the CVs of side-scattering signals from the commercial device, and the improvements are quite significant for 10 and 15 μm beads. One should keep in mind that the LAS signal was detected by a low cost Si photoreceiver bias at 5 V as opposed to a PMT biased at 1500 V and the CV values of the LAS signals set the new record for microfluidic devices. Hence, we believe the optical space-time coding method is not only compatible with the microfluidic platform but also particularly suitable for point-of-care applications where low cost, simple operation and quality of results are key concerns.

Besides reducing the noise and CV values for FS and LAS signals, the optical space-time coding method also offers the unique capabilities to measure the position and velocity of each particle in the microfluidic channel. The velocity information can be easily obtained from the spacing between the slits and the time difference between the peaks in the waveform. As we have 4 peaks produced by 4 slits in the spatial mask, the speed of travel can be obtained from multiple measurements to reduce errors. Based on the special design of the spatial mask (Fig. 3.2), there exists a simple relation between the ratio of the pulse width of each peak and the position of the particle.

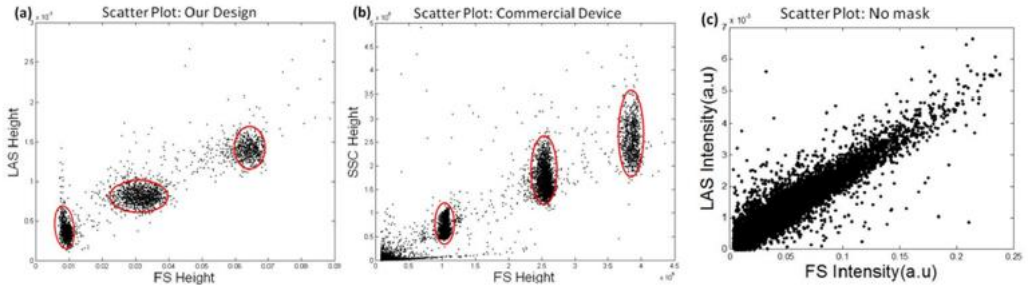

Figure 3.11 Data plots for a mixture sample of 5 lm, 10 lm, and 15 lm beads. (a) FS-LAS scatter plot of our design (with the spatial mask). (b) FS-SSC scatter plot of a commercial flow cytometer. (c) FS-LAS scatter plot of a microfluidic devicewithout the spatial mask. The flow rate is 25 µl/min.

Table 3.2 Summary of scatter CVs of polystyrene bead mixture consisting of 5, 10 and 15 µm, measured with the optical-coding microfluidic device and the commercial flow cytometer (Accuri C6), respectively.

	FS CV (our design)	FS CV (commercial device)	LAS CV (our design)	SSC CV (commercial device)
5 μm	10.05%	3.38%	26.12%	22.33%
10 μm	9.53%	2.78%	11.5%	16.85%
15 μm	3.95%	1.97%	7.97%	14.09%

Fig. 3.12 shows two distribution plots: bead position versus FS intensity (Fig. 3.12 (a) and (c)) and velocity versus FS intensity (Fig. 3.12 (b) and (d)), for the mixture of 5, 10 , and 15 μm beads at a flow rate of 25 and 50 μl/min, respectively. Around 3000 events were processed and included in the figure. The data in Fig. 3.12 (a) suggest that, without flow focusing or sheath flow, 5 μm beads spread widely over the entire 100 μm width of the microfluidic channel whereas 10 μm and 15 μm beads were more concentrated to a narrow range of the channel. This is a clear demonstration of the effect of inertial focusing governed by the "particle Reynolds number."[13] The principal of inertial migration was first proposed in 1961[14] in the macroscale tube, where particles uniformly distributed in suspension migrate to the equilibrium position away from the channel walls. Recently, researchers have observed the inertial effect in microfluidic devices. The concept of inertial migration of particles within microfluidic channels is the interaction of drag forces and lift forces. Due to the viscosity of fluid, the nature parabolic velocity profile of carrier fluid causes the drag forces that drive the particles toward the channel walls. As particles close to the channel walls, a wall-induced lift force will be generated to drive particles away from walls.[10] These two opposing forces are dependent on the ratio of particle diameter to channel dimension (a_p/D_h), where a_p is the diameter of particles and D is the hydraulic dimension of microchannel geometry. The minimal ratio of particle diameter to channel dimension ($a_p/D_h \geq 0.07$) is required to trigger the inertial effect within the microchannel. The equilibrium position of particles in a rectangular cross-section microchannel is the longer side, as shown in Fig 3.13. Besides the geometry ratio, the high flow speed is another factor to meet the

requirement of inertial effect within a microchannel. Because of the intrinsic small dimension of microfluidic device, the inertial effect is not considered in the early stage of developing microfluidic devices. However, for all microfluidic devices taking the advantage of inertial effect, it has to operate in certain Reynolds number (Re) regime ($Re \leq 100$), where Reynolds number is defined as $Re=\rho U_f D_h/\mu$ (ρ: fluid density, U_f: average velocity of flow, D_h: hydraulic diameter of microchannels, and μ: fluid viscosity). For our device, the microchannel cross-section is rectangular with D_h of 62.1 μm and the measured average velocities are 0.09 and 0.18 m/s for the flow rates of 25 and 50 μL/min, resulting in Re of 5.59 and 11.18, respectively, which are under the stable regime to observe the inertial focusing effect with the given channel geometry.

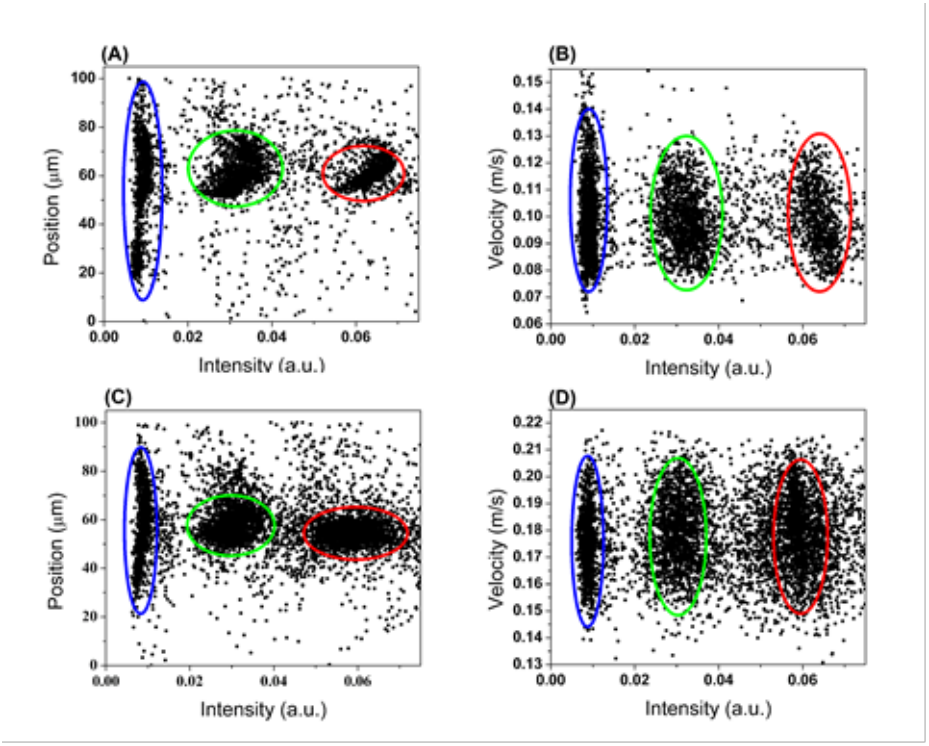

Figure 3.12 Scatter plots of particle position along x-axis versus forward scattering intensity, (a) and (c), and particle velocity versus intensity, (b) and (d), at flow rates of 25 μL/min and 50 μL/min, respectively. Red circle: 15 μm beads, Green circle: 10 μm beads, Blue circle: 5 μm beads.[11]

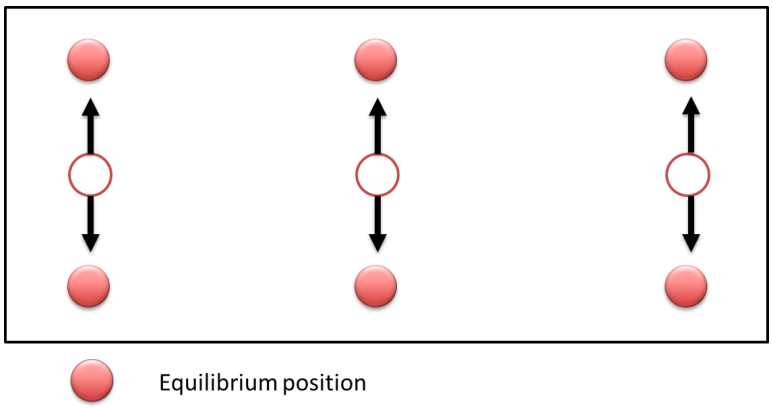

Figure 3.13. Inertial migration of particles in a rectangular microchannel for $a_p/D_h \geq 0.07$. The solid circles represent the final particle equilibration positions under the inertial effect.

Next we describe the method to obtain the particle position along channel depth (i.e. *y*-axis) from the particle velocity. As a result, at a given particle position along the width (*x*-direction) of the channel, the velocity profile along the out-of-plane (*y*-axis) direction obeys, to a good approximation, the parabolic characteristics:

$$\upsilon(x, y) = \upsilon_{Max}(x) [1- (y/h)^2] \quad (3.1)$$

where $\upsilon(x, y)$ is the velocity at a specific position (x,y) over the cross-section of the microchannel, $\upsilon_{Max}(x)$ is the velocity at position x and the middle of the channel (i.e., at y=0), and h is the half-depth of the channel, 22.5 μm in our microfluidic device. Therefore, as long as we obtain $\upsilon_{Max}(x)$ at each position x from straightforward fluid dynamic simulation, we can obtain the position y of the particle from its velocity using Eq. (3.1). Because the measured average velocities agree well with the values calculated from COMSOL simulations (Fig. 3.14) that yield the average velocities of 0.09 and 0.19 m/s, this justifies the use of the simulated $\upsilon_{Max}(x)$ to find the out-of-plane position of the particle, y, from Eq. (3.1).

Fig 3.15 illustrates the contour plot of spatial distribution for 5 and 10 μm beads at flow rates of 25 and 50 μL/min, respectively. First of all, the results show that the stable positions for both 5 μm and 10 μm beads are 8.3 μm away from the channel wall (i.e. ±14 μm from center) under a flow rate of 25 μL/min and ~6.8 μm away from the channel wall (i.e. ~±16 μm from center) under a flow rate of 50 μL/min. These results indicate that particles migrate closer to the wall as *Re* increases;[10] and under these experimental parameters, the lift force drives particles to positions that are ~0.2 *H* away from the walls where *H* is the characteristic dimension (i.e. height of the microchannel

for our device geometry).[15] Secondly, along the *x*-axis, larger particles are more concentrated toward the center of the channel.

Such distinct phenomena in particle distributions along the *x*- (width) and *y*-axes (height) are consistent with the results predicted by the fluidic dynamic theory for inertial focusing. The lift force can be represented as $F_L=\rho G^2 C_L d^4$ where G is the fluid shear rate ($G = 2\ U_f/H$), C_L is the lift coefficient (which for microchannels remains constant), and d is the particle diameter.[10] In our device geometry, the width to height ratio is larger than 2, resulting in a lift force in the *y*-direction four times greater than the force in the *x*-direction due to different shear rates. This effect causes particles to migrate toward the longer channel walls to find the equilibrium positions.[13] Concerning the lift force in the *x*-direction, its magnitude depends on the size of particles to the 4th power so the lift force of 10 μm beads is 16 times of the lift force of 5 μm beads. The greater lift force leads larger beads to be farther away from the walls of shorter dimension and show a narrower distribution than the smaller beads, consistent with the results in Fig. 3.15.

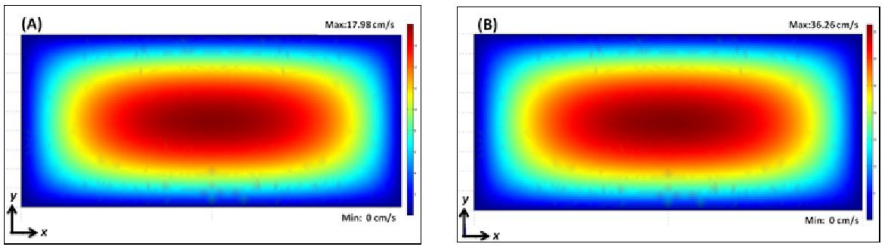

Figure 3.14 Simulated flow velocity profile on the *x*-*y* plane at a flow rate of (a) 25 µL/min and (b) 50 µL/min.

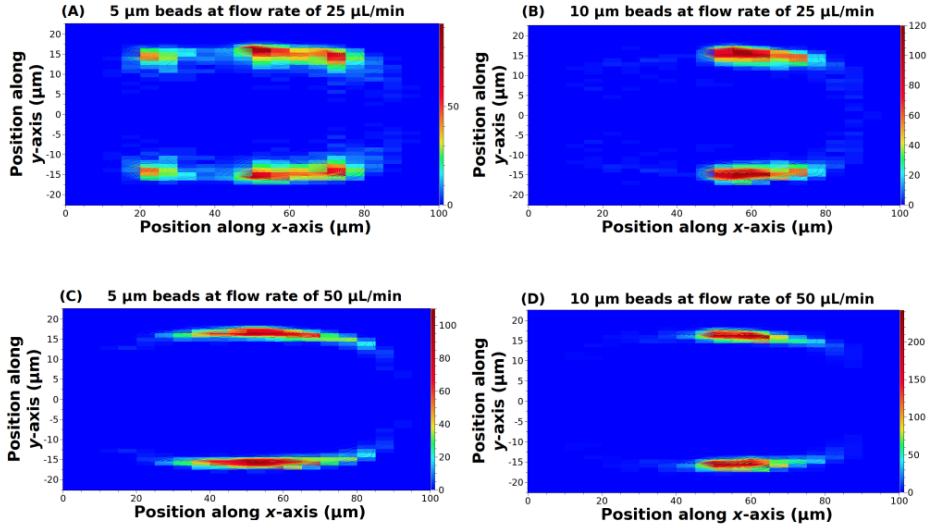

Figure 3.15 Spatial distribution of particles within microfluidic channels. (a) and (b) are results for 5 and 10 µm beads at a flow rate of 25 µL/min. (c) and (d) are results for 5 and 10 µm beads at a flow rate of 50 µL/min. The color bar shows the frequency of microbeads population.

To show the feasibility of our technique for cell detection, we performed preliminary experiment with fibroblast cells at a flow rate of 30 μL/min. About 1000 events were detected and processed, and the results are shown in Fig. 3.16. Fibroblasts have a typical size of around 15 μm, and the cell focusing effect is clearly demonstrated in Fig. 3.16 (b). Due to the depth and angle of tubing insertion to microfluidic devices, the particle distribution along the x-axis direction might show bias from the center of the channel; and our method can faithfully reveal such effects of interfacing the macro- and micro- fluidic environments. So far all the experiments have been performed at sample speeds between 5 cm/s and 20 cm/s, which are typical values for many applications (e.g. flow cytometer, cell counter, complete blood count, etc.). This method can be applied to higher sample speeds for high throughput applications because the Si photoreceiver has a large (>10 MHz) gain-bandwidth product. For special applications that require lower sample speeds, one would expect improved CVs than the reported values here provided the sample is properly diluted to reduce the probability of coincident events. Similar to conventional forward scattering measurements, our technique is subject to the laser intensity noise, amplifier thermal noise, and possibly speckle noise. Such noises may contribute to the increase in the CV values as well as the uncertainties in the sample position measurements.

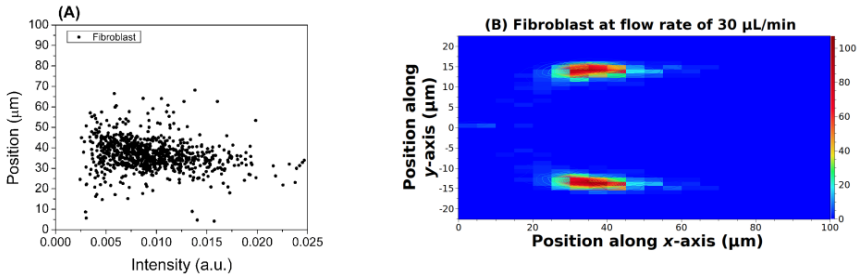

Figure 3.16 (a) Scatter plot of fibroblast position along x-axis versus forward scattering intensity and (b) Spatial distribution of fibroblast within the microfluidic channel at a flow rate of 30 μL/min.

3. 6. Conclusion

To summarize, we have demonstrated an optical space-time coding method that can be easily incorporated into microfluidic devices to aid the detection of forward and large angle scattering signals. Because of the enhanced signal quality by the new technique, one can detect large angle scattering signals using a pair of silicon PIN photoreceivers without the usual PMT detector, resulting in significant cost saving and simplification in operation to favor point-of-care applications. The optical space-time coding technique also enables us to set the performance records for large-angle scattering CVs among microfluidic devices. The performance of the technique has also been verified with commercial systems.

Meanwhile, we have also demonstrated, for the first time, an optical-coding technique to experimentally obtain the particle distributions in a microfluidic channel under different flow conditions. After processing the forward scattering signals encoded by a specially designed spatial mask, we obtain the position and velocity of each bead. The results provide insight of the behaviors of different particles in microfluidic channels. We also demonstrate the feasibility of the technique to mammalian cells and produce the spatial distribution of cells within the microfluidic channel. The technique can help us evaluate and design microfluidic lab-on-a-chip devices such as cell sorters and flow cytometers. The methodology will find wide applications in microfluidic biomedical devices. The enumeration of blood cells and multi-dimensional analysis of harnessing the optical-coding technique will be discussed in Chapter 4 and Chapter 5, respectively.

References:

1. S. H. Cho, J. M. Godin, C. H. Chen, W. Qiao, H. Lee and Y. H. Lo, Biomicrofluidics **4** (4) (2010).

2. P. Yager, T. Edwards, E. Fu, K. Helton, K. Nelson, M. R. Tam and B. H. Weigl, Nature **442** (7101), 412-418 (2006).

3. S. Neethirajan, I. Kobayashi, M. Nakajima, D. Wu, S. Nandagopal and F. Lin, Lab Chip **11** (9), 1574-1586 (2011).

4. J. Godin, C. H. Chen, S. H. Cho, W. Qiao, F. Tsai and Y. H. Lo, J Biophotonics **1** (5), 355-376 (2008).

5. A. Valero, T. Braschler, N. Demierre and P. Renaud, Biomicrofluidics **4** (2) (2010).

6. X. C. Xuan, J. J. Zhu and C. Church, Microfluid Nanofluid **9** (1), 1-16 (2010).

7. N. Watkins, B. M. Venkatesan, M. Toner, W. Rodriguez and R. Bashir, Lab Chip **9** (22), 3177-3184 (2009).

8. E. B. Cummings and A. K. Singh, Anal Chem **75** (18), 4724-4731 (2003).

9. J. J. Hawkes, R. W. Barber, D. R. Emerson and W. T. Coakley, Lab Chip **4** (5), 446-452 (2004).

10. D. Di Carlo, D. Irimia, R. G. Tompkins and M. Toner, P Natl Acad Sci USA **104** (48), 18892-18897 (2007).

11. T. F. Wu, Z. Mei, L. Pion-Tonachini, C. Zhao, W. Qiao, A. Arianpour and Y. H. Lo, Aip Adv **1** (2) (2011).

12. J. Godin and Y. H. Lo, Biomed Opt Express **1** (5), 1472-1479 (2010).

13. A. A. S. Bhagat, S. S. Kuntaegowdanahalli and I. Papautsky, Microfluid Nanofluid **7** (2), 217-226 (2009).

14. G. Segre and A. Silberberg, Nature **189** (476), 209-& (1961).

15. B. Chun and A. J. C. Ladd, Phys Fluids **18** (3) (2006).

Chapter 3 or portion thereof has been published in *AIP advances* (2011), Tsung-Feng Wu, Zhe Mei, Luca Pion-Tonachini, Wen Qiao, Ashkan Arianpour and Yu-Hwa Lo, and *Biomicrofluidics* (2011), Zhe Mei, Tsung-Feng Wu, Luca Pion-Tonachini, Wen Qiao, Ashkan Arianpour and Yu-Hwa Lo.

Chapter 4

Optofluidic device for label-free cell classification from human whole blood

In this chapter, we demonstrated a clinlical application of using unique optofluidic lab-on-a-chip device that can measure optically encoded forward scattering signals to address point-of-care needs. From the design of the spatial pattern, we can measure the position and velocity of each cell in the flow and generate a 2-D cell

distribution plot over the cross section of the channel. Moreover we have demonstrated that the cell distribution is highly sensitive to its size and stiffness. The latter is an important biomarker for cell classification and our method offers a simple and unequivocal method to classify cells by their size and stiffness. We have proved the concept using live and fixed HeLa cells. Due to the stiffness and size difference of neutrophils compared to other types of white blood cells, we have demonstrated detection of neutrophils from other blood cells. Finally, we have performed the test using 5 μL of human blood. In a greatly simplified blood preparation process, skipping the usual steps of anticoagulation, centrifuge, anti-body labelling or staining, filtering, etc., we have demonstrated that our device and detection principle can count neutrophils in whole human blood. Our system is compact, inexpensive, and simple to fabricate and operate, having a commodity laser diode and a Si PIN photoreceiver as the main pieces of hardware. Although the results are still preliminary, the studies indicate that this optofluidic device holds promise to be a point-of-care and home care device to measure neutrophil concentration, which is the key indicator of the immune functions for cancer patients undergoing chemotherapy.

4. 1. Introduction

Detection and classification of cells using sophisticated tools such as flow cytometers and fluorescence-activated-cell-sorters (FACS) are often performed clinically for disease diagnosis and prognosis. To reduce cost, time from test to outcome, as well as chances for hospital infection, performing such tests in point-of-care

clinics or patient's residence is highly attractive provided the devices are able to generate reliable results, easy to operate, compact and affordable.[1]

Today most sophisticated equipment for cell-based assays is located in major medical centers. The high cost for equipment acquisition, maintenance, and medical personnel, as well as the support of the massive outfit and infrastructure contributes to the high and rising health care cost in most developed countries, particularly the United States. The lack of such sophisticated medical equipment in resource limited countries and territories, on the other hand, presents major challenges in delivering quality health care services to populations living in these areas. To address this barrier in health care, development of a new class of medical devices that are suitable for point-of-care or personal use has become a global focus of biomedical device research

To meet this challenge, lab-on-a-chip devices that combine microfluidics with other technologies have attracted significant attention. Since blood and bodily fluids are the samples easiest to acquire with minimal invasiveness and such samples, particularly blood, contain rich health and disease information, a large family of lab-on-a-chip devices are microfluidic devices that handle blood and bodily fluids. However, most existing methods require labelling to detect or isolate specific subpopulations of cells from the sample mixture,[2, 3] and require sample preparation procedures such as anticoagulation, anti-body labelling, staining, centrifuge, filtering, etc. that are too complicated to be handled by people without medical trainings. To address this issue, we suggest that, instead of developing general purpose systems such as full-bloomed flow cytometers, our chance of success in moving the lab-on-a-chip technology to

clinics will be significantly better if we develop devices for specific applications, targeting at specific biomarkers without labelling. To meet this objective, three issues need to be addressed: (1) identify an effective biomarker or markers for unequivocal determination of the condition of certain disease, (2) develop an accurate and low-cost method to read the biomarker signals, and (3) develop straightforward and minimally invasive sample extraction and processing procedures. In this paper, in addition to cell size that has been used to classify cells since the invention of Coulter counter, we use cell stiffness as an additional biomarker because the stiffness of cells is cell type specific[4] and also give information about the health and life cycle of cells.[5] To detect the cell effects in microfluidics attributed to cell stiffness, we invent a unique method of optical space-time coding, described in Chpater 3, that enables us to unambiguously measure the position of each cell travelling in the microfluidic channel. Using the principle that the stable positions of cells in a microfluidic channel depend upon cell size and stiffness, we can classify cells by their stiffness in the flow channel at very high throughput. Since the detection method needs only a semiconductor diode laser and a Si PIN photoreceiver requires no sheath flow for flow confinement, the system is simple and compact and can be fabricated at very low cost. Finally, the test draws only a minimum amount of peripheral blood (~5μL) similar to the blood draw for glucose test, and requires minimum sample processing.

To demonstrate point-of-care and home care functions, we have applied the device to measure the neutrophil concentration in the blood because neutrophil concentration is an important indicator for the functions of the immune system.[6] For a

healthy person, the total concentration of white blood cells is between 4000 and 11000 per microlitre of blood, with 53-62% of white blood cells being neutrophils and the majority of the rest being lymphocytes. Neutrophil is a granulocyte named by the shape of its nucleus and is softer than monocytes and lymphocytes,[7] a property that facilitates its migration to the sites of infection from blood vessels. Clinically a patient is considered to be in mild neutropenia if the neutrophil count is between 1000 and 1500/μL, in moderate neutropenia when the neutrophil density drops to 500 – 1000/μL, and in severe neutropenia when the neutrophil density falls below 500/μL. Severe neutropenia leads to very high risks of infection, which could be life threatening particularly for cancer patients undergoing chemotherapy.[7] Each year over 90,000 patient deaths result from hospital infection in the United States.[8] Cancer patients undergoing chemotherapy typically make 12 to 24 hospital visits, often times only for neutrophil counts. This represents a particularly high risk group and therefore a device that can easily and accurately measure the immune function of cancer patients is tremendously valuable. Therefore we have chosen such a device for demonstration of clinical applications of lab-on-a-chip technologies

We have designed and fabricated a simple optofluidic lab-on-a-chip device consisting of a straight microfluidic channel with spatially coded patterns that modulate the excitation light intensity experienced by the particle passing the patterns. The technique effectively converts a spatial pattern (code) into an optical intensity-modulated time-domain signal that can be readily processed by digital signal processing (DSP) algorithms.

The method of converting a spatial pattern into a temporal signal has been explored by a few groups.[9, 10] However, the previous methods detect only fluorescent signals for labelled cells, and cell labelling is a dedicated and expensive process that cannot be done correctly and reliably by persons without medical training and access to proper facility. Above all, these earlier methods are elegant ways to detect the same information as a conventional flow cytometer does, thus producing no new information about cell properties. In Chapter 3, we have discussed a specially designed optical space-time coding method that can detect new information, namely the position of the cell in the channel and its travel speed, not detectable by the previous methods. With the designed pattern, the waveform of the optical forward scattering (FS) signal directly corresponds to the cell position inside the microfluidic channel. After applying the DSP technique to decipher the FS waveform, we can measure the cell position very precisely. The equilibrium position of cells inside a microfluidic channel is highly useful because it directly results from cell size and stiffness.[11-13] Thus one can use cell position to distinguish softer and larger neutrophils from red blood cells and other types of white blood cells.

Furthermore, since the space-time coded signal is carried in both forward and side scattering signals, we have the option to only detect the forward scattering (FS) signal from which all the needed information such as cell position and velocity can be obtained. This makes the system simple, robust, compact and inexpensive since forward scattering signal is orders of magnitude stronger than side scattering signal thus requires no sophisticated optics or photomultiplier tubes (PMTs) to perform the measurements.

4. 2. Principal of device operation

In chapter 3, we have elucidated the basic concept of using the optical-coding microfluidic device. To encode the position and velocity information into the FS signal from a travelling cell, we designed a mask pattern that contains four trapezoidal slits, as shown in Fig. 4.1. A semiconductor laser source was used to illuminate from the bottom of the microchannel. Through these slit openings, the forward scattering signal was detected by the Si photodiode on the opposite side of the semiconductor laser diode. 5μL of whole blood is taken by a finger prick and then introduced into the microfluidic channel after lysing red blood cells. Depending on the trajectory of moving samples, the forward scattering signals were encoded by the spatial mask and exhibited distinct waveforms in time domain (Fig. 4.2). We later on used these waveforms to obtain the positions of these cells in the microfluidic channel. For convenience of discussion, we define the direction of channel width as *x*-axis and the direction of channel height as *y*-axis. The intensity-modulated FS signal by the trapezoidal slits displays 4 peaks (Fig. 4.2). The ratio between the width of the first peak (*W1*) and the second peak (*W2*) yields information about the cell position in the *x*-axis. The same information can also be obtained from the ratio of *W4* and *W3*. The redundancy helps reduce noise and improve measurement accuracy. As discussed in Chapter 3, the velocity of traveling cells can be resolved by dividing the total pattern length (450 μm) by the duration of signal. Then the spatial distribution of cells within a microfluidic channel can be reconstructed.

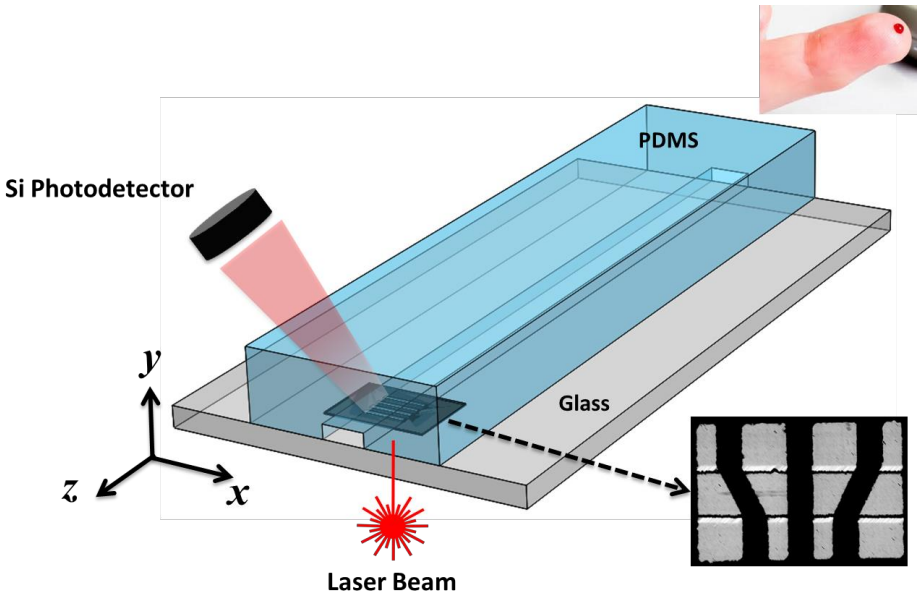

Figure 4.1 Schematics of the encoded microfluidic device and the system setup for white blood cell counting. 5μL of human whole blood taken by finger prick is diluted with the blood lysis agent. At high flow rate to indroduce the lysed white blood cells, the neutrophils can be counted by post digital signal processing.

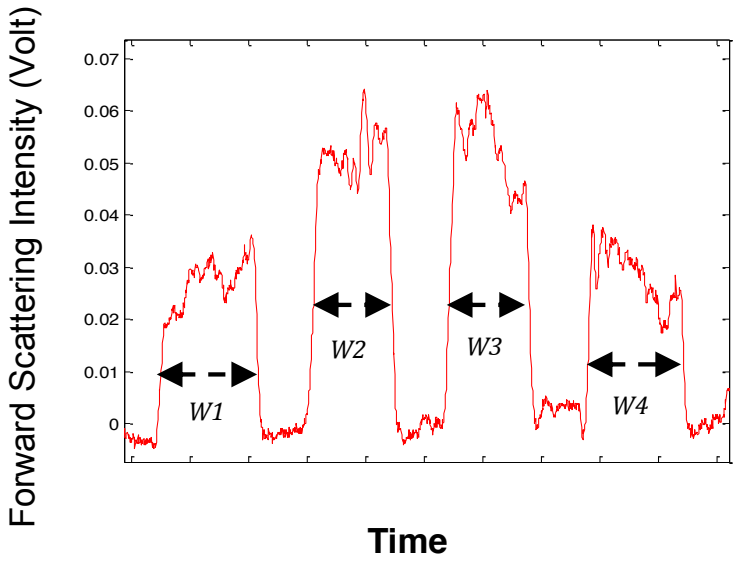

Figure 4.2 An encoded forward scattering signal of white blood cell detected by the silicon PIN photoreceiver after digital signal processing.

The knowledge of both the position and speed of each cell gives us insight about the property of cells. In our device, the inertial effect would focus the particles toward equilibrium positions inside the channel. In addition, if similar sized cells have different stiffness, the more deformable cells tend to migrate laterally toward the central area in the *x*-axis as illustrated in Fig 4.3. When cells flow within the microchannel, the relative concentration of cells along the radial direction of channel is different. The radial changes of cell composition along the microchannel mainly depend on the hydrodynamic properties of cells. In other words, the cells that are more deformable will tend to move faster than other stiffer cells. Due to the no-slip boundary condition on channel walls, the parabolic velocity profile is given within the microchannel. Thus, the region of higher speed is the centre of microchannel, where faster and more deformable cells would stay. Fig 4.4 provides a schematic illustration of the equilibrium positions in the microchannel for larger and softer cells relative to smaller and stiffer cells. To summarize, the equilibrium positions of cells are determined by the balance of two forces, lift force due to the inertial effect and fluidic dynamic drag force. Larger cells experience a greater inertial force which pushes the cells farther away from the channel wall so they tend to be located nearer the centre of the microchannel than smaller cells do (Fig. 4.4 (a)). On the other hand, due to the greater deformability of softer cells for better alignment with the streamline, softer cells experience less drag force than stiffer cells and tend to be closer to the center of the channel. As a result, larger and greater deformability cells can be identified by their travel speed and their location in the microchannel.

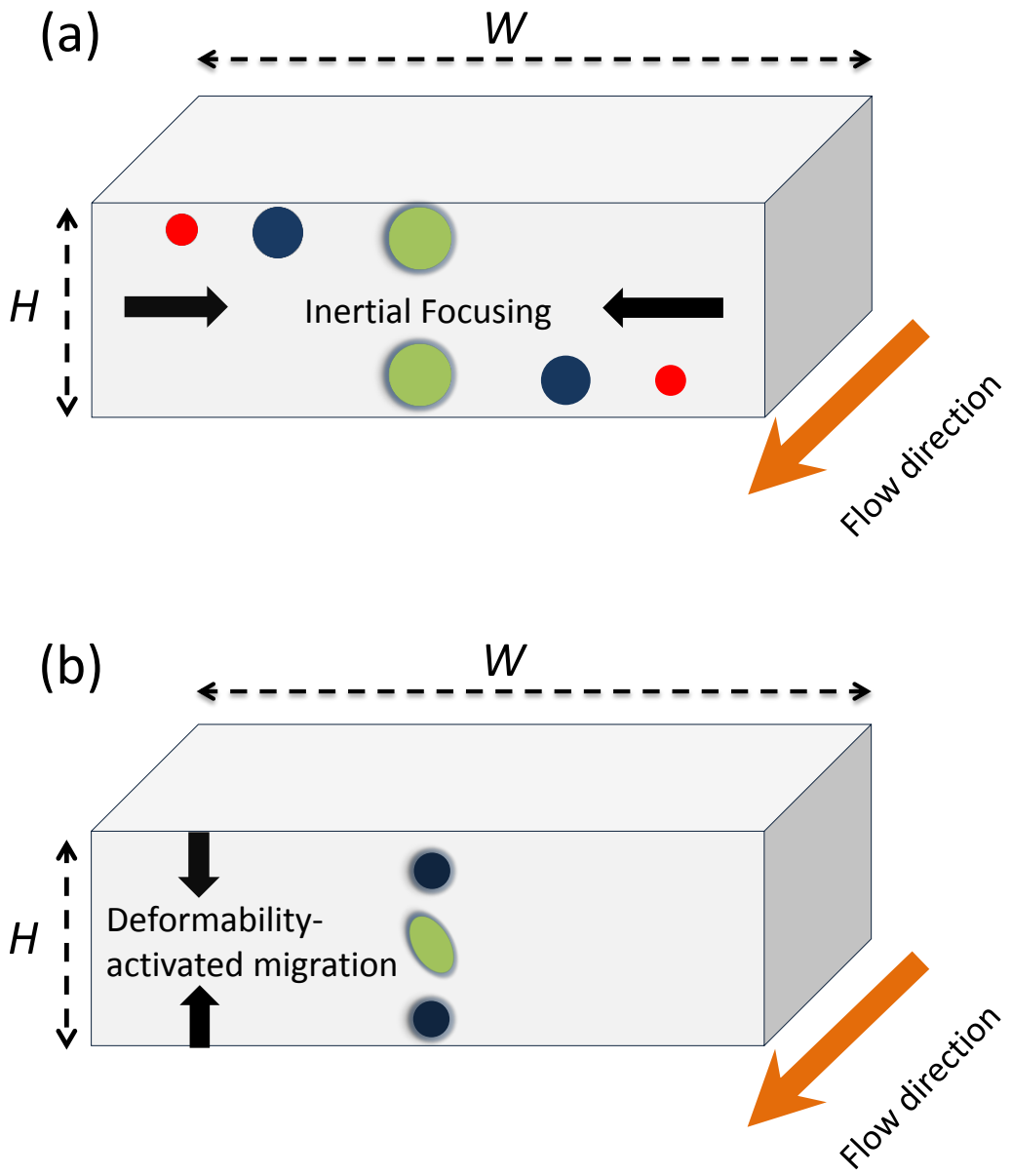

Figure 4.3 Illustration of equilibrium position distribution of cells affected by (a) the inertial effect, which mostly depends on the size of cells, and (b) the deformability-activated migration, which is related to the stiffness of cells.

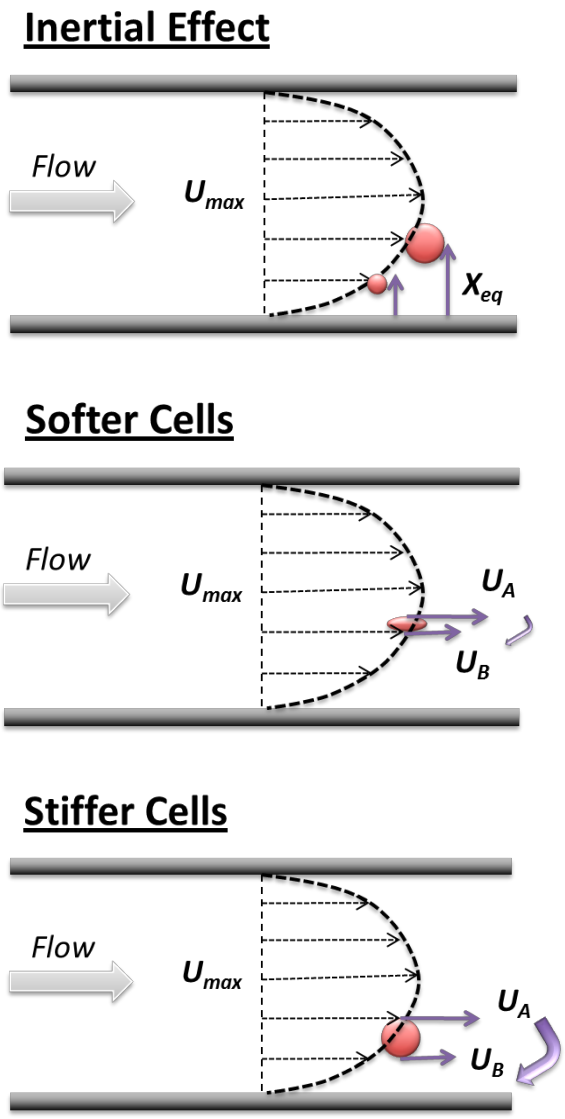

Figure 4.4 (a) Equilibrium position of cells affected by the inertial effect, which mainly depends on the size of cells. The larger cells experience the greater lift force that pushes cells toward the centre of the mcirochannel. (b) and (c) When the cells are deformable under the shear force, the velocity across cells (U_A-U_B) causes the gradient difference that keeps the softer cells stay around the centre of the microchannel and have faster traveling speed.

4. 3. Preparation of samples

For device characterization with selected cell types, we have prepared samples with cancer cells (HeLa cells), red blood cells (RBCs), and white blood cells (WBCs). HeLa (human cervical epithelioid carcinoma) cells were cultured in the growth medium in a humidified incubator at 37°C in 5% CO_2. For fixed HeLa cells, paraformaldehyde was used prior to the experiment. Whole blood samples used to produce RBC and WBC samples were purchased from the blood bank. To prepare white blood cell samples, whole blood was lysed with commercial lysing buffer (eBioscience, CA). To prepare RBC samples, 100μL of whole blood was centrifuged at 10,000 rpm. 5μL of red blood cells was carefully taken out from the bottom of canonical tubes (below the buffy coat) and then diluted 2 million times using a buffer solution. The buffer solution used for sample dilution consists of 10mM ethylenediaminetetraacetic acid (EDTA), 1% bovine serum albumin (BSA), and 1X phosphate buffered saline (PBS)

For neutrophil counting tests, 5μL of whole blood was taken from healthy volunteers using a finger prick. The blood was first diluted with 1mL of buffer solution. Then 500μL RBC lysing agent was added to 150μL of the diluted blood to create a total dilution of ~870X in the WBC concentration. After keeping the sample in the ambient environment for 10 minutes, the blood mixed with the lysing agent was introduced into the microfluidic device for measurement without further preparation.

4. 4. Results and discussion

4. 4. 1. Cancer cell detection

Signals from HeLa cells were first characterized using the space-time optically encoded signal from the lab-on-a-chip optofluidic device. HeLa cells were tested at three different flow rates of 25 μL/min, 50 μL/min and 75 μL/min. Under the average flow velocities of 9, 18 and 27 cm/s for the corresponding flow rates of 25, 50, and 75 μL/min, the Reynold number (*Re*) is calculated to be 5.6, 11.2 and 16.8, respectively. More than 500 cells were detected within a measurement period of 90 seconds and the encoded FS signals were processed using custom developed algorithms implemented as the way we discussed in the previous chapter. With the aid of COMSOL simulation to retrieve the maximum velocity of flow at each flow rate, the spatial distribution of cells was obtained using the method discussed in the previous section. Figure 4.5 shows the distribution of HeLa cells over the cross section of the microfluidic channel at different flow rate, respectively. When the flow rate increases, HeLa cells migrate toward the center of the microchannel along the *x*-axis. Detailed analyses on the HeLa cell distribution along the *x*-axis show a standard deviation (σ_x) of 17.26 μm, 12.89 μm and 7.59 μm at the flow rates of 25, 50, and 75 μL/min, respectively. Similar phenomenon have been observed using a CCD camera and explained in the literature[14, 15] although those measurements were made from time averaged intensity profile of fluorescent beads instead of individual unlabeled cells.

A more prominent and useful feature for cell classification in Fig. 4.5 is that HeLa cells were tightly focused to narrow positions in the *y*-axis. At the flow rates of

25, 50, and 75 μL/min, the standard deviation (σ_y) of each band in the channel height direction is as small as 1.36 μm, 1.03 μm, and 0.51μm, respectively. Given the ~20 μm average size of HeLa cells, this represents an extremely tight distribution along the *y*-axis. In addition, the position of the peak population of HeLa cells moves closer to the channel wall with increasing flow rates. The very tight population distribution represents steep energy minima.

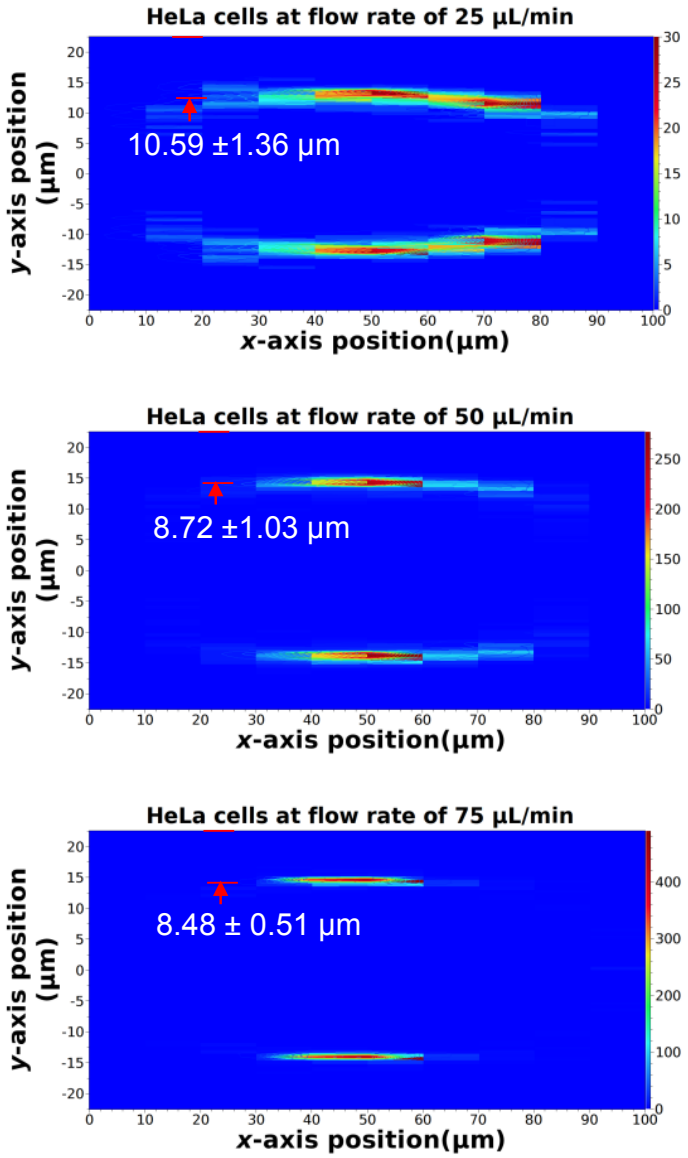

Figure 4.5 Population distribution plots for HeLa cells over the cross section (100µm × 45µm) of the microfluidic channel at flow rates of 25, 50, and 75 µL/min or Reynolds number of 5.6, 11.2 and 16.8 (from top to bottom).

4. 4. 2. Live and fixed HeLa cell detection

Secondly, we measure live and fixed HeLa cells since live and fixed HeLa cells are known to have different stiffness. Both types of HeLa cells were suspended in PBS buffer solution (ρ=103 kg/m3, $\mu=1.05\times10^{-3}$ Pa•s) and were tested separately at a flow rate of 50 μL/min, i.e. the Reynolds number is of 11.2. Fig 4.6 shows the distribution of fixed and live HeLa cells over the cross section of the microfluidic channel. Detailed analyses on the HeLa cell distribution along the *x*-axis show a standard deviation (σ_x) of 12.89 μm for fixed cells and 8.66 μm μm for live cells at the Reynolds number of 11.2.

A more prominent and useful feature for cell classification in Fig. 4.6 (a) and (b) is that both live and fixed HeLa cells were tightly focused to narrow positions in the *y*-axis. At the Reynolds number of 11.2, the distribution of fixed HeLa cells was centered at 8.72 μm from the channel wall with a standard deviation (σ_y) of 1.03 μm. As a comparison, when live HeLa cells were introduced into the microfluidic device under the same condition, their distribution was centered at 9.34 μm from the channel wall with a standard deviation (σ_y) of 0.73 μm. Earlier reports showed that cell fixation by paraformaldehyde hardens cells due to the crosslink of protein.[16] As indicated in Fig. 4.6, the observation of live HeLa cells moving farther away from the channel wall compared to the stiffer fixed HeLa cells indicated that cells of the same size experienced a force influenced by their stiffness.[17] In the microfluidic channel, cells generally experience a lift force, mainly determined by their size, to achieve their equilibrium position, which is about ~0.2*h* from the channel wall.[18] However, the most exciting discovery from the experiment is the first direct observation of the effect of cell stiffness

on the cell distribution in a microfluidic channel. The flow between cells and the channel wall creates a repulsive lubrication force that results in a negative velocity and drives cells toward the channel wall. Thus, as discussed, because softer cells are more deformable to become thinner in the direction of force, the flow velocity difference across the cell is smaller than that of a stiffer cell.[17] Therefore, softer cells have their equilibrium positions farther away from the channel wall and travel faster than the stiffer cells. Our results in Fig. 4.6 agree well with the theory and show the feasibility of using cell stiffness as a biomarker for cell distinction. Like most circulating cancer cells that migrate through the tissue barrier to enter the blood vessel to metastasize,[19] live HeLa cells are more deformable than most normal cells. The equilibrium position of cells of different stiffness in a microfluidic channel might be used to identify cell phenotype or cell cycles.

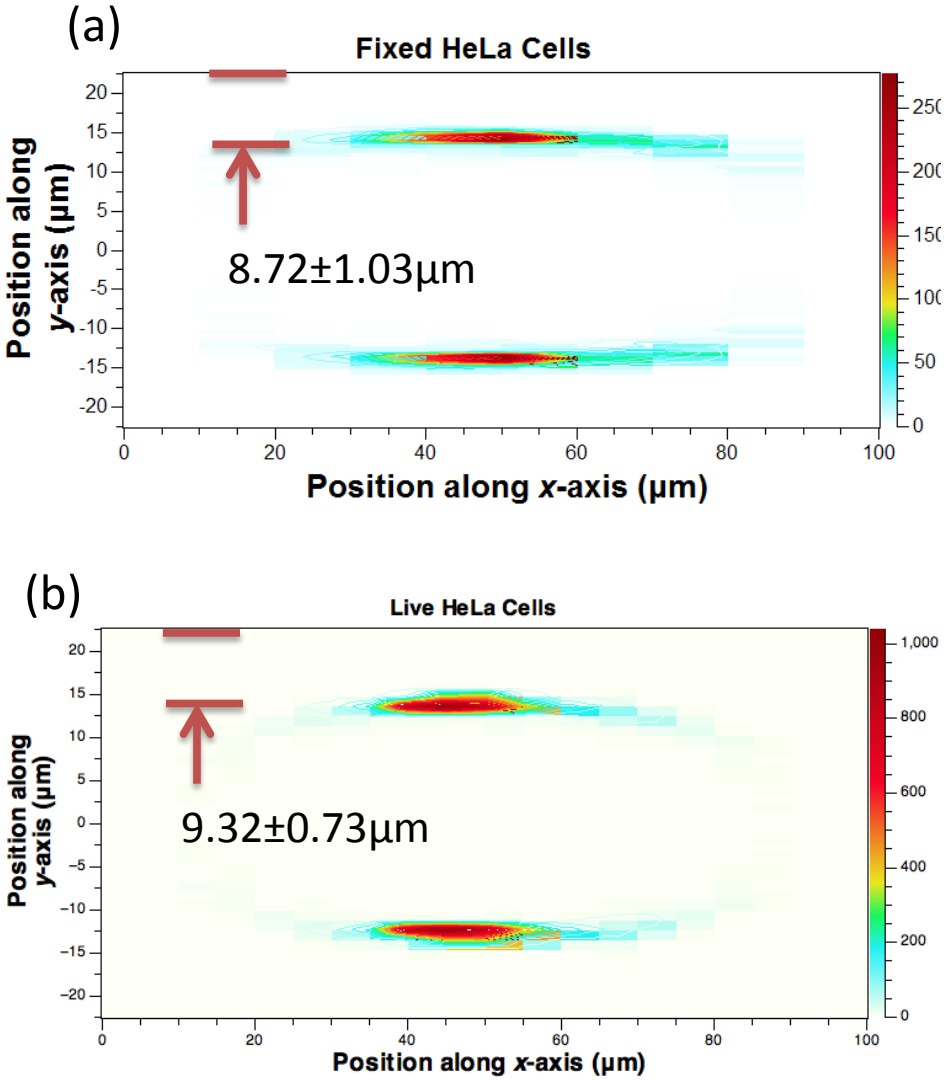

Figure 4.6 Population distribution plots for fixed HeLa cells (left) and live HeLa cells (right) over the cross section (100µm × 45µm) of the microfluidic channel. The Reynolds number of the sample is 11.2.

4. 4. 3. Classification of white blood cells and red blood cells

Next we performed experiment to classify white blood cells (WBCs) and red blood cells (RBCs) where the two groups of cells have different size and stiffness. We first characterize the WBCs and RBCs separately. After dilution of the RBC-lysed whole blood to a WBC concentration of around 10 counts/μL, WBCs were introduced into the device at the Reynolds number of 5.6 and 16.8, respectively. To test the RBCs, whole blood was diluted by 2 million times and introduced into the device at the Reynolds number of 5.6 and 16.8, respectively. A minimum of 1,500 encoded FS signals from each cell type were detected and analysed to create the population distribution plots. As shown in Fig 4.7 and 4.8, the distribution discrepancy along *y*-axis of red blood cells and white blood cells is reduced as the flow rate increases. It is indicated that the passive microfluidic devices that harness inertial effect for cell classification or sorting have the optimal operating flow rate and channel dimension for few types of cell. However, this can be improved by using multi-dimensional analysis that we will discuss in Chapter 5.

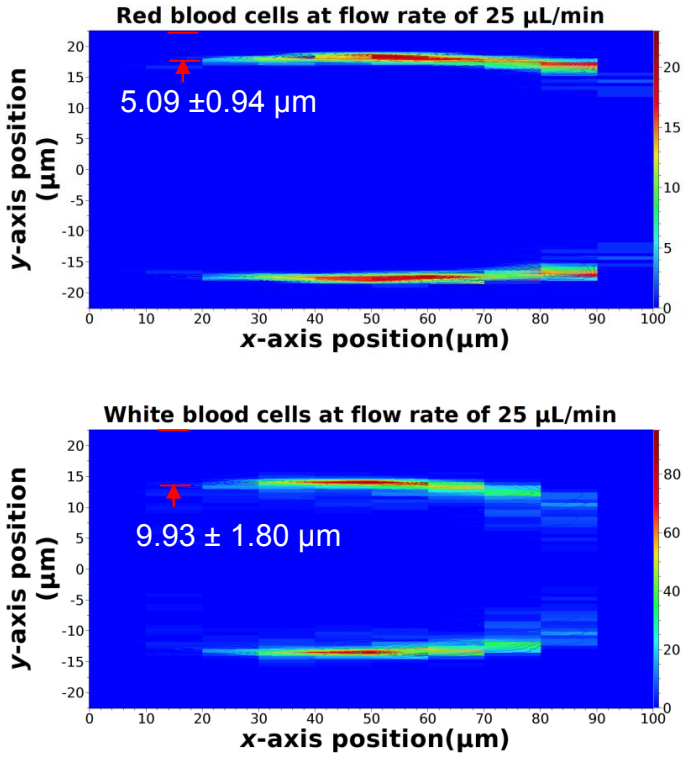

Figure 4.7 Population distribution plots for red blood cells (top) and white blood cells (bottom) over the cross section (100µm × 45µm) of the microfluidic channel. The Reynolds number of the sample is 5.6.

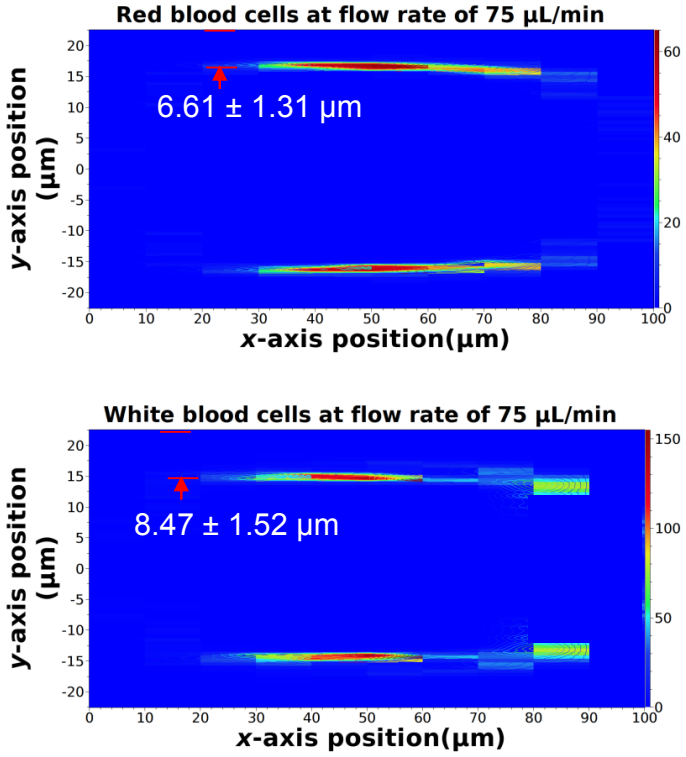

Figure 4.8 Population distribution plots for red blood cells (top) and white blood cells (bottom) over the cross section (100µm × 45µm) of the microfluidic channel. The Reynolds number of the sample is 16.8.

Since the previous HeLa cell study shows a tight distribution along the *y*-axis and the cell velocity approximately follows the parabolic function of the *y*-position in a rectangular channel, we hypothesized that velocity could be used as a convenient parameter for cell separation. Fig 4.9(a) shows the histogram for RBCs and WBCs using cell velocity as the parameter, and the results clearly support our hypothesis. The superimposed distribution plots for RBCs and WBCs are shown in Fig. 4.9(b). As predicted, two distinctive regimes for WBCs and RBCs are present, and the separation is primarily along the *y*-axis. From Fig. 4.9 (b), RBCs are mostly populated at a distance of 5.09 μm from the channel wall in the *y*-axis, with σ_y being 0.94μm. In contrast, larger WBCs are mostly populated at a distance of 9.93 μm from the channel wall, with σ_y being 1.80μm. If we define "gating" in the *x*-*y* plane in a similar fashion to user-defined gating with a commercial flow cytometer, then the separation between RBCs and WBCs can be even more distinctive and accurate than the single parameter plot in Fig. 4.9 (a). The experimental data implied that the inertial force induced by the size of cells dominates the distribution. Even though RBCs appears to be softer than WBCs, WBCs were farther away from the channel wall and travel faster because of their significantly larger size than RBCs. The results show that both cell size and cell stiffness contribute to the equilibrium position of cells in a microfluidic channel.

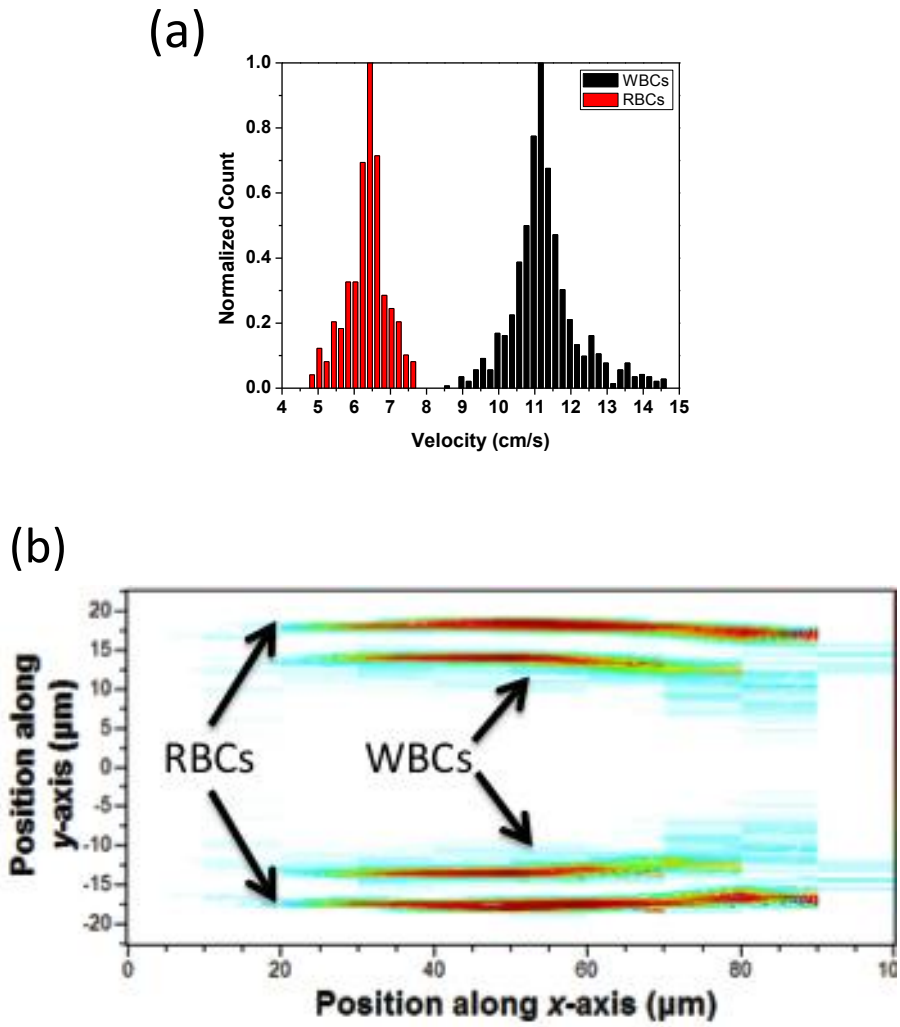

Figure 4.9 WBCs and RBCs tested separately at Re = 5.6. (a) Histogram of WBCs and RBCs using cell velocity as the parameter. (b) Superimposed population distributions for WBCs and RBCs within the microfluidic channel.

4. 4. 4. Neutrophil counting from whole blood

Using cell size and stiffness as biomarkers that can be faithfully represented in the population distribution plot, we exploited the feasibility of counting neutrophil population from a very small amount (5μL) of whole blood with minimum sample processing steps. Neutrophil count reveals the condition of the immune function and has been used as a key parameter for drug dosage and cytotoxicity in chemotherapy. To reduce the chance of hospital infection and cost, it is desirable to perform neutrophil test at point-of-care clinics or even more preferrably, at patient's residence in a self-administered fashion. Therefore, in this experiment we have limited the blood sample to 5 μL. Without adding any anticogulation agent, the blood sample was diluted in a buffer solution to a total volume of 1mL with RBC lysing agent. The RBC-lysed diluted blood was directly introduced to the device for testing without centriguge and pipetting. Thus the sample preparation procedure and the equipment requirement has been reduced to a minimum level suitable for self-administered test.

Within the WBC family, there exists a diverse size distribution among different subpopulations of WBCs. Essentially WBCs form a continuium in their size distribution, making cell classification by size alone very difficult without expensive flow cytometers that can give out very low intrinsic values of coefficients of variation (CVs). Since we discovered a method to measure cell positions within the channel and the cell positions depend strongly on cell stiffness, we have found an approach to count neutrophils from other types of WBCs such as lymphocytes and monocytes because of the high deformability of neutrophils. For example, being of similar size, neutrophils are more

than twice as deformable as monocytes. Neutrophils are slightly softer than lymphocytes[18] but also appreciably larger. All these are in favor of separating neutrophils from other WBCs (i.e. lymphocyes and monocytes) for an accurate neutrophil count.

Taking 5μL whole blood from purchased blood and from healthy volunteers, we prepared samples for neutrophil counts after RBC lysing and blood dilution. At *Re*=16.8, 112.5 μL of diluted blood sample passed through the sensing area of microfluidic devices within 90 seconds and the histogram of WBC velocity is shown in Figure 4.10 (a). The histogram shows a subpopulation of WBCs at a higher speed (i.e. velocity>30cm/s) than the rest of population which is believed to be from lymphocytes, partially monocytes and RBC residues since the samples were not centrifuged after lysing. The data become more revealing when they are presented in the cell distribution plot as illustarted in fig. 4.10 (b), where the cells with the velocity over 30cm/s are marked as red and considered as neutrophils. The population of neutrophils is clearly separated from that of other cells. To further verify the results from the microfluidic devices, we performed more blood tests from healthy donors and compared our results with the results from a commercial flow cytometer. In each run we flew 112.5μL of diluted blood through our device in 90 seconds and 200μL of diluted blood through a commercial flow cytometer in 15 minutes. The flow cytometer results in figure 4.11 showed three populations, representing the major groups of WBCs. Table 1 summarizes the results of neutrophil count from our device and the flow cytometer. Except for run 1, the results from our device agree with the flow cytometer results within 10%.

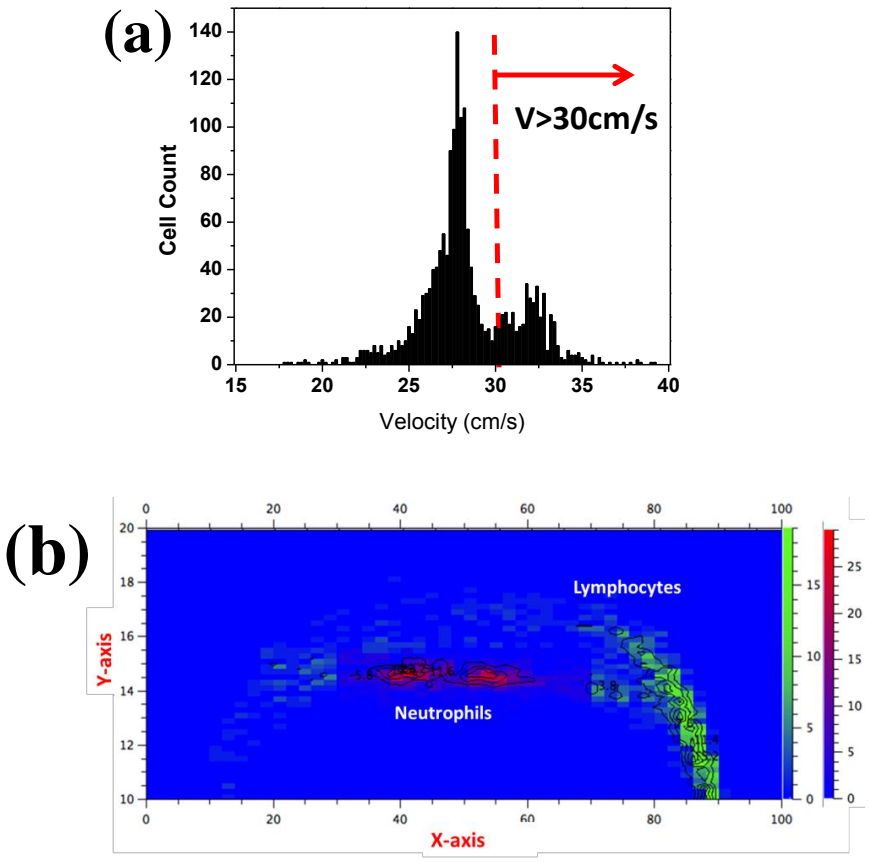

Figure 4.10 (a) Velocity histogram of white blood cells from 5μL RBC-lysed whole blood sample (870X dilution) at Re=16.8. The histogram shows a distinguishable population of neutrophils due to their high deformability. The peak on the left of the neutrophil (i.e. V<30cm/s) is the signal from other WBC types plus RBC residues since the sample did not go through centrifuge. (b) The distribution of RBC-lysed whole blood sample converted from (a) shows a separate band for neutrophils (red) from other cells (green).

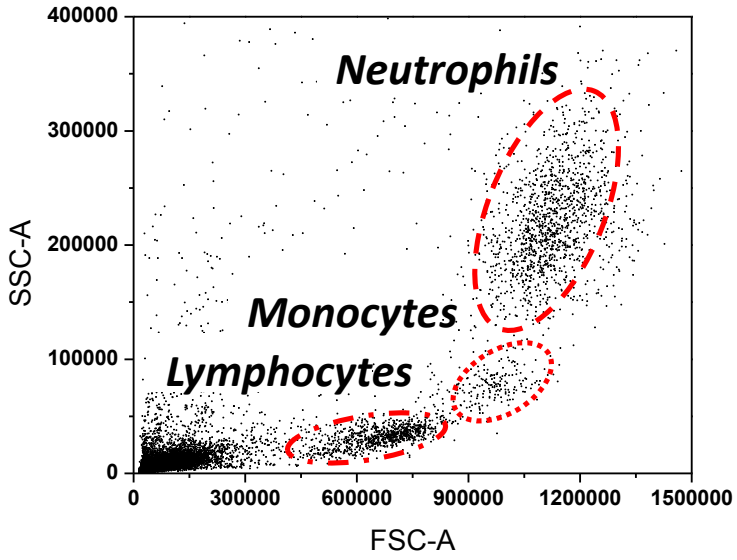

Figure 4.11 Scatter plot of 5µL RBC-lysed diluted whole blood sample (870X dilution) measured with a commercial flow cytometer (Accuri C6). Three populations clearly exhibit major WBC groups as the gating indicated

Table 4.1 Summary of test results from 870X diluted RBC-lysed blood samples usng our device and a commerical flow cytometer (Accuri C6)

Run of experiments	**I**	**II**	**III**	**IV**
Our device (neutrophil counts /μL)	5.80	7.74	5.72	6.20
Accuri C6 (neutrophil counts /μL)	4.38	7.09	6.39	6.77

4. 5. Conclusion

In this chapter, we demonstrated a unique optofluidic lab-on-a-chip device that can measure optically encoded forward scattering signals. From the design of the spatial pattern, we are able to acquire the position and velocity of each cell in the flow and generate 2-D cell distribution plots over the cross section of the channel. Moreover we have demonstrated that the cell distribution within the microfluidic channel is highly sensitive to cell size and stiffness. The latter is an important biomarker for cell classification, and our method offers a simple and unequivocal method to classify cells by their stiffness. We have proved this concept using live and fixed HeLa cells. Due to the softness of neutrophils compared to other types of white blood cells, we have demonstrated detection of neutrophils from other blood cells. Finally, we have performed the test using a very small amount of human whole blood. In a greatly simplified blood preparation process, skipping the usual steps of anticoagulation, centrifuge, anti-body labelling or staining, filtering, etc., we have demonstrated that our device and detection principle can count neutrophils in whole human blood.

Our system is compact, inexpensive, and simple to fabricate and operate, having a commodity laser diode and a Si PIN photoreceiver as the main hardware. Although the results are still preliminary, the studies indicate that this optofluidic device holds promise to be a point-of-care and home care device that measures the immune function of patients, which is of great value to cancer patients undergoing chemotherapy.

References:

1. M. Toner and D. Irimia, Annu Rev Biomed Eng **7**, 77-103 (2005).

2. D. Holmes and H. Morgan, Anal Chem **82** (4), 1455-1461 (2010).

3. H. Yun, H. Bang, J. Min, C. Chung, J. K. Chang and D. C. Han, Lab Chip **10** (23), 3243-3254 (2010).

4. H. W. Hou, A. A. S. Bhagat, A. G. L. Chong, P. Mao, K. S. W. Tan, J. Y. Han and C. T. Lim, Lab Chip **10** (19), 2605-2613 (2010).

5. C. S. Chen, M. Mrksich, S. Huang, G. M. Whitesides and D. E. Ingber, Science **276** (5317), 1425-1428 (1997).

6. J. Crawford, D. C. Dale and G. H. Lyman, Cancer **100** (2), 228-237 (2004).

7. N. V. Sipsas, G. P. Bodey and D. P. Kontoyiannis, Cancer **103** (6), 1103-1113 (2005).

8. L. R, S. DL, R. LA and L. SA, Discov. Med. **5** (27), 303-308 (2005).

9. P. Kiesel, M. Bassler, M. Beck and N. Johnson, Appl Phys Lett **94** (4) (2009).

10. S. H. Cho, W. Qiao, F. S. Tsai, K. Yamashita and Y. H. Lo, Appl Phys Lett **97** (9) (2010).

11. A. A. S. Bhagat, S. S. Kuntaegowdanahalli and I. Papautsky, Microfluid Nanofluid **7** (2), 217-226 (2009).

12. S. C. Hur, N. K. Henderson-MacLennan, E. R. B. McCabe and D. Di Carlo, Lab Chip **11** (5), 912-920 (2011).

13. J. P. Beech, S. H. Holm, K. Adolfsson and J. O. Tegenfeldt, Lab Chip **12** (6), 1048-1051 (2012).

14. S. C. Hur, H. T. K. Tse and D. Di Carlo, Lab Chip **10** (3), 274-280 (2010).

15. D. Di Carlo, D. Irimia, R. G. Tompkins and M. Toner, P Natl Acad Sci USA **104** (48), 18892-18897 (2007).

16. V. Lulevich, T. Zink, H. Y. Chen, F. T. Liu and G. Y. Liu, Langmuir **22** (19), 8151-8155 (2006).

17. S. Mortazavi and G. Tryggvason, J Fluid Mech **411**, 325-350 (2000).

18. B. Chun and A. J. C. Ladd, Phys Fluids **18** (3) (2006).

19. M. Lekka, P. Laidler, D. Gil, J. Lekki, Z. Stachura and A. Z. Hrynkiewicz, Eur Biophys J Biophy **28** (4), 312-316 (1999).

Chapter 4 or portion thereof has been published in *Lab on a Chip*, Tsung-Feng Wu, Zhe mei, and Yu-Hwa Lo, 12, 3791 (2012)

Chapter 5

Label-free Optofluidic Cell Classifier Utilizing Support Vector

In this chapter, we exhibit a multi-dimensional analysis to enhance the performance of cell classification by harnessing our optofluidic lab-on-a-chip device that can measure optically encoded forward scattering signals. From the design of the spatial pattern, the position and velocity of each cell in the flow can be detected and then

a spatial cell distribution over the cross section of the channel can be generated. According to the forward scattering intensity and position information of cells, a data-mining method, support vector machines (SVMs), is applied for cell classification.

In this study, breast cancer cells (MCF-7) and human white blood cells are used to demonstrate the capability of our system. With the help of SVMs, the multi-dimensional analysis can be performed to significantly increase all figures of merit for cell classification. We show marked improvements in the performance of cell classification, measured by the rates of sensitivity (85.87%), specificity (98.32%), and accuracy (93.95%)

5. 1. Introduction

The detection and classification of biological cells with high performance tools are used for clinical diagnosis of diseases.[1-7] Today most of biomedical test instruments for cell assays are set up in hospitals or medical institutes. For large populations living in areas where such medical infrastructure is lacking, timely diagnosis and monitoring of patent conditions becomes difficult and impractical. Point-of-care is widely recognized by the global health care community as a promising approach to address the above concern. The successful implementation of the point-of-care relies on the availability of low cost, easy-to-operate, and accurate medical equipment suitable for point-of-care clinics. Lab-on-a-chip devices possess some inherent merits for point-of-care applications so have become the foci of biomedical device research. For clinical tests, samples such as blood and bodily fluids (saliva, sputum, and urine) are easy to

acquire with minimum invasiveness (compared with biopsy) and have great values in disease diagnosis and measurements of patients' health conditions. Therefore a large number of lab-on-a-chip devices for point-of-care applications are microfluidic devices for cell-based and molecular-based assays. However, most lab-on-a-chip devices today require cell labelling for cell detection, classification, and isolation from the mixture of analytes.[8] The procedures of cell labelling are usually time-consuming, hard to control, and expensive because of the high cost of reagents (e.g. fluorescently labelled anti-bodies). Also, the equipment used to detect the labelled signals is usually highly sophisticated, involving complex optics, laser sources, and sensitive photodetectors such as photomultiplier tubes (PMTs).[9] Both the complicated and costly sample preparation procedures and the sophisticated instrument impose serious constraints on the use of such devices in point-of-care clinics. Therefore, a few groups, including ours, have moved our attention to devices that can function without cell labelling. The challenge for label-free cell-based assay is low sensitivity and specificity. Compromises in either area lead to high false positive and false negative rates, which greatly diminishes the device efficacy for point-of-care devices.

To achieve label-free cell detection and classification in high accuracy, as described in the previous chapter, we demonsrated a method of using a spatial mask to encode the scattering signals of beads or cells in microfluidic channels in Chapter 3 and 4. We demonstrated that the optical-encoding method enables us to detect forward scattering (FS) and large angle scattering (LAS) signals as well as the velocity and position of each individual cell according to its hydrodynamic behaviours governed by

parameters such as cell volume, cell shape, and in particular, cell stiffness. Thus without cell labelling, we have developed a method to measure many cell properties that can be used as biomarkers for cell classification (e.g. live and dead cells, red blood cells and white blood cells, subclasses of white blood cells such as lymphocytes and neutrophils). This approach appears to be highly promising, with a demonstrated ability to detect neutropenia (low neutrophil counts) for patients undergoing chemotherapy.

However, to explore the full potential of the technique for point-of-care clinics, we will need efficient cell classification algorithms to improve the detection accuracy and expand its application to more diseases and health parameters. In this article, we apply a supervised computer learning method to enhance the performance for cell classification. Support vector machine (SVM)[10-14] is one of the most powerful computer learning tools for bioinfomatics analysis. SVMs are computer-learning algorithms that use the prior knowledge to classify the unknown events. For cell classification, SVMs employ a kernel function and use existing information in the database to form a training model. After the training routine, SVMs are able to classify samples under test by their type. In addition, SVMs are able to operate in a multi-dimensional feature space to achieve higher accuracy in cell classification. Combining the SVM classification method with the encoding method of the lab-on-a-chip microfluidic device, the device performance can be significantly improved for unlabelled biological detection.

5. 2. Design and principal of the optical-coding mifrofluidic device

In the previous chapters, we have demonstrated the fabrication and opertation of the optical-coding device. Fig 5.1 briefly shows the working principal of the optical-coding technique. For more information, readers are encouraged to review Chapter 3.

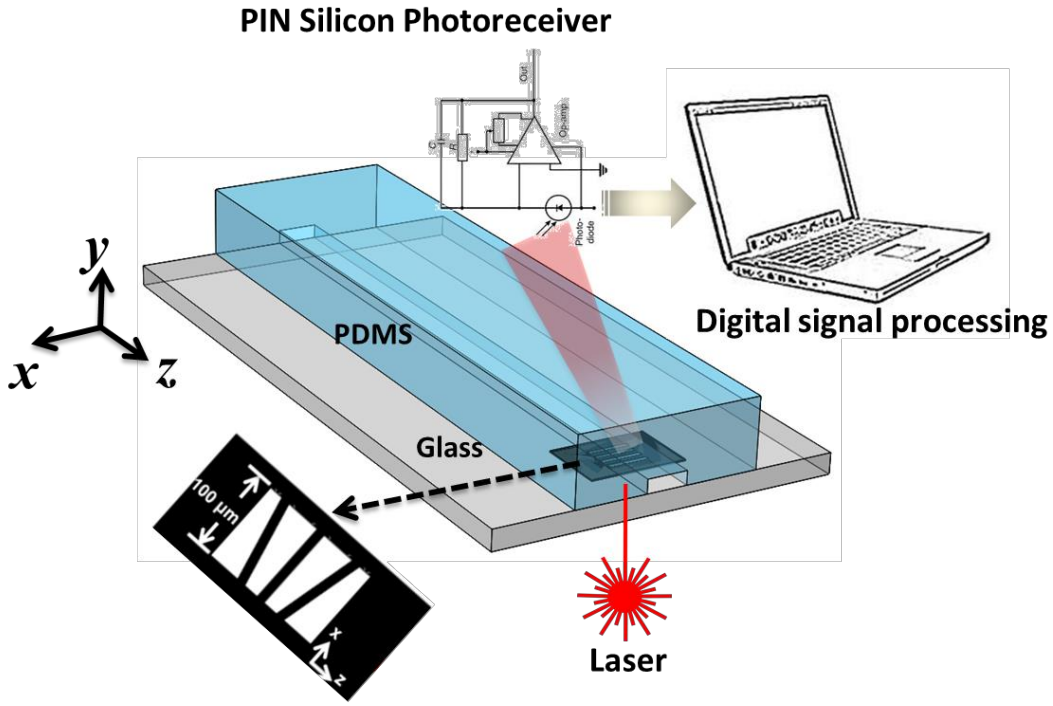

Figure 5.1 A scheme of the optical-coding microfluidic channel. The beads or cells are interrogated with a laser source. The laser light is encoded after passing through the sensing area to provide the position information of beads or cells.

5.3 Theory of Support Vector Machines (SVMs)

For cell classification, the ideal scenario is to establish a classifier that divides all components into well-defined groups. However, a classifier with a clear boundary rarely exists for biological samples because of inevitable variations within the class. Increasing the dimensions of feature space can improve the performance for sample classification under such situations. One can expand those inseparable cases into a higher-dimensional feature space using the appropriate expression information. By doing so, it becomes more likely to define the hyperplane for cell classification. However, traditional learning methods in higher-dimensional feature space are usually accompanied with overfitting problems because artificially separated hyperplanes might find trivial solutions.

The algorithms of SVMs create a classifier that gives rise to a maximal margin while avoiding the overfitting problem at the same time. The simplest way for classification is to find a linear separating hyperplane, shown in Fig 5.2(a). Assume an expression vector x to each data point, SVMs would have a decision function $d(x,w,\mathrm{b})=w\bullet x+\mathrm{b}$, where $\bullet$ means dot product, w is the normal vector to the hyperplane, and b is a scalar called bias factor. Because the output of $d(x,w,\mathrm{b})$ is a scalar, the indicator function, F, is defined as the sign of $d(x,w,\mathrm{b})$ that indicates which group (class) each data point belongs to. The optimal canonical hyperplane with functional margin of 1 is the contour where the decision function is equal to zero, i.e. $d(x,w,\mathrm{b})=w\bullet x+\mathrm{b}=0$, and the separating margin, γ, for both sides from the hyperplane is maximal, i.e. $2\gamma=2/\|w\|$. The principle of SVMs is to maximize the separating margin to ensure every data point is distant from the decision boundary by at least γ. After the hyperplane of SVMs is

defined, an unknown vector x_N is classified according to the value of indication function, F, defined as the sign of $d(x_N,w,b)$.

In general, data might not be classified linearly because of the mislabelled events in the database or inexistence of linear classifiers. The former issue can be addressed by introducing a soft margin that allows some data points to be in the wrong side of hyperplane.[10] For the latter problem, as illustrated in Fig 5.2(b), a nonlinear classifier has to be defined to maximize the separating margin, by using an adequate kernel function, $K(x_i, x_j)$. Since SVM algorithms were originally based on a linear machine learning technique, introducing a nonlinear kernel function is an effective route to address the problem without changing the fundamental computation algorithms. In this case, the decision function should be substituted with the designed kernel functions that enable the SVM algorithms to achieve the nonlinear hyperplane with maximal margin. The nonlinear hyperplane is especially important for classification in a multi-dimensional feature space, as shown in Fig 5.2 (c). Once the analysis is conducted in n-dimensional feature space, the (n-1)-dimensional hyperplane is needed. The nonlinear kernel functions exist in various forms such as polynomial, hyperbolic tangent, inverse multi-quadratic and Gaussian radial basis function (RBF). In this article, we employ a Gaussian RBF kernel $K(x_i, x_j) = \exp(-\gamma||x_i - x_j||^2)$ because it has a smaller number of hyper-parameters to allow for less complex model selection and higher accuracy for our applications.

In this capter, we trained the SVMs to recognize expression data, including FS, positions of x-axis and positions of y-axis. These factors were recorded from beads or

biological cells, thus representing the true behaviours of samples flowing in the microfluidic channel. In the training procedure, two-thirds of the data were used to establish the hyperplane and the remaining one third of data were tested for the accuracy. Afterwards, we used data from several separate runs of experiment to repeatedly test the algorithm. The open source SVMs software [14] was used in the present work.

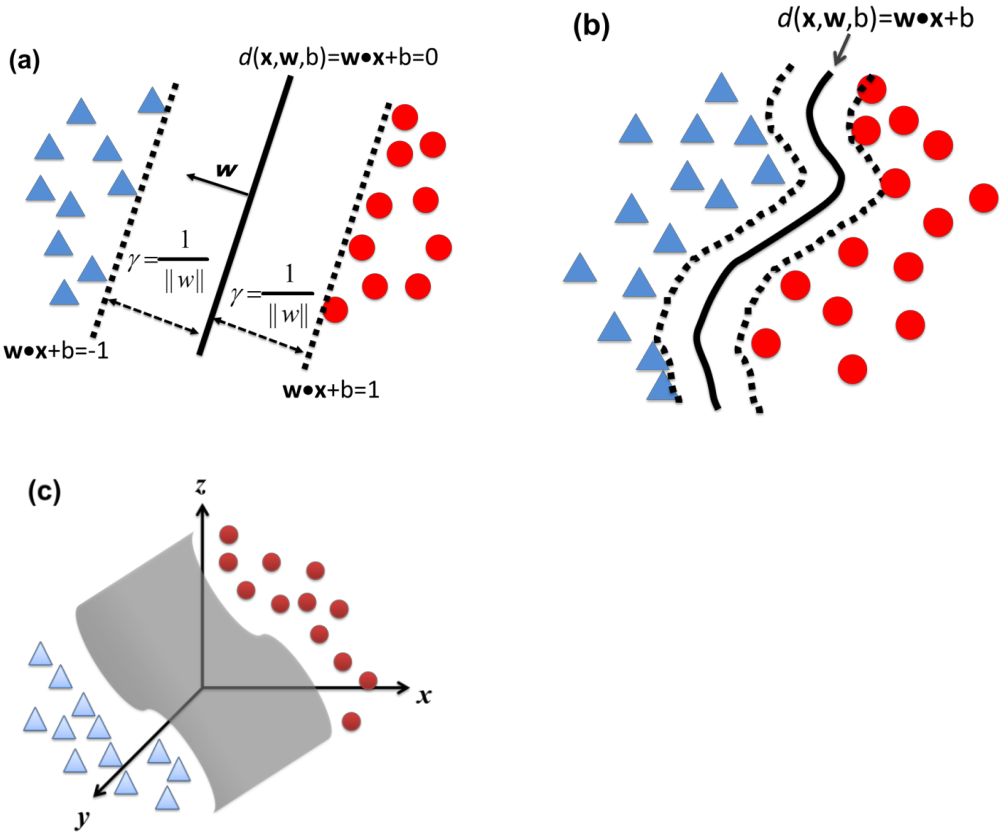

Figure 5.2 (a) A hyperplane formed by SVMs for a linear classification. A filled red circle represents type I and a filled blue triangle represents type II. The thick line is the optimal hyperplane for classification, with *w* being the normal vector of hyperplane. Two dashed lines are the margins with a distance, γ, from the hyperplane. The condition γ= 1/||*w*|| is required to achieve functional margin for the canonical hyperplane. (b) A nonlinear hyperplane formed by SVMs with a nonlinear kernel function. (c) A nonlinear hyperplane in 3-dimensional space represented the multi-parameter analysis using SVMs.

5. 4. Preparation of sample

To characterize optical-coding devices with selected cell types, we have prepared samples with breast cancer cells (MCF-7 cells) and white blood cells (WBCs). MCF-7 cells were cultured in the growth medium in a humidified incubator at 37°C in 5% CO_2 and then fixed with paraformaldehyde prior to the experiment. Whole blood samples used to produce WBC samples were purchased from the blood bank. To prepare WBC samples, whole blood was lysed with commercial lysing buffer (eBioscience, CA). The buffer solution used to re-suspend cells in this study consists of 10mM ethylenediaminetetraacetic acid (EDTA), 1% bovine serum albumin (BSA), and 1X phosphate buffered saline (PBS).

5. 5. Results and Discussion

Using a knowledge-based algorithm to assist the classification of cells, we first trained SVMs to establish the hyperplane. To set up the database, data from MCF-7 cells and white blood cells (WBCs) were collected separately at a flow rate of 75 μL/min (the Reynolds number=16.8). Figure 5.3 (a) shows the superimposed contour plot of *x*-axis position versus forward scattering intensity of MCF-7 cells and WBCs. In general, MCF-7 cells have a larger diameter and produce stronger forward scattering signals than WBCs because of their larger number of scattering centers. Fluid dynamically, larger particles inside the microchannel experience a stronger lift force that drives the particles closer to the center of the microchannel.[15] This lift force is given as $F_L = \rho G^2 C_L d^4$, where ρ is the density of fluid, G is the fluid shear rate ($G = 2U_f/H$), C_L is

the lift coefficient (which for microchannels remains constant when Re<100), and d is the particle diameter. As observed, the x- position of MCF-7 cells is closer to the centerline (i.e. 50 μm) than the x- position of WBCs. Furthermore, due to the parabolic velocity profile within microfluidic channels, the y-position of particles can be calculated according to the parabolic relation, $\upsilon(x, y) = \upsilon_{Max}(x)\,[1- (y/h)^2]$, where $\upsilon(x, y)$ is the velocity at a specific position, $\upsilon_{Max}(x)$ is the velocity at position x and the middle of the channel (i.e., at y=0) obtained from the COMSOL simulation results, and h is the half-height of the channel, 22.5 μm in this study. Figure 5.3 (b) and (c) shows the spatial distribution contour plots of WBCs and MCF-7 cells on the x-y plane, respectively. It is found that in the y–direction, a small yet clear separation between MCF-7 cells and WBCs is present, by a distance of 1.19 μm. This spatial separation in y-axis is attributed to different lift forces due to differences in cell size and cell stiffness. Since MCF-7 cells are larger and softer than most WBCs, both factors drive MCF-7 cells closer to the center of the channel in the y-direction[16]. In the microfluidic channels, softer cells are more easily deformed into shapes that follow the streamline more closely, yielding a smaller velocity difference across the cells than stiffer cells.[17] As a result, softer cells experience a weaker drag force than stiffer cells, moving farther away from the channel wall and gaining a faster speed. In this manner, cell deformity becomes an effective biomarker for cell classification in the microfluidic channel.

The scattering signals from cells have been detected in many microfluidic devices. However, because of large variations of the signals and lack of effective methods to relate the scattering signals to the cell properties, scattering signals have not

been used as a reliable method for cell classification. With the optical-coding microfluidic devices, the distribution of cells over the cross section of the microfluidic channel is explored to allow the multi-dimensional analysis by SVM analysis. Although SVMs have been widely used for bioinformatics, it is the first time the method is used to achieve accurate cell identification. SVMs can automatically create the separating boundary to classify and enumerate cells for different populations, which reduces the error by manual gating. To establish the separation hyperplane by SVMs, the defined database was fed into SVMs first and the analysis process would take around 3 hours to deal with about 2,000 data points. Once the hyperplane has been built, the unknown samples can be analyzed within 30 mintues for each batch of dataset. The prediction performance of SVMs is judged by seven indicators: true positive (TP), true negative (TN), false positive (FP), false negative (FN), accuracy, sensitivity and specificity. The key figures of merit are accuracy, sensitivity and specificity defined as follow,

$$Accuracy = (TP + TN)/(TP + TN + FP + FN) \quad (5.1)$$

$$Sensitivity = TP/(TP + FN) \quad (5.2)$$

$$Specificity = TN/(FP + TN) \quad (5.3)$$

The outcomes of SVMs analysis are summarized in Table 5.1. The total events of MCF-7 cells and WBCs are 842 and 2324, respectively. For each parameter (FS, *x*-position, *y*-position), SVM analysis was performed on three separate trails. When we used FS as the only parameter for SVMs, the average values of sensitivity and accuracy

are ~56.86% and 87.96%, although the specificity value (a measure of true negative rate) is very high: 99.26%.

Adding the parameter of x-axis position to the SVM analysis slightly increases the sensitivity to ~59.93%. This modest contribution suggests that although MCF-7 cells have larger FS intensity and more focused to the center position in the *x*-axis, these effects are insufficient for highly accurate cell classification. In contrast, adding the third parameter (*y*-position) to the SVMs significantly increases the accuracy and sensitivity up to 93.95% and 85.87%, respectively, while maintaining a high value of specificity (98.32%). The results demonstrated that expanding the hyperplane to higher dimensions can significantly improve the performance for cell classification. The 2-dimensional and 3-dimensional hyperplanes are illustrated in Fig 5.4 (a) and (b), where the hyperplane in Fig 5.4 (b) is established using about one-third of data points for clarity in visual illustration. The minor misclassification of SVMs might result from the size variation between MCF-7 and WBCs cells, resulting unresolved parameters. However, these results still demonstrate the efficacy of SVM algorithms with optically encoded forward scattering signals from a lab-on-a-chip microfluidic device

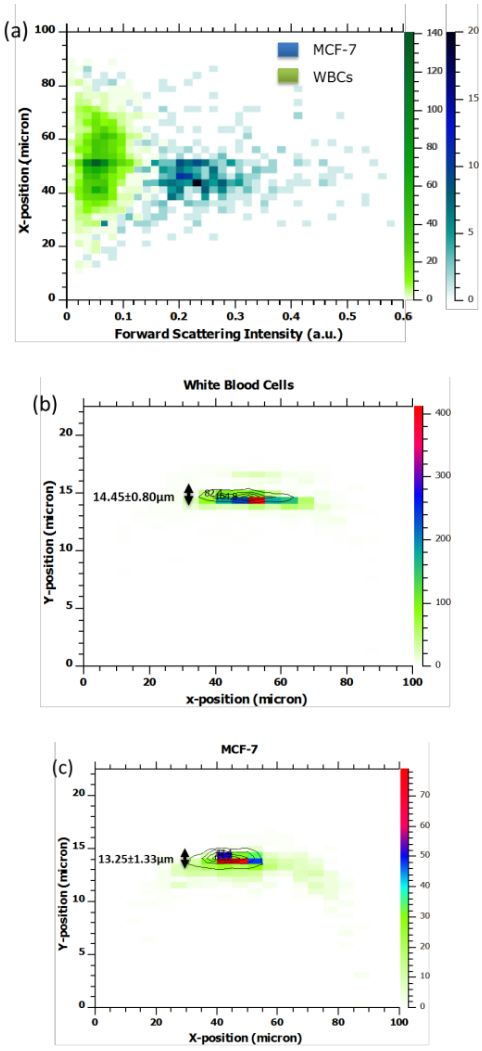

Figure 5.3 (a) The superimposed contour plot of *x*-axis position versus forward scattering intensity for MCF-7 cells and white blood cells. The flow rate is at 75μL/min. (b) and (c) The spatial distribution contour plots of white blood cells and MCF-7 cells on the cross section of the half microchannel, respectively. Color bars in each figure represent the density of cell distribution.

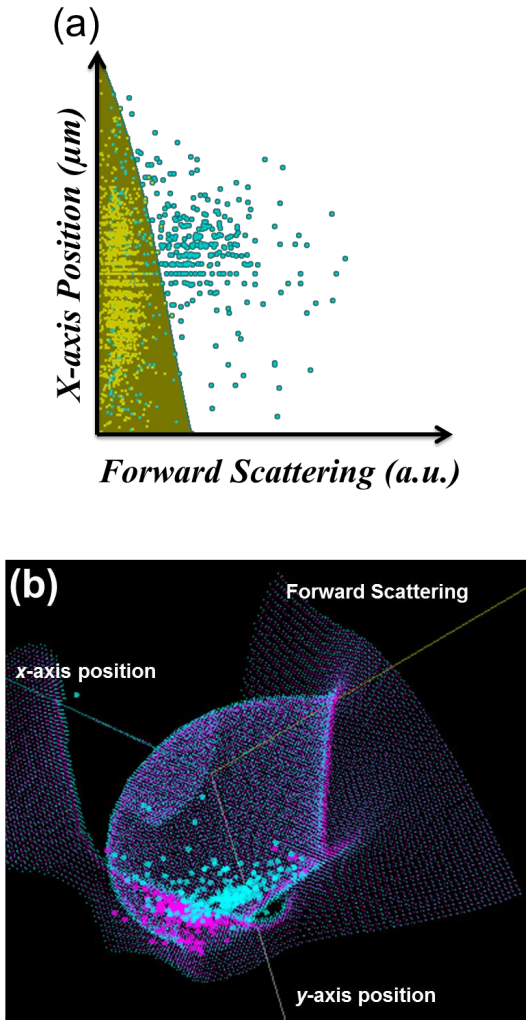

Figure 5.4 (a) The hyperplane created by SVMs for 2-parameter cell classification, using forward scattering signals and position of cells along the x-axis. (b) The hyperplane created by SVMs for 3-parameter cell classification with the information of cell positions along x- and y-axes and the forward scattering intensity. This nonlinear hyperplane in 3-dimensional space allows multi-parameter analysis to achieve higher accuracy for cell classification.

Table 5.1 Summary of support vector machines for different dimensional analysis

Parameter	Trail	TP	TN	FP	FN	Accuracy	Sensitivity	Specificity
FS	I	156	762	12	124	87.09%	55.71%	98.45%
	II	169	770	4	114	88.83%	59.72%	99.48%
	III	155	773	1	126	87.96%	55.16%	99.87%
FS, X	I	161	761	13	119	87.48%	57.50%	98.32%
	II	164	773	2	118	88.56%	58.16%	99.74%
	III	179	754	22	100	88.65%	64.15%	97.16%
FS, X,Y	I	189	762	13	90	90.22%	67.74%	98.32%
	II	243	750	24	40	93.95%	85.87%	96.90%
	III	227	762	13	53	93.74%	81.07%	98.32%

5. 6. Conclusion

Forward scattering is the most common and easiest to detect signal from biological cells, but it has been a great challenge to extract biologically relevant information from the forward scattering signal alone. Our unique optical coding technique produces forward scattering signal that also contains information about cell speed and position, and such information is closely related to cell properties such as cell size, cell shape, and cell stiffness. For the first time to our knowledge, we have applied the SVMs method to perform multi-dimensional analysis of the encoded forward scattering signals. The results have shown significant enhancement in the accuracy, sensitivity, and specificity for cell classification. The encouraging initial results suggest the potential value of combining the lab-on-a-chip technology and SVMs data analysis method in point-of-care clinics.

References:

1. C. D. Chin, V. Linder and S. K. Sia, Lab Chip **7** (1), 41-57 (2007).

2. B. Cline, K. Kuhlmann and R. Luo, Microsc Microanal **15**, 870-871 (2009).

3. D. Mabey, R. W. Peeling, A. Ustianowski and M. D. Perkins, Nat Rev Microbiol **2** (3), 231-240 (2004).

4. X. L. Mao and T. J. Huang, Lab Chip **12** (8), 1412-1416 (2012).

5. A. W. Martinez, S. T. Phillips, G. M. Whitesides and E. Carrilho, Anal Chem **82** (1), 3-10 (2010).

6. G. M. Whitesides, Nature **442** (7101), 368-373 (2006).

7. P. Yager, T. Edwards, E. Fu, K. Helton, K. Nelson, M. R. Tam and B. H. Weigl, Nature **442** (7101), 412-418 (2006).

8. J. Nam, H. Lim, D. Kim and S. Shin, Lab Chip **11** (19), 3361-3364 (2011).

9. T. P. Forbes and S. P. Forry, Lab Chip **12** (8), 1471-1479 (2012).

10. W. L, Springer (2005).

11. M. P. S. Brown, W. N. Grundy, D. Lin, N. Cristianini, C. W. Sugnet, T. S. Furey, M. Ares and D. Haussler, P Natl Acad Sci USA **97** (1), 262-267 (2000).

12. S. Ramaswamy, P. Tamayo, R. Rifkin, S. Mukherjee, C. H. Yeang, M. Angelo, C. Ladd, M. Reich, E. Latulippe, J. P. Mesirov, T. Poggio, W. Gerald, M. Loda, E. S. Lander and T. R. Golub, P Natl Acad Sci USA **98** (26), 15149-15154 (2001).

13. T. S. Furey, N. Cristianini, N. Duffy, D. W. Bednarski, M. Schummer and D. Haussler, Bioinformatics **16** (10), 906-914 (2000).

14. C. C. Chang and C. J. Lin, Acm T Intel Syst Tec **2** (3) (2011).

15. S. C. Hur, H. T. K. Tse and D. Di Carlo, Lab Chip **10** (3), 274-280 (2010).

16. S. C. Hur, N. K. Henderson-MacLennan, E. R. B. McCabe and D. Di Carlo, Lab Chip **11** (5), 912-920 (2011).

17. S. Mortazavi and G. Tryggvason, J Fluid Mech **411**, 325-350 (2000).

Chapter 5 or portion thereof has been published in *Sensors and Actuators B: Chemical*, Tsung-Feng Wu, Zhe mei, and Yu-Hwa Lo, 186, 327 (2013)

Chapter 6

Reconstruct signature of cellular nucleus by using label-free scattering-imaging-based cytometry

In this chapter, we demonstrated a label-free scattering-based-cytometer for directly reconstructing the signature of cell nucleus. By using the low-cost, compact and easy-to-operate optics, we demonstrated that the large angle scattering light from cells can be recorded on the commercial CMOS imagers. This method lights on the possibility of portable imaging cytometer that can harness the omnipresent smartphone camera for unlabelled bead and cell analysis.

6. 1. Introduction

The optical techniques of flow cytometry have been developed for several decades[1, 2] because of the capability of providing the statistical data for the cell sorting and analysis of cell size, complexity, cell cycle and cellular phenotyping. Advanced systems can collect various fluorescence and scattering signals from thousands of cells a second. Cell population of a mixed or unknown sample can further identified by multi-parametric analysis consisted of forward scattering, side scattering and fluorescence signals. However, the deeper understanding of the cellular structure is still unavailable. For example, the cell morphology or, more importantly, the intracellular structure cannot be retrieved with the traditional flow cytometer. To gather entire information of cells, images of cells become necessary because cellular images carry more insight that is hardly resolved from scattering or fluorescence measurement. The confocal microscope is usually used to produce fluorescently a 3-dimensional image of inner cell structure, but long time consumption of taking a single cell sample cannot be compromised when a batch of cell samples needs to be analyzed. Taken together the demand of cell images and throughput, imaging cytometry holds a solution to combine microscopy and flow cytometry, after first introduced in 1979.[3, 4] Like the standard microscopy, imaging cytometry can collect all kinds of modes, including scatted and transmitted light, fluorescence, etc., to establish complementary information of cells. Although the resolution of imaging cytometry is currently not comparable to confocal microscopy, the capability of imaging cytometry to resolve sub-cellular structueres is adequate, especially for the quantitative assessment of cellular phenotyping within

decent timespan. There have been many commercial imaging cytometers in the market for users to proceed the cellular analysis and eliminating manual error from eyeball counting,[5-7] but the commercially available machines are usually in benchtop version that cannot address the purpose of point-of-care applications. Due to the advancement of microfabrication, optical imaging techniques have been realized in microfluidics devices.[8, 9] For example, microfluidic imaging flow cytometers have been demonstrated to observe cell cycle,[10, 11] image blood cells,[12] or evaluate cytotoxicity.[13, 14] To improve the resolution, the concept of light sheet has been introduced in imaging cytometry.[15, 16] Recently, 3-dimensional images of phytoplankton can be generated by a light sheet fluorescence imaging flow cytometer.[17] However, the fluorescent-labeling of cells is the necessity to enhance precision observation in most imaging flow cytometry. In the reality, labeling of cells causes costly procedure prior to use and negatively affects the viability and behavior of cells that are unwanted for the following applications. On the other hand, the bulky imaging system will be the hurdle when integrating with microfluidic imaging cytometers for point-of-care needs. Fortunately, high resolution CMOS cameras that can be used as imaging system have become omnipresent in our daily life due to the fast growth of cellphone and mobile devices. Advanced CMOS imagers can capture millions of pixels at once and tens of frames per second, holding the potential for point-of-care applications.[18, 19]

Although a lot of effort has been spent on the development of imaging cytometry, a label-free and highly portable imaging cytometry platform that can reveal the intracellular structure is still lacking. Understanding the sub-cellular structures, i.e.

the shape, size and orientation of nucleus, may be more important than morphologies of cells. It is not only because the stiffness of nucleus is usually 2 to 10 times greater than the other cellular structures else,[20, 21] which can reduce external factors causing the error of analysis, but also the changes in the shape and size of nucleus are associated with cancerous mechanism,[22-26] aging,[27, 28] and senescence.[29] For instance, when the size increase of cancerous nucleus is observed, it is indicated that cancer cells become more aggressive to begin the metastatic process.[30, 31]

In this chapter, a label-free scattering-imaging-based cytometry platform that can be highly integrated with CMOS imagers for portable imaging system has been demonstrated to interrogate the sub-cellular structures and plot a signature for cell classification. The incoherent light source is refracted by designed microlens (μlens) and then penetrates a narrow slit to form a light sheet beam, which is less than 4 μm wide. By imaging scattering light from various cell types, we have realized the functionality of light sheet scan on examining the intracellular structure. Because it is believed that the refractive index of cells is associated with its protein density,[32, 33] the nucleus is considered to be the place that has densest protein content in sub-cellular structure. With the light sheet beam, we show the darkfield scattering imaging of nucleus and achieve the reconstruction of nuclear signature as a marker for cell classification. In our platform, the existence of brightfield imaging can be a self-contained verification to clearly delineate the cell boundary. Besides, since the change of nucleus would take place throughout the cell cycle[34] and cell cycle has an essential role in both biological clinical applications,[35, 36] we also control the cell cycle for further observation. Finally,

we implement our platform to interrogate the human white blood cells and manifestly prove the different nuclear signatures for granulocytes and agranlocytes. Without using any fluid pumps, the samples can be tested with the smeared way that further cut down the total cost. Although we have demonstrated the functionalities of detecting scattering signals in the previous chapters, it is the first time that directly measurement of sub-cellular structures by using a scattering-imaging-based cytometer which is compatible with portable CMOS imagers and, more importantly, label-free sample preparation is applied. We believe our findings would innovate more applications for point-of-care or further telemedicine needs.

6. 2. Fabrication of scattering-imaging-based cytometer platform

The general way to generate the topology required for microlens (μlens) is to thermally reflow the photoresist that is photographical patterned on the substrate. As shown in Figure 6.1, the pattern of μlens on the transparent photo-mask (CAD/Art services, Inc.) was designed as the rectangle with 2200 μm × 160 μm (length × width). To obtain the thin light beam, a 2 × 2 cm2 square silver film with an opening of 2000 μm × 10 μm (length × width) was deposited on the thin glass (~150 μm in thickness) by conventional lift-off process. The double spinning process was adapted to retrieve the thick photoresist layer. SPR220-7.0 (Shipley) photoresist was first coated at 1200 rpm for 40 seconds and baked at 80 °C for 1 minute. Second spin-coating process was implemented at 1200 rpm for 40 seconds. Prior to exposure process with using Karl Suss MA6 mask aligner, the as-spun sample should have a hold time for at least one day

in the ambient environment. The alignment between the layer of μlens and as-deposited metal layer should be carefully executed to keep the 5 μm of edge-to-edge spacing along the entire length direction for both layers. After the exposure process, the sample was immersed into the developer until the photoresist of unpatterned area vanished, followed by deionized water rinse. The remained photoresist patterns were melted by thermal heating at 140 °C for 1 hour from room temperature at the ramping rate of 25°C/hour on the hot plate. The μlens was shaped with the 43 μm of sag and 160 μm of width, characterized by Dektak 150 surface profiler, shown in Figure 6.2. As for the cell reservoir, a negative photoresist, SU8-2050, was spun on the glass substrate to form a rectangular rim of 3 cm × 1.5cm × 15 μm (length×width×height) with the rim thickness of 500 μm.

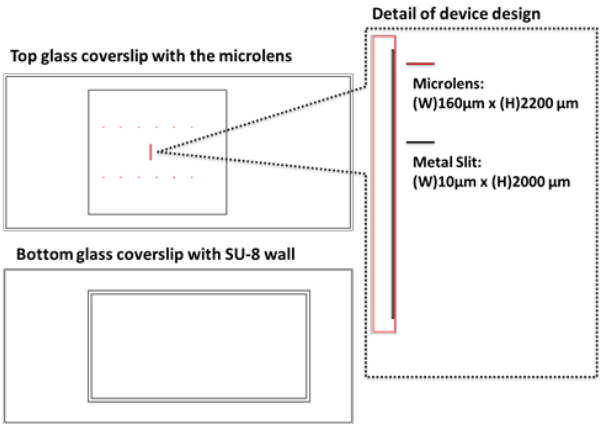

Figure 6.1 Device layout for the scattering-imaging-based cytometer platform.

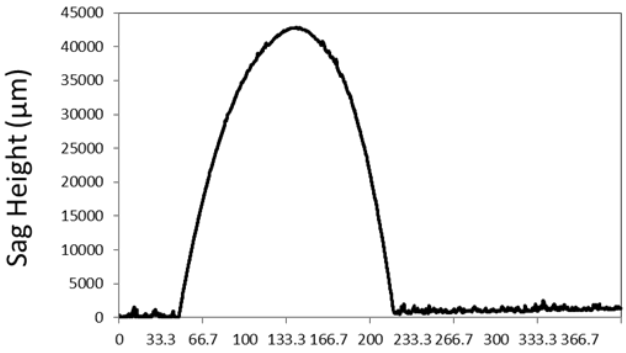

Figure 6.2 Dektek measurement for the morphology of microlens by reflow process.

6. 3. Experimental setup

For the characterization of scattering-imaging-based cytometer with selected cell types, we prepared samples with cancer cells (HEK293 cells) and isolated WBCs (the procedure discussed later). HEK293 (Human Embryonic Kidney) cells were cultured in the growth medium in a humidified incubator at 37°C in 5% CO_2. Whole blood samples used to produce mononuclear and polymorphonuclear WBC samples were purchased from the blood bank (San Diego Blood Bank). All cell samples were suspended in PBS (phosphate buffered saline) solution prior to the experiment. Poly-D-lysine (Sigma P-0899) solution was prepared by dissolving in the sterile water to around 0.2mg/mL, followed by adding poly-lysine solution onto the glass coverslip with the cell reservoir. Incubate the glass coverslip at room temperature for 1 hour at room temperature and then rinse 3 times with PBS. Taking 5μL of cell samples and pipetting on the pretreated glass coverslip, the μlens-covered glass coverslip was used to spread the sample over the glass coverslip at the smearing angle of about 10 degrees. As illustrated in Figure 1(a), the sandwiched glass coverslips with samples were placed on the stage for a stepping pump to slide the bottom glass coverslip at the speed of 4.16μm per second. A halogen lamp with an orange color filter illuminated the glass coverslips. A 20 X lens (N.A. 0.4) was place on the focal plane with respect to the samples to expand the scattering images, which were recorded by CMOS imager (Phantom 7.3) with the frame rate of 10 fps.

6. 4. Sample preparation

In the experiment designed to arrest HEK293 cells at G1 phase, the Mitomycin of 10 μg / ml in Dulbecco's Modified Eagle Medium (DMEM) supplemented with 0.5 % (v/v) fetal bovine serum (FBS) and 1 % (v/v) Penicillin/Streptomycin (PS) was added into the culture medium and then cells were incubated for 3 hours prior to the experiment. On the other hand, 50 ng / ml nocodazole in DMEM supplemented with 0.5 % (v/v) FBS and 1 % PS was used to culture the cells for 16 hours in order to stop the cell cycle at prometaphase. The flow cytometric analysis was executed to confirm the control of cell cycle. Cells at designed stages were washed with PBS. Ice-cold 70% ethanol was added to suspend cells, followed by keeping cells at 4°C for 30 minutes. Centrifuge cell suspension at 2000rpm for 5 minutes and then wash with PBS twice. 2.5 μL RNAse (Invitrogen 12091-021) was added into cell suspension in 500 μL of PBS, incubating at room temperature for 15 minutes. After centrifuge, 25 μL Propidium iodide (PI) was added into cell suspension in 500 μL PBS and then cells were incubated for 5 minutes at room temperature, followed by PBS rinse. Analyze stained cells by Accuri C6 flow cytometer to collect at least 20,000 events per sample, as shown in Figure 6.3.

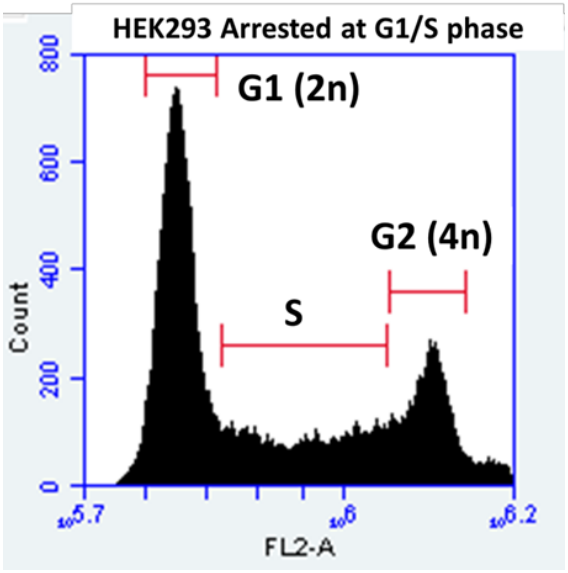

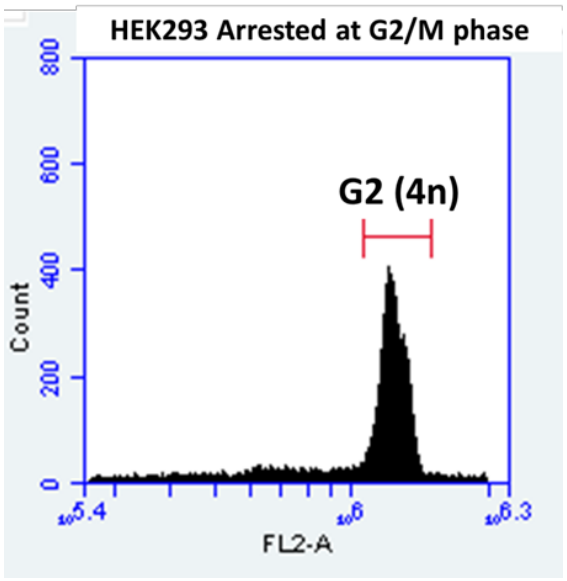

Figure 6.3 Characterized by Accuri C6 and stained with PI, the histogram is comprised of two major peaks located at 2n and 4n levels of cellular DNA contents, which correspond to the cells in the G1/S and G2/M phase, respectively.

The typical Hypaque-Ficoll method with partial modification was used to isolate specific white blood cells from whole blood. 6mL of whole blood purchased from blood bank was mixed with red blood cell lysing buffer (eBioscience, CA) and kept at room temperature for 10 minutes. After centrifuge at 1600 rpm for 5 minutes, cell pellets were rinsed with buffer solution including 10mM ethylenediaminetetraacetic acid (EDTA) and 1X phosphate buffered saline (PBS), followed by another centrifuge. Cells were carefully resuspended in 2.5mL of PBS. Layer the cell suspension over 3mL of Hypaque-Ficoll solution (Sigma 1077) in a 15 mL canonical tube and spin at 1500 rpm for 45 minutes at 4°C using a low brake. Carefully take out the layer of cells (mononuclear cells, MN) between the top level solution and Hypaque-Ficoll solution and the bottom cell pellet (polymorphonuclear cells, PMN), respectively. Resuspend both types of cells in Ca^{2+} and Mg^{2+}-free Hank's balanced salt solution (Sigma) for further experiment.

6. 5. Working principal of scattering-imaging-based cytometer

Figure 6.4. illustrates the schematics of scattering-imaging-based cytometer for detecting scattering images from beads or cells. The scattering-imaging-based cytometer platform includes samples sandwiched with two pieces of glass coverslips. The top glass coverslip (refractive index, n=1.45) is 150 μm in thick, where a 300nm of silver film patterned with 10μm slit is deposited on the glass. The μlens that has 43 μm sag height and 160 μm in wide is fabricated on the surface of silver film with the 5μm of edge-to-

edge alignment between μlens and slit by photolithography process. The bottom glass coverslip has a 15 μm high SU-8 wall as a scaffold for the sample reservoir. The halogen lamp combined with an orange color filter is applied as the light source because the incoherent light with filtered wavelength spectrum minimizes the speckle noise and chromatic aberration. Furthermore, given the 10 μm slit to form a light sheet beam, the spherical aberration can be almost eliminated, resulting in a good quality of label-free scattering imaging. When imaging the scattering light of samples between two glass coverslips, the incoherent light is introduced from the top glass coverslip. The bottom glass coverslip, which is loaded with sample, is slided by a stepping pump with the control speed of 4.16μm/sec. A spatial filter is placed under the glass coverslip to block out the primary transmitted beam, which would saturate the detector, allowing only large angle scattering light to enter 20X lens. All samples on the glass coverslip can be scanned and recorded by the off-the-shelf CMOS imagers (e.g. cellphone CMOS camera) at the frame rate of 10 fps. As the dynamics range of commercial CMOS imagers is narrow, it is the crux that we develop the scattering imaging system by using micro-fabricated μlens to avoid directly saturating the CMOS imager.

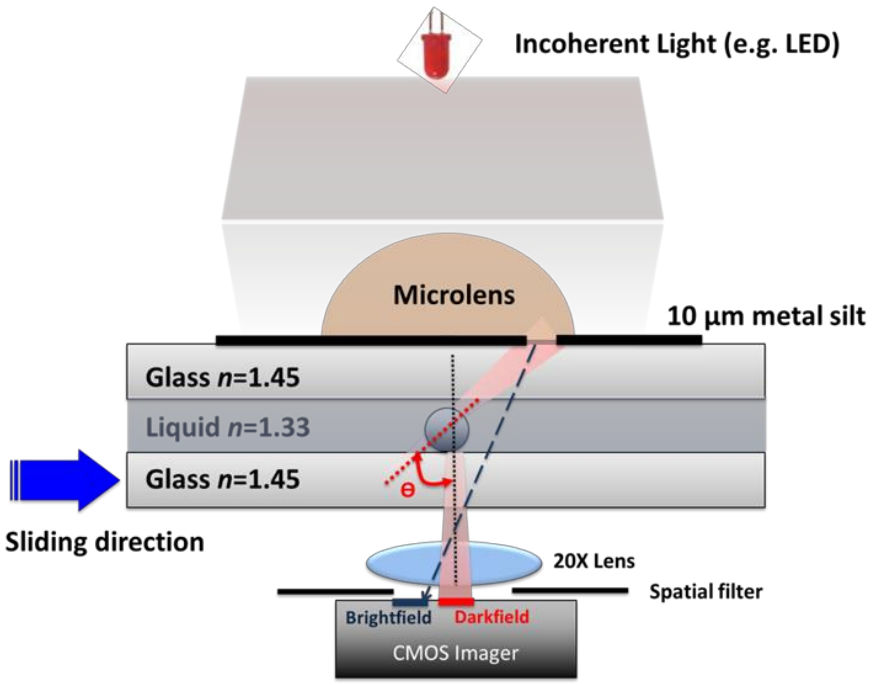

Figure 6.4 Schematics of the scattering-imaging-based cytometer platform, wherein an incoherent light is introduced to penetrate through a 10µm wide slit, forming a light sheet beam that is refracted by a microlens to scan beads or cells. Θ, shown in the schematics, means the scattering angle between the optics axis and transmitted light sheet beam.

Since the fabrication technique of μlens has been extensively studied,[37, 38] the back focal length of μlens can be calculated by the equation, $f_b = n_2 \frac{n_1 R - (n_1 - 1)h}{n_1(n_1 - 1)}$, wherein n_1 =1.63 is the refractive index of μlens, n_2=1.45 is the refractive index of glass coverslip, d and h are the diameter and sag height of μlens, respectively, and R is the curvature of μlens obtained by an approximation, $R = \frac{(d^2 + 4h^2)}{8h}$. Also, the numerical aperture (N.A.) of μlens can be retrieved by $N.A. = n_2 \left\{ \frac{n_2^2}{n_1^2} \frac{4R[Rn_1 - (n_1 - 1)h]}{(n_1 - 1)^2 d^2} + 1 \right\}^{-\frac{1}{2}}$. The f_b and $N.A.$ of μlens are 183 μm and 0.66 in our system, respectively. To further characterize the profile of light-sheet-like beam, the 15μm polystyrene beads are implemented. As shown in Figure 6.5, the dimmer scattering spot is observed on the screen when the leading edge of beads is intercepted by the refracted beam. As bottom glass coverslip slides, the more area of bead is sectioned, the brighter scattering spot is observed, followed by decreasingly dimmer spot when gradually cutting the trailing edge of beads, shown in Figure 6.6. The similar observation is confirmed with 7.66μm polystyrene beads in diameter. The intensity of scattering bright spots of 7.66μm beads is about 4 times weaker than 15μm beads at the same exposure time, which shows the brightness dependency on the bead cross-section scanned. The time-lapse montage of bead scattering images indicates that the width of light sheet beam can be approximately calculated by the intensity profile of bead scattering spots over the entire timespan.

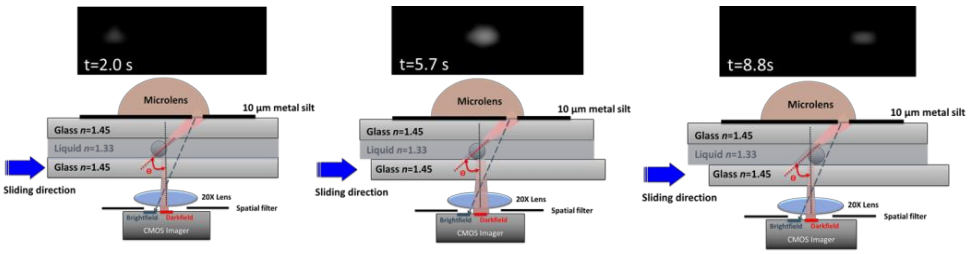

Figure 6.5 Detailed snapshots of 15μm bead traveling the sensing area at different timespan.

Figure 6.6 Time-lapse montage of 15 μm polystyrene bead subjected to sliding altering the scattering images shown on CMOS imager over time.

Figure 6.7 digitalizes the scattering image intensity over frames. Under the experimental condition, each frame means the moving distance of about 0.416 μm. Taken the full width at half maximum and bead diameter into the calculation, the width of light sheet beam is around 3-4 μm, which allows us to resolve the delicate structure within cells. Figure 6.8. shows the snapshot of recording images, showing a bright band exists on the downstream of the sliding direction. It is because the absorption of μlens against the incident light at short wavelength, causing the μlens creates autofluorescence and form the brightfield observation. The intensity of autofluorescent light can be tailored by tuning the exposure time of CMOS imager, and provides self-contained verification images with those images obtained from the darkfield band. In Figure 6.8., polystyrene beads completely block all of light and show the shadows in the bright field; however, the transmitted light can partially penetrate cells and allow us to delineate the cell contour, which will be discussed later. One should note that by recording the scattering light in the dark field, the signal-to-noise ratio of images could be significantly enhanced, resulting in manifest scattering images.

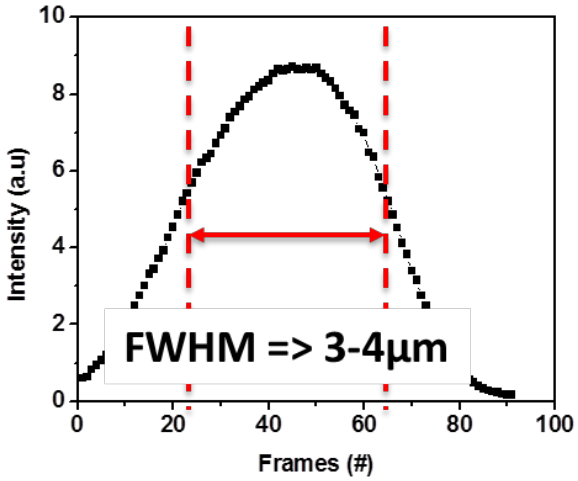

Figure 6.7 The plot of intensity of scattering images versus the frame sequence.

Figure 6.8 A snapshot of 15 μm polystyrene beads interrogated with the scattering-imaging-based cytometer platform, showing clear scattering images in the dark field and a bright band for self-contained verification. Due to the software setting, the brightfield imaging is shown in the downstream direction to align with the sliding direction.

6. 6. Observation of HEK293 cell cycle and construction of nuclear signature

Because the cell nucleus is considered to produce the dominant scattering light within mammalian cells, all the images observed on the CMOS imager reflect the unique properties of the size and shape of the cell nucleus, which can be used as an effective marker for cell classification and cell cycle monitor. To demonstrate the functionality of scattering-imaging-based cytometer as a nucleus monitor tool for biological samples, we first cultured stable HEK293 cell lines. Smearing 5 μL of HEK293 cell suspension in PBS on the poly-D-lysine treated glass coverslip, various morphologies of HEK293 cells are observed in Figure 6.9(a). As glass coverslip slides, the scattering images in the dark field become the translucent objects with discernible boundaries in the bright field. The imaging transition offers a chance to obtain the scattering imaging from cell nucleus and examine the corresponding cell boundary. Interestingly, the cell at division phase, although this type of cell morphologies cannot be observed often due to the relatively short period of mitotic phase during the entire cell cycle, is observed in Figure 6.9(b). This also indicates that whether the cells present as the single, adjacent or dividing form can be distinguished with the combination of dark-to-bright field imaging transition. To more specifically monitor cells at different cycles, we cultured HEK293 cells with cell inhibitors to stop cell at different checkpoints. Mitomycin is used to arrest the cell cycle at G1 phase,[39] where the biosynthetic activities of cells are activated to form necessary proteins for the supply of S phase and thus the size of cells slightly increases. Figure 6.9 (c) shows the images of single HEK 293 cell passing through the dark field and bright field, respectively. Similar

to uncontrolled HEK293 cells, scattering imaging is visibly recorded in the dark field, followed by the translucently brightfield imaging delineating cell boundary. On the other hand, nocodazole is treated to achieve cell cycle arrest at G2/M phase, more specifically at prometaphase. After undergoing G2 phase, cells become even larger, but without microtubule attachment cells cannot proceed the prometaphase, where the nuclear membrane breaks down and then constitutes of nucleus distribute within the cell. At this point, there is no dominant scattering center and thus scattering images could barely be observed in CMOS imager even with three times longer of the exposure time, as shown in Figure 6.9(d). It is further suggested that in cell samples the scattering images can be formed when the complete nucleus exists within the cell. Also, the diameter of cells can be approximately estimated by the brightfield imaging, that is, 21.78±2.47μm and 31.79±3.45μm for cells at G1/S (n=10) and prometaphase (n=10) stage, respectively.

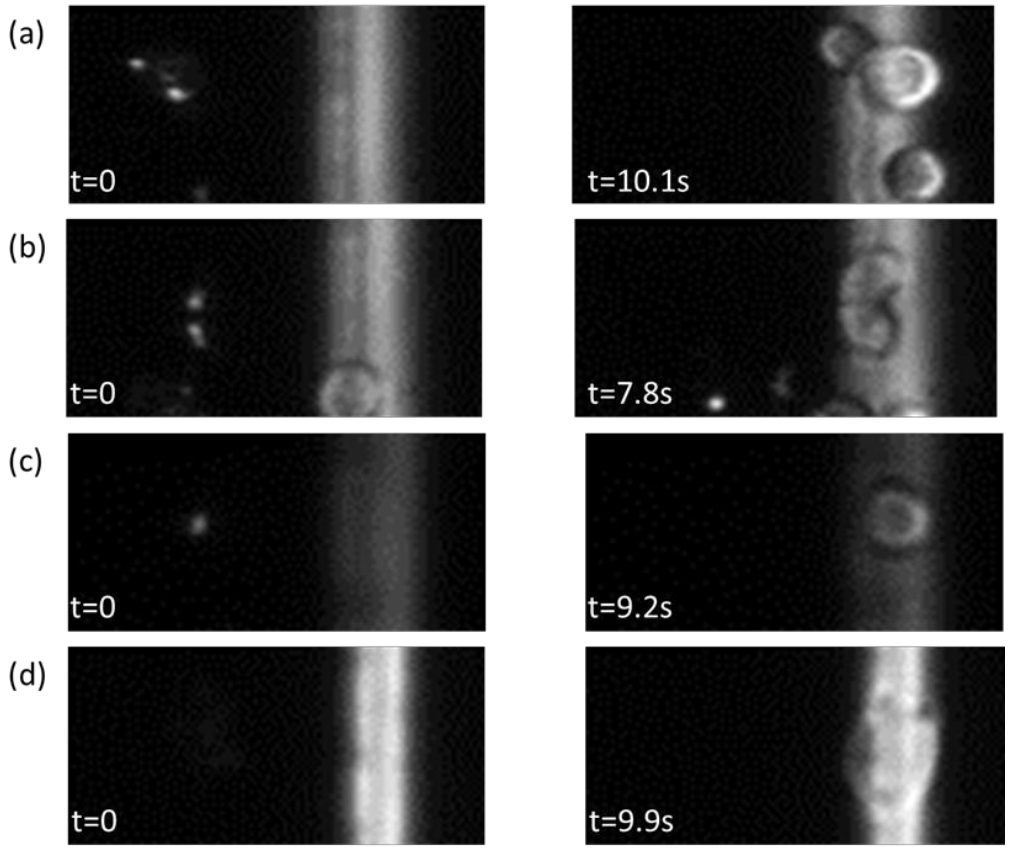

Figure 6.9 (a) and (b) Snapshots of uncontrolled HEK293 cells taken by CMOS imagers, where HEK293 cells are first imaged as darkfield spots, followed by examining under the bright field with definable cell boundary. The brightfield imaging allows further clarification of cell morphology. (c) and (d) Snapshot images of HEK293 cell arrested at G1/S phase and prometaphase stage, respectively. Exposure time is increased 3 times longer in (d).

Based on this finding, taken together with the intensity dependency over frames, we are able to construct the signature of the size and shape of nucleus. Figure 6.10 (a) and (b) show the 3-dimensional contour plot of nuclei of HEK293 cell at G1 and prometaphase stages (i.e. the images of the dark field in Figure 6.9. (c) and 9(d)), respectively. By overlaying each frame over time sequence, the signature of nucleus can be graphed by accumulating the intensity of each pixel. As shown in Figure 6.10 (a), the size of nucleus at G1 phase is averaged to be about 16 μm; however, the size of nucleus at prometaphase cannot be estimated without the definable nuclear shape. We demonstrate that the scattering-imaging-based cytometer can unambiguously record the scattering images from the cell nucleus and create the contour plot as the nuclear signature.

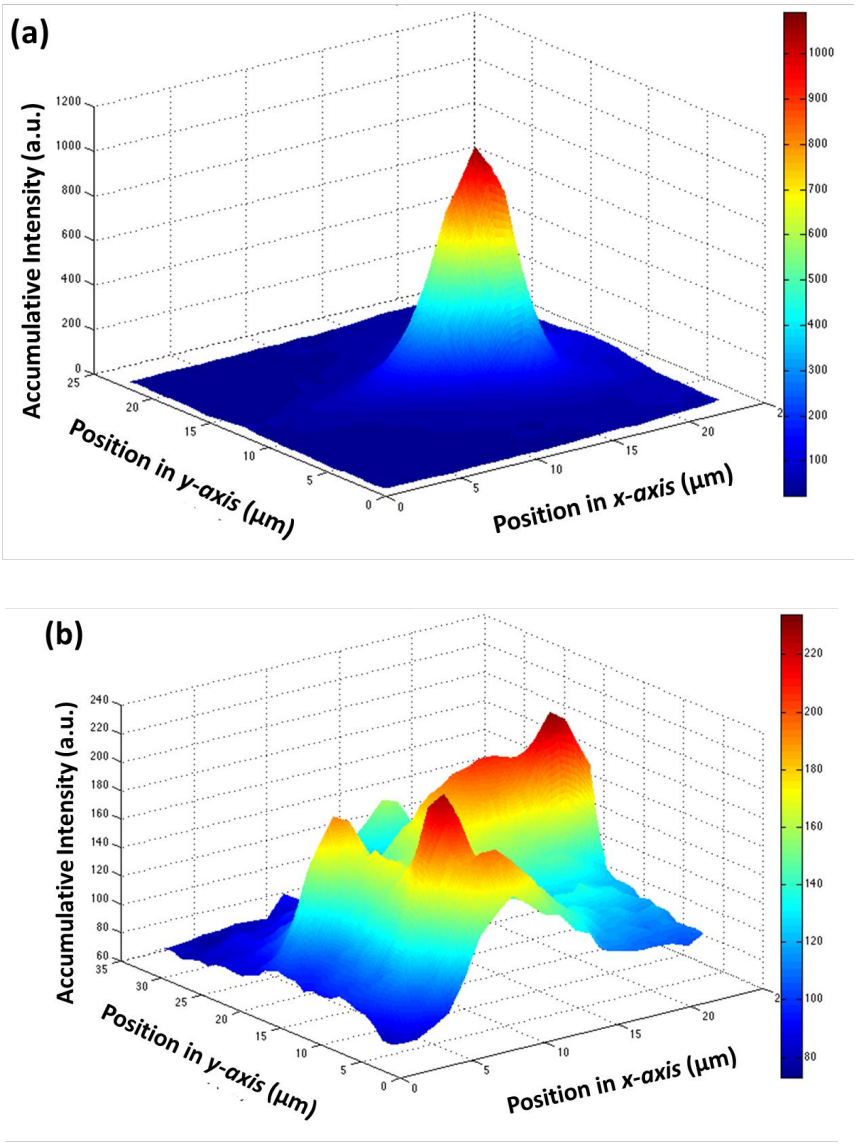

Figure 6.10 (a) and (b) 3-dimensional contour plot of nucleus signature for HEK293 cell arrested at G1/S and prometaphase stages, respectively.

6. 7. Differentiation of white blood cells with nuclear signature

Although most of cell types normally have round or oval nuclear shape, the distinct nuclear shapes in white blood cell family have drawn tremendous attention. It is not only because the white blood cells (WBCs) play important role on the immunological system, but also a wide range of nuclear shapes helps the cell differentiation of WBCs. In general, in terms of nuclear morphologies, WBCs can be categorized to mononuclear (MN) and polymorphonuclear (PMN) cells. MN WBCs are the cell types with single nucleus such as lymphocytes or monocytes. In contrast, PMN WBCs have the presence of 2-5 lobes in their nucleus, e.g. neutrophils. Starting with the whole blood, we isolate PMN WBCs from MN WBCs by using Hypaque-Ficoll method[40]. The analysis results of flow cytometer indicates that high-purified PMN and MN WBCs (each majority > 90%, shown in Figure 6.11) can be obtained prior to applying on the pretreated glass coverslip with poly-D-lysine coating.

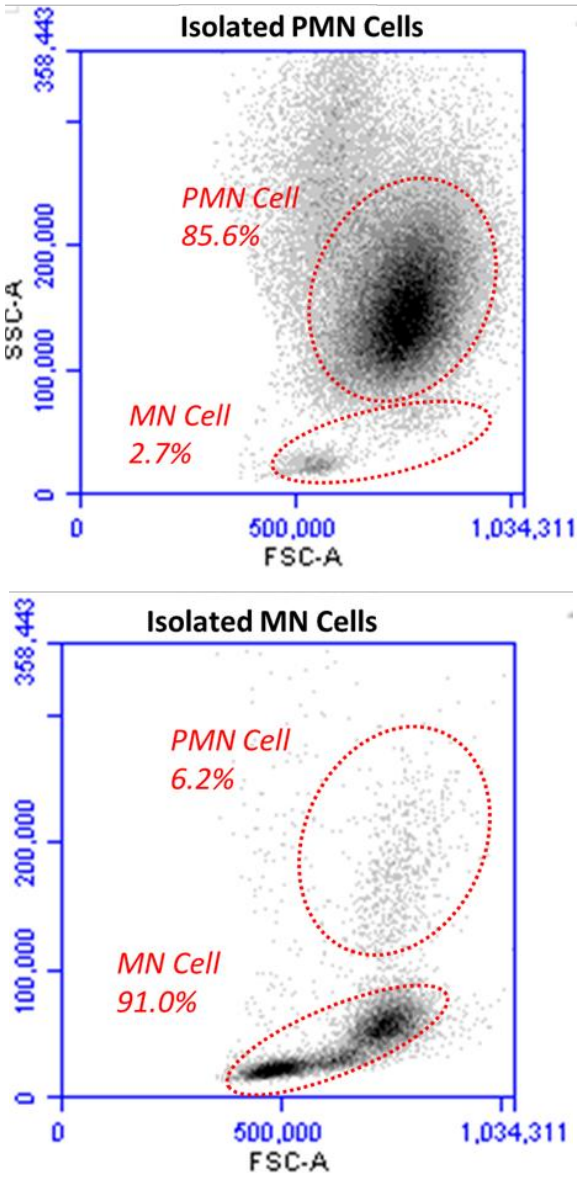

Figure 6.11 Scatter plots of isolated mononuclear (MN) cells and polymophonuclear (PMN) cells from human whole blood, respectively.

Figure 6.12 (a) and (b) show the typical cell traveling snapshots for MN and PMN WBCs, respectively. It is observed that the scattering images of PMN cells are brighter than MN cells in the dark field; meanwhile, the spotty images of PMN cells can be found. It is inferred that the presence of multi-lobed nucleus results in the multi-spotted images. The brightfield imaging shows the diameter of MN (n=10) and PMN (n=10) cells is 10.12±1.01μm and 12.54±1.39μm, respectively. Similarly, we accumulate all images recorded and output the 3-dimensional contour plots as the signature of each cell type. Figure 6.13 (a) and (b) exemplify 2-dimensional and 3-dimensional contour plots of a MN cell, respectively. Similarly, the 2-dimensional and 3-dimensional contour plots of a PMN cell are shown in Figure 6.14(a) and (b), wherein Figure 6.14 (a) shows two main contour populations and one satellite population, indicating multi-lobed structures of neutrophils, and Figure 6.14(b) shows the corresponding contour peaks in 3 dimensional views. Moreover, we also observe four-lobed structure of PMN cell shown in Figure 6.14 (c) and (d). It is indicated that the orientation of nucleus in the cell with respect to the incident light beam can produce the distinct scattering imaging. As shown in Figure 6.15, assuming the nucleus shape is oval, when the long axis of nucleus is oriented to the direction of incident beam the sharp scattering imaging would be shown; on the contrary, if the short axis of nucleus is aligned with the beam direction, the relatively flat shape would be imaged. However, no matter how the orientation of nucleus in cell is the accumulative voxels of the same cell type should keep in a range. Again, as shown in Figure 6.16, the accumulative voxels

within the nucleus contour plot should be similar for the identical cell type. Thus, the accumulative voxels of PMN cells are 3 times more than MN cells.

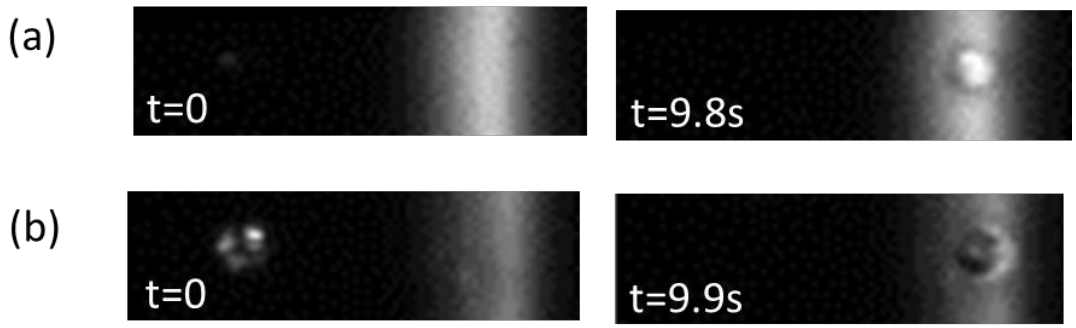

Figure 6.12 (a) Snapshots of mononuclear cells, e.g. lymphocytes, and (b) Snapshots of polymorphonuclear cells, e.g. neutrophils. All cells travel the darkfield imaging first and then go through the brightfield imging for definable cell boundary.

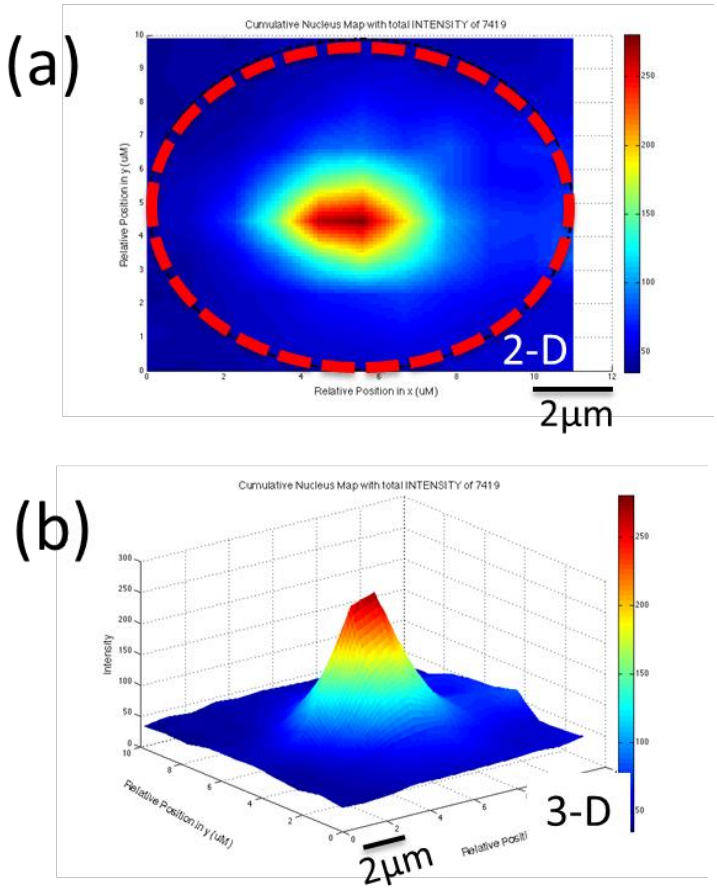

Figure 6.13 (a) and (b) represent 2-dimensional and 3-dimensional contour plot of mononuclear cells, respectively.

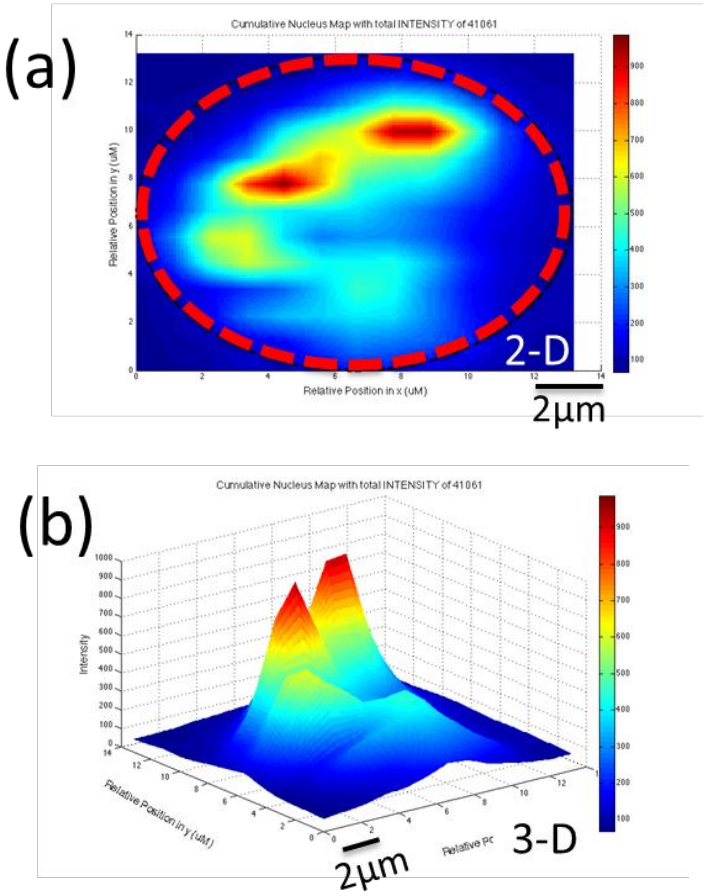

Figure 6.14 (a) and (b) represent 2-dimensional and 3-dimensional contour plot of a polymorphonuclear cell, respectively. (c) and (d) represent 2-dimensional and 3-dimensional contour plot of another polymorphonuclear cell, respectively.

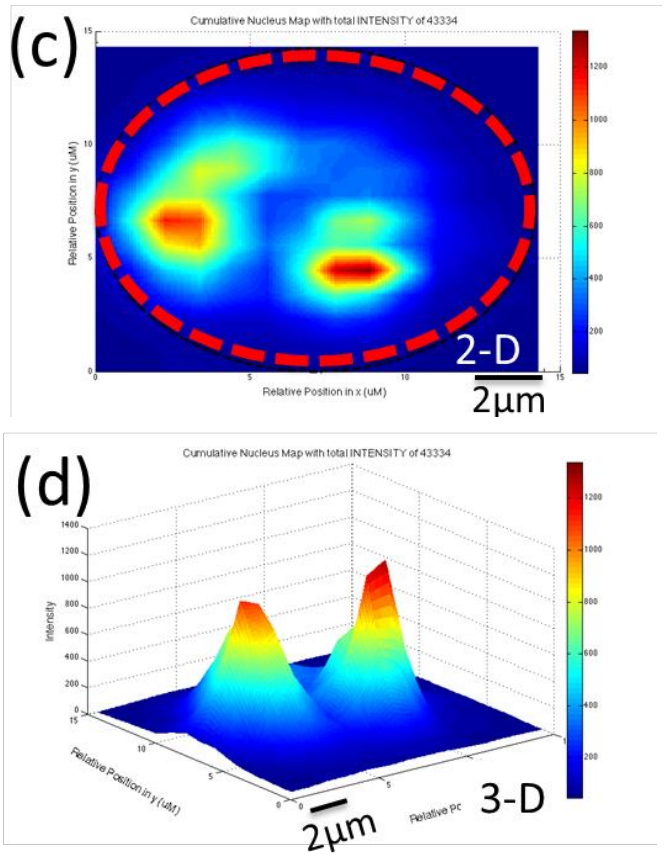

Figure 6.14. Continued

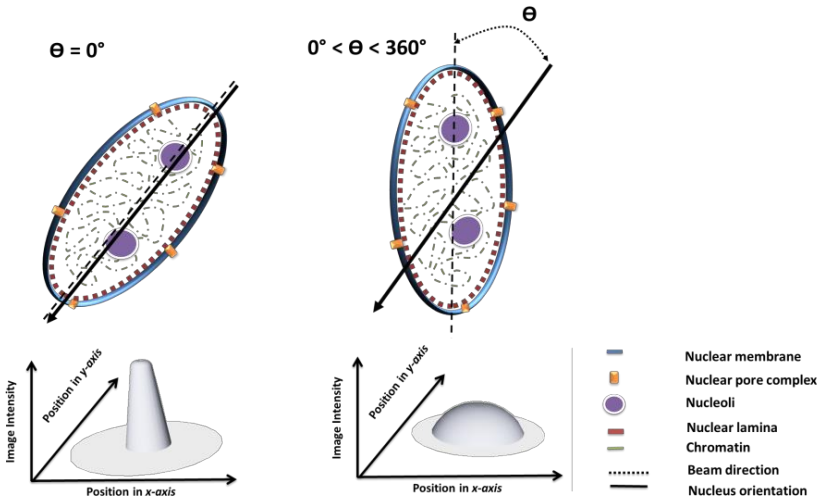

Figure 6.15 Illustration of the orientation effect of nucleus on the scattering imaging.

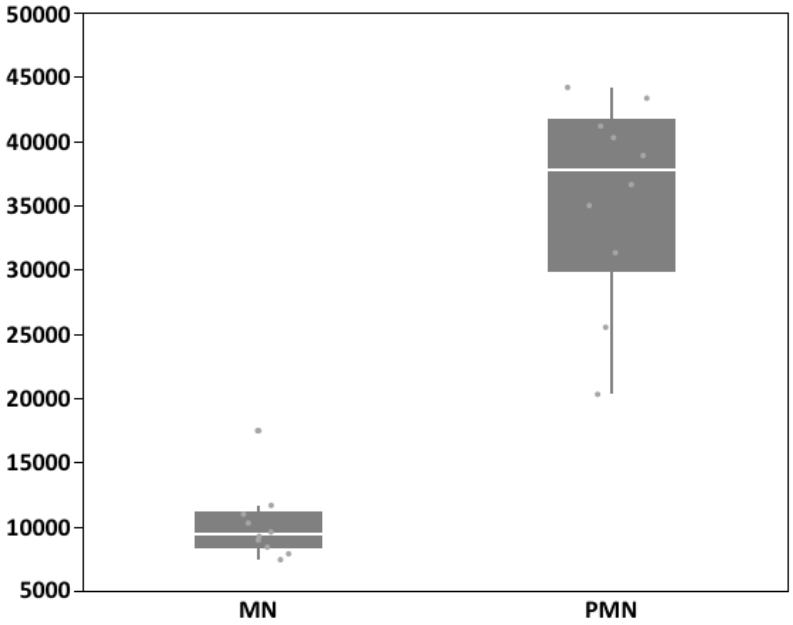

Figure 6.16 Box chart of voxels under 3-dimensional contour plot for mononuclear and polymorphonuclear cells, indicating the accumulative voxels of the same cell type remain within the narrow distribution.

6. 8. Discussion

We have demonstrated a scattering-imaging-based cytometer platform, allowing for label-free imaging the nuclear shape by using a compact optics setup and an inexpensive CMOS imager system. The incoherently incident light was refracted by the micro-fabricated μlens on a thin layer of silver film with 10 μm slit. Due to the narrow opening allowed, the thin light sheet beam is formed to scan the objects. Designed μlens with high N.A. can effectively refracted the light beam to produce scattering light of samples of interest and collect images in the dark field with the CMOS imager. The spatial filter is necessary to block out the primary light to avoid the saturation of the CMOS imager. A 20X lens is merely used to magnify the scattering imaging, showing that the expensive and complicated optics setup is not required for this scattering-imaging-based cytometer platform. More importantly, for most point-of-care applications, the availability of imaging system, e.g. CCD camera, with acceptable sensitivity would become a hurdle. By harnessing omnipresent CMOS imagers on cellphone or any mobile devices, the scattering-imaging-based cytometer platform realizes the in-situ observation of scattering images for beads or cells. It should be noted that the current light sheet microscopy images objects in the bright field, which cannot be accommodated with narrow-dynamic-ranged CMOS imagers. Unlike commercial imaging cytometers, without any cell labeling, we only recorded the scattering light that was generated by any scattering center of samples. All cells are tested with smeared form that simplifies the preparation procedure and exempt from using fluid pump. By doing so, we can ensure that cells or beads will settle down on the same focal plane and

also remove the pressurized flow that may squeeze the nucleus. Given that the lateral field of view of CMOS imager is 460 μm, the scanning area of scattering-imaging-based cytometer platform was about 2.5 mm^2 for 20 minutes of scanning, when the scanning speed of 4.16 μm per second was conducted. The speed of sliding the glass coverslip could be increased as long as the disturbance of fluid is minimized to keep all samples on the same focal plane. This large field of view offers the high throughput for sample analysis. Although the color filter was used, the partial transmission light at short wavelength could be still absorbed by μlens, exciting the autofluorescence to form the bright band from the 10 μm slit. For all objects across this area after passing through the dark field, the bright field images can delineate the outline of beads or cells. Characterizing with 15 μm polystyrene beads that have the definable and strong scattering boundary, the beam width can be experimentally calculated to be about 3-4 μm, which is able to resolve the intracellular morphology.

The functionality of our scattering-imaging-based cytometer can be further implemented on the observation of sub-cellular structures, especially on resolving nuclear morphologies. In order to keep cells focused, the glass coverslip was pretreated with poly-D-lysine for better adhesion between substrate surface and cells. A solid nucleus with the complete nuclear membrane could be considered as a major scattering center within the cells because of its high protein content. It could be proved when HEK293 cells are arrested at prometaphase stage, at which the nuclear membrane disintegrates, the scattering images become significantly dimmer compared to cells at other stages. Also, mutually verifying with darkfield and brightfield imaging, true

nucleus morphologies within cells can be confirmed. We also demonstrated the features that the nuclear size and shape could be deconvoluted as the signature. Because as the glass coverslip slides, the light sheet beam consecutively slices a portion of nucleus that creates the scattering images, the intensity and projected area of scattering image carry the information of orientation, size and shape of nucleus in the cell. We are able to convert the temporal imaging into the spatial structure of nucleus by sequentially accumulating images. Since the light sheet beam scans through the entire nucleus slice by slice at the resolvable temporal scale, the accumulative intensity value of cells can be used as a marker to represent the identical cell type.

Furthermore, it is possible to address cell classification for the clinical applications, for example, multi-part differential white blood cell analysis. One important issue impeding the label-free white blood cell classification in the portable devices is the sensitivity. Without labeling, PMN and MN cells can mainly be distinguished by their size with poor differentiation for most microfluidic devices. In our scattering-imaging-based cytometer, the unique morphology of PMN cells can be reconstructed based on the scattering images when the orientation of nuclear lobes is parallel to the incident angle of light sheet beam. We are able to compare the accumulative intensity between PMN and MN cells. Because of several times difference on the intensities, it is readily to discern the cell types. To our best knowledge, this is the first time that a label-free cell classification by directly distinguishing intracellular structure with microfluidic-based devices has been demonstrated.

3. 6. Conclusion

To summarize, our study provides a new label-free method for rapid identifying the cellular inner structure by imaging the scattering light from the nucleus in the cell. This temporal scattering imaging technique exhibits the significant feature to resolve the shape and size of nucleus. With the aid of imaging processing, the signature of nucleus can be plotted with the 3-dimensional contour. The total voxels can also represent the real volume of nucleus, which offer a new route for the future cell classification. We will undergo the entire solution to in-situ image the nuclear signature, including the design of cartridge that can attach onto smartphone. This technology will likely be further expanded to more clinical applications to interrogate cellular level diseases such as malaria, etc.

References:

1. L. A. Herzenberg, D. Parks, B. Sahaf, O. Perez, M. Roederer and L. A. Herzenberg, Clin Chem 48 (10), 1819-1827 (2002).

2. L. A. Herzenberg, R. G. Sweet and L. A. Herzenberg, Sci Am 234 (3), 108-117 (1976).

3. V. Kachel, G. Benker, K. Lichtnau, G. Valet and E. Glossner, J Histochem Cytochem 27 (1), 335-341 (1979).

4. D. B. Kay, J. L. Cambier and L. L. Wheeless, J Histochem Cytochem 27 (1), 329-334 (1979).

5. D. A. Basiji, W. E. Ortyn, L. Liang, V. Venkatachalam and P. Morrissey, Clin Lab Med 27 (3), 653-+ (2007).

6. R. Kong, S. Friend, B. Hall, D. Basiji and H. Pugsley, J Immunol 190 (2013).

7. S. Friend, R. Kong, B. Hall, D. Basiji and P. Haley, J Immunol 190 (2013).

8. J. G. Wu, G. A. Zheng and L. M. Lee, Lab Chip 12 (19), 3566-3575 (2012).

9. M. Halter, Cytom Part A 81A (8), 643-645 (2012).

10. H. J. Yoo, J. Park and T. H. Yoon, Cytom Part A 83A (4), 356-362 (2013).

11. D. R. Albrecht, G. H. Underhill, J. Resnikoff, A. Mendelson, S. N. Bhatia and J. V. Shah, Integr Biol-Uk 2 (5-6), 278-287 (2010).

12. E. Schonbrun, S. S. Gorthi and D. Schaak, Lab Chip 12 (2), 268-273 (2012).

13. M. J. Kim, K. H. Lim, H. J. Yoo, S. W. Rhee and T. H. Yoon, Lab Chip 10 (4), 415-417 (2010).

14. K. H. Lim, J. Park, S. W. Rhee and T. H. Yoon, Cytom Part A 81A (8), 691-697 (2012).

15. R. Regmi, K. Mohan and P. P. Mondal, Microsc Res Techniq 76 (11), 1101-1107 (2013).

16. J. C. S. Wood, L. L. Wheeless and D. B. Kay, Cytometry 2 (2), 138-138 (1981).

17. J. L. Wu, J. P. Li and R. K. Y. Chan, Opt Express 21 (12), 14474-14480 (2013).

18. I. Navruz, A. F. Coskun, J. Wong, S. Mohammad, D. Tseng, R. Nagi, S. Phillips and A. Ozcan, Lab Chip 13 (20), 4015-4023 (2013).

19. H. Y. Zhu, I. Sencan, J. Wong, S. Dimitrov, D. Tseng, K. Nagashima and A. Ozcan, Lab Chip 13 (7), 1282-1288 (2013).

20. M. Versaevel, M. Riaz, T. Grevesse and S. Gabriele, Soft Matter 9 (29), 6665-6676 (2013).

21. M. Versaevel, T. Grevesse and S. Gabriele, Nat Commun 3 (2012).

22. M. Webster, K. L. Witkin and O. Cohen-Fix, J Cell Sci 122 (10), 1477-1486 (2009).

23. Y. Fu, L. K. Chin, T. Bourouina, A. Q. Liu and A. M. J. VanDongen, Lab Chip 12 (19), 3774-3778 (2012).

24. K. H. Chow, R. E. Factor and K. S. Ullman, Nat Rev Cancer 12 (3), 196-209 (2012).

25. P. Dey, Diagn Cytopathol 38 (5), 382-390 (2010).

26. D. Zink, A. H. Fischer and J. A. Nickerson, Nat Rev Cancer 4 (9), 677-687 (2004).

27. M. Prokocimer, M. Davidovich, M. Nissim-Rafinia, N. Wiesel-Motiuk, D. Z. Bar, R. Barkan, E. Meshorer and Y. Gruenbaum, J Cell Mol Med 13 (6), 1059-1085 (2009).

28. H. Lans and J. H. J. Hoeijmakers, Nature 440 (7080), 32-34 (2006).

29. K. Maeshima, H. Iino, S. Hihara and N. Imamoto, Nucleus-Austin 2 (2), 113-118 (2011).

30. L. J. Edens, K. H. White, P. Jevtic, X. Y. Li and D. L. Levy, Trends Cell Biol 23 (4), 151-159 (2013).

31. A. D. Walters, A. Bommakanti and O. Cohen-Fix, J Cell Biochem 113 (9), 2813-2821 (2012).

32. R. Barer and S. Joseph, Q J Microsc Sci 95 (4), 399-423 (1954).

33. R. Barer and K. A. F. Ross, J Physiol-London 118 (2), P38-P39 (1952).

34. M. Hesse, A. Raulf, G. A. Pilz, C. Haberlandt, A. M. Klein, R. Jabs, H. Zaehres, C. J. Fugemann, K. Zimmermann, J. Trebicka, A. Welz, A. Pfeifer, W. Roll, M. I. Kotlikoff, C. Steinhauser, M. Gotz, H. R. Scholer and B. K. Fleischmann, Nat Commun 3 (2012).

35. M. Kawasaki, K. Sasaki, T. Satoh, A. Kurose, T. Kamada, T. Furuya, T. Murakami and T. Todoroki, Cell Proliferat 30 (3-4), 139-147 (1997).

36. J. Y. Wang, P. P. Lou, R. Lesniewski and J. Henkin, Anti-Cancer Drug 14 (1), 13-19 (2003).

37. J. Lim, P. Gruner, M. Konrad and J. C. Baret, Lab Chip 13 (8), 1472-1475 (2013).

38. J. Chen, W. S. Wang, J. Fang and K. Varahramyan, J Micromech Microeng 14 (5), 675-680 (2004).

39. S. G. Kang, H. Chung, Y. D. Yoo, J. G. Lee, Y. I. Choi and Y. S. Yu, Curr Eye Res 22 (3), 174-181 (2001).

40. W. Nauseef, in Neutrophil Methods and Protocols, edited by M. Quinn, F. DeLeo and G. Bokoch (Humana Press, 2007), Vol. 412, pp. 15-20.

Chapter 6 or portion thereof will be submitted by Tsung-Feng Wu, Tony Minghung Yen, Yu-Jui Chiu, Yuanyuan Han, Yu Sheng Lin and Yu-Hwa Lo (2014).

Chapter 7

Conclusion

The development of optofluidic lab-on-a-chip (LOC) flow cytometer for point-of-care (PoC) applications has drawn tremendous attetion. The LoC devices are intended to be portable, easy-to-use, and low cost for in-vitro diagnosis. However, due to the issues of device fabrication, precision optics and optomechanics, performance and

functionality, optofluidic LoC devices demonstrated to date have not been able to match their bench top counterpart. Issues on device manufacturing will be removed by continuous improvements in technology, but other issues related to performance, particularly sensitivity and functionality, demand novel solutions outside the fields of conventional flow cytometry. Also to minimize the complexity of sample preparation, the label-free method offers a route to address the clinical uses. To this end, we have employed innovative device architectures and computational methods to enhance the signal-to-noise ratio for optofluidic devices. The space-time coding technique, aided by digital signal processing, not only increases the signal quality significantly but also reveals valuable cellular information (e.g. cell size, stiffness, intracellular structure) via direct measurements of cell position and velocity out of the space-time coded signal. Such additional information produces room for the data-mining algorithm to further improve the accuracy for cell classification.

Although we have demonstrated a label-free optical-coding technique for rapid cell classification, the more detailed information of cell is still lacking. We further proposed a new label-free imaging method for directly onserving the cellular inner structure by imaging the scattering light from the nucleus in the cell. This temporal scattering imaging technique exhibits the significant feature to resolve the shape and size of nucleus. With the aid of imaging processing, the signature of nucleus can be plotted with the 3-dimensional contour. The total voxels of 3-dimensional contour can also represent the volume of nucleus, which offer a new route for the future cell classification. We will undergo the entire solution to in-situ image the nuclear signature,

including the design of cartridge that can attach onto smartphone. This technology will likely be further expanded to more clinical applications to interrogate cellular level diseases such as malaria, direct whole blood exam, etc.

.